Exploring Collective Radiative Dynamics with Nanofiber-Coupled Atomic Ensembles in a Fiber-Ring Resonator

From Cavity to Waveguide QED

DISSERTATION

zur Erlangung des akademischen Grades
DOCTOR RERUM NATURALIUM
(Dr. rer. nat.)
im Fach Physik

eingereicht an der
Mathematisch-Naturwissenschaftlichen Fakultät
der Humboldt-Universität zu Berlin

von

M.Sc. Daniel Lechner

Präsidentin der Humboldt-Universität zu Berlin
Prof. Dr. Julia von Blumenthal

Dekanin der Mathematisch-Naturwissenschaftlichen Fakultät
Prof. Dr. Caren Tischendorf

Gutacher
Prof. Dr. Arno Rauschenbeutel
Prof. Dr. Robin Kaiser
Prof. Dr. Janik Wolters

Tag der mündlichen Prüfung
24.09.2024

There is a theory which states that if ever anyone discovers exactly what the Universe is for and why it is here, it will instantly disappear and be replaced by something even more bizarre and inexplicable.

There is another theory which states that this has already happened.

Douglas Adams

ABSTRACT

Efficient coupling between photons and quantum emitters is crucial for research and applications that employ light–matter interaction. This coupling is typically realized in one of two paradigmatic settings: cavity quantum electrodynamics (QED) or waveguide QED. In cavity QED, light–matter coupling is enhanced through the repeated interactions with circulating photons in a cavity. In contrast, waveguide QED achieves strong light–matter interactions by tightly confining light within structures such as nanophotonic waveguides, enabling strong interactions with thousands of emitters in a single pass. These two regimes are typically considered to be distinct as most experimental setups operate in either one or the other regime.

In this thesis, we demonstrate a unique experimental system capable of seamlessly transitioning between cavity and waveguide QED. The key element is an ensemble of neutral cesium atoms coupled to a nanofiber-based optical interface that is integrated into a fiber-ring resonator. Using this system, we study light–matter interaction in cavity QED, waveguide QED, as well as in the transition regime between the two. In particular, starting from waveguide QED, we study the collective radiative dynamics of large ensembles of atoms coupled to the nanofiber. We perform detailed measurements of superradiant decay, demonstrating how the system transitions from an initial superradiant state, where emission is enhanced, through subradiant states, where emission is inhibited.

In another set of experiments, we investigate the transition between waveguide and cavity QED by changing the length of the fiber-ring resonator. For a cavity length of 45 m, the roundtrip time is much longer than the response time of the atoms. Therefore, the temporal dynamics are characterized by repeating features that are reminiscent of the single-pass dynamics observed in waveguide QED. Shortening the resonator length to 6 m, where the cavity roundtrip time is comparable to the response time of the atoms, the single-pass features start to overlap, leading to the appearance of Rabi oscillations. For even shorter cavity lengths, the features associated with a single pass vanish and Rabi oscillations dominate the dynamics.

Our findings in this largely unexplored regime of cavity QED highlight the interplay between the collective single-pass dynamics of an ensemble, typical of waveguide QED, and the resulting ensemble–cavity dynamics of cavity QED. This novel platform has the potential of enabling new protocols in emerging quantum technologies.

ZUSAMMENFASSUNG

Eine effiziente Kopplung zwischen Photonen und Quantenemittern ist entscheidend für die Forschung und für Anwendungen, die auf der Wechselwirkung zwischen Licht und Materie basieren. Diese Kopplung wird in der Regel in einem von zwei paradigmatischen Regimen erreicht: Resonator Quantenelektrodynamik (QED) oder Wellenleiter QED. In der Resonator QED wird die Licht–Materie Kopplung durch die wiederholte Wechselwirkung der umlaufenden Photonen im Resonator verstärkt. Im Gegensatz dazu erreicht die Wellenleiter QED starke Licht–Materie Wechselwirkungen, indem Licht in Strukturen wie nanophotonischen Wellenleitern stark fokussiert geführt wird. Dies ermöglicht starke Wechselwirkungen mit Tausenden von Emittern in einem einzigen Durchgang des Lichtes. Diese beiden Regime werden in der Regel als getrennt betrachtet, da die meisten Versuchsaufbauten entweder in dem einen oder in dem anderen Regime liegen.

In dieser Arbeit demonstrieren wir ein spezielles experimentelles System, das einen nahtlosen Übergang zwischen Resonator und Wellenleiter QED ermöglicht. Das Schlüsselelement ist ein Ensemble neutraler Cäsiumatome, das an eine nanofaserbasierte optische Schnittstelle gekoppelt ist, die in einen Faserringresonator integriert ist. Mit diesem System untersuchen wir Licht–Materie Wechselwirkung in Resonator QED, Wellenleiter QED sowie im Übergangsbereich zwischen beiden. Insbesondere untersuchen wir, ausgehend von der Wellenleiter QED, die kollektive Strahlungsdynamik großer Ensembles von Atomen, die an die Nanofaser gekoppelt sind. Wir führen detaillierte Messungen des superradianten Zerfalls durch und zeigen, wie das System von seinem anfänglichen superradianten Zustand, in dem die Emission verstärkt ist, in subradiante Zustände übergeht, in denen die Emission gehemmt ist.

In einer weiteren Reihe von Experimenten untersuchen wir den Übergang zwischen Wellenleiter und Resonator QED, indem wir die Länge des Faserringresonators verändern. Bei einer Resonatorlänge von 45 m ist die Umlaufzeit viel länger als die Reaktionszeit der Atome. Daher ist die zeitliche Dynamik durch sich wiederholende Merkmale gekennzeichnet, die an die in der Wellenleiter QED beobachtete Einzeldurchangsdynamik erinnern. Wenn der Resonator auf eine Länge von 6 m verkürzt wird, wird die Umlaufzeit des Resonators vergleichbar mit der Reaktionszeit der Atome. Dabei beginnen sich die wiederholenden Einzeldurchangsdynamiken zu überlappen, was dann zu Rabi Oszillationen führt. Bei noch kürzeren Resonatorlängen verschwinden

die mit der Einzeldurchangsdynamik verbundenen Merkmale und Rabi Oszillationen dominieren die Dynamik.

Unsere Ergebnisse in diesem weitgehend unerforschten Regime der Resonator QED verdeutlichen das Zusammenspiel zwischen der kollektiven Einzeldurchgangsdynamik, wie sie für Wellenleiter QED typisch ist, und der daraus resultierenden Ensemble–Resonator Dynamik der Resonator QED. Diese neuartige Plattform hat das Potenzial, neue Protokolle in aufkommenden Quantentechnologien zu ermöglichen.

ACKNOWLEDGMENTS

Four years ago I embarked on the journey of doing a PhD, and now I finally can write these words as I am finishing my thesis. Despite the ups and downs, I truly enjoyed my time in the lab and beyond, and I am very happy to have pursued this journey within Arno's group.

Therefore, I want to start by thanking you, Arno, for giving me the opportunity to pursue this journey in your group. Thank you for giving me this space to grow. I want to thank you for all the valuable discussions and your ability to explain complex topics intuitively. Your sharp mind has navigated us through many unknown territories in the field of light–matter interaction and have been crucial in shaping this research.

Furthermore, I want to thank you, Jürgen, for always having an open ear and taking the time to explain anything in just the right words. Your passion for physics is inspiring, and it is always a pleasure to discuss with you (for hours) and share your knowledge. Let there be cake... and Spätzle, but not too many vegetables!

And of course, I also want to thank you, Riccardo! You have been a constant support throughout this journey. I have learned so much from you, starting from my first time coupling light into a fiber, to aligning double-pass AOMs, to analyzing our data and understanding whatever was happening in the lab. Your knowledge and critical thinking were always there to answer any questions that I might have and were vital to my growth as a physicist.

I also want to thank Martin (Austrian pronunciation) at this point, who built our NanoFiRe experiment from scratch and taught me all of its quirks. Thanks for always lifting the heaviest things in the lab, being unconventional and for showing me your favorite noisy music. Thank you, Philipp, for valuable input, helpful discussions and your continuous support. You always brought new perspectives into our focus, which have added depth to our work.

I am also deeply grateful to the rest of GOP. I spent a fantastic time in our group and the atmosphere that you create makes a huge difference. I want to highlight Sofia, thank you so much for being who you are. Your curiosity and your enthusiasm is so refreshing, and I value your support so much! Whenever I had a bad time, I could come to you and you would have exactly the right words. All the best for you, Max and ... ? Chris, thank you for being a brilliant physicist and a great friend. You have been inspiring me so much and made

me feel normal during tough times. I look forward to many more years of friendship, enjoying your saxophone play and taking part in "Evening rants with Luisa Esguerra". Speaking of which... Luisa, or better known as LaserLuisa, an unofficial member of our group. Your combination of amazing physicist, dancer, relationship coach and all-around awesome human being make you very dear to my heart. LaserLuisa and DiffractionDani just belong together. We have to do another Friday Light Show! This is also a good point to thank the BOS.QT graduate program, as otherwise I would not have gotten to know you! Merci à Martin (French pronunciation, or Marteng), for sharing my passion for outreach and adding your French coolness to the group. It was so much fun to inspire kids during the science fairs in Brussels together with Sofia, and also in Berlin with the rest of the group. Thank you Constanze for being a fantastic physicist, for bringing fabulous vibes into the group and for fighting the good fight. Thanks for all the sugar in the form of Sicilian sweets, Gabriele, I wish you the best for your new chapter in life as a father. Also thanks to Luke, part of the thesis-writing weekend shift, and for influencing my decision to join this group. Playing the bagpipes when I interviewed was unforgettable. Big thanks also to Inna, you brought fresh air into the group and are the best Mensa mate. I will always be there to trouble shoot your life. Thanks to Felix for being a great office mate, to Lucas for sharing the best train knowledge, to Luca for the brief, but sweet time we spent in the lab, to Xin Xin for sharing a fascination of cats, and to Jihao for the best restaurant tips. I am very grateful also to Thomas for keeping the group running smoothly, for pulling our fibers, and your great sense of humor. A big, big thank you to Fedoua for always supporting and helping us navigate the administration of Humboldt University, your patience is outstanding and we will be very sad to see you go.

A heartfelt thanks to everyone who helped proofread my thesis – Riccardo, Jürgen, Deepl, ChatGPT, Ahmad, Angi, Anita, Bea, Celia, Fabi, Lea. Special thanks also to Mark Edwards and the Humboldt Graduate school for the course on Planning the Completion of your Dissertation. Without the things that I learned in this course about planning, I would not have finished the thesis in five months, just in time before summer!

Beyond the scientific community, I am thankful to everyone who made my time in Berlin so special and keeping me sane during my PhD. A very special shoutout (or singout?) goes to *oh my choir*. You are the most amazing, colorful, sparkling community that I am so grateful to have in my life and to sing with! I love you all so much! Meeting you, Danilo, has been the best 30th birthday present I could ever have imagined. One month ago, we had our first musical production, which

I co-organized with the Luftschloss team – Julius, Lino, Anita, Celia, Franka. Was it way too stressful so close to handing in? Yes! Was it worth it? Absolutely! Special shoutouts also to the oh my libourne crew – Angi, Aron, Celia, Charlotte, Franka, Lea, to my BassBabes – Flow, Julius, Lachie, Lino, Nicolò, Max, Sebastian, and also Bea, Yoni, Rike, Eliad, Matteo, Liss, Tanguy, Moritz, Jana, Tom, Simone, Kelly, Lena, Lena, Lea, Inga, Johanna, Valerie, Len, Sarah...

I am so happy to have so many great friends who enrich my life: Kevin (thanks for typesetting the cover), Lena, Lukas, die Kompakten Brudis – Yoki, Oussama, Ahmad, Tomás + me – Emilio, Meret, Julian, Jonas, Nimar, Judith, Magda, Klaudia, Alexandra, José, Fabi...

Auriane, I am deeply thankful for the connection we have. Thank you for always being there for me, for your love, your encouragement and the wonderful times we share. Thanks for making me appreciate how to properly cut French cheese, for great dinner dates and the best brunches. Je t'aime beaucoup!

I also want to thank my parents, Heidi and Mario, mi familia, for all your unwavering love and support. Thank you for bringing me up in a way that made me cherish the present moment, to love good food and to always be kind. I am immensely grateful to have you in my life and I could not have asked for better parents.

Whenever I forget the beauty of physics, I put on my diffraction glasses and marvel at the spectrum of the world around me. This kind of everyday physics keeps me captivated by the wonders of science, and seeing the light in other people's eyes that see these wonder for the first time brings me immense joy.

Thank you all for being part of this incredible journey through light and matter!

Daniel LichtLechner

LIST OF PUBLICATIONS

The following publications have been published during the course of working on this thesis.

- Daniel Lechner, Riccardo Pennetta, Martin Blaha, Philipp Schneeweiss, Arno Rauschenbeutel, and Jürgen Volz.
  Light-Matter Interaction at the Transition between Cavity and Waveguide QED.
  Physical Review Letters, 131(10):103603, 2023.

- Riccardo Pennetta, Daniel Lechner, Martin Blaha, Arno Rauschenbeutel, Philipp Schneeweiss, and Jürgen Volz.
  Observation of Coherent Coupling between Super- and Subradiant States of an Ensemble of Cold Atoms Collectively Coupled to a Single Propagating Optical Mode.
  Physical Review Letters, 128(20):203601, 2022.

- Riccardo Pennetta, Martin Blaha, Aisling Johnson, Daniel Lechner, Philipp Schneeweiss, Jürgen Volz, and Arno Rauschenbeutel.
  Collective Radiative Dynamics of an Ensemble of Cold Atoms Coupled to an Optical Waveguide.
  Physical Review Letters, 128(7):073601, 2022.

- Daniel Lechner, Andreas Zepp, Marc Eichhorn, and Szymon Gładysz.
  Adaptable Shack-Hartmann Wavefront Sensor with Diffractive Lenslet Arrays to Mitigate the Effects of Scintillation.
  Optics Express, 28(24):36188-36205, 2020.

CONTENTS

1 INTRODUCTION

Fundamental research on light–matter interactions and many applications of quantum optics rely on efficient interfaces to couple photons and emitters. There are two paradigmatic approaches to this goal: cavity quantum electrodynamics (QED) and waveguide QED. Cavity QED achieves efficient coupling by embedding emitters within a cavity, where photons circulate through the cavity and interact multiple times with the emitters, thus enhancing the interaction strength. Conversely, in waveguide QED, light is typically strongly confined in the transverse direction to increase the interaction strength. This is achieved, for example, by using nanophotonic waveguides, where it is possible to couple many thousands of emitters to light in a single pass along the length of the waveguide.

Cavity QED has a long history and has enabled a deeper understanding of many fundamental properties of quantum physics [1–3]. The origins of cavity QED can be traced back to a remark by Purcell [4], who found that the spontaneous emission rate of an emitter changes depending on its environment, indicating that spontaneous emission is not solely an intrinsic property of the emitter. In free space, an emitter can radiate into an infinite number of vacuum modes. However, when the environment is altered, the number of modes available for the emitted light field also changes. Drexhage was the first to systematically study this effect by placing quantum emitters near metallic mirrors, thus finding that their emission rates would change significantly depending on the distance to the mirror [5, 6]. Therefore, by engineering the environment, the radiation properties of emitters can be controlled. An effective way of engineering this environment is to place emitters into a cavity, for example, into a Fabry-Pérot cavity consisting of two parallel mirrors. Such a cavity has a discrete frequency spectrum of longitudinal modes that depends on the spacing between the mirrors. Coupling emitters to such cavities led to experiments in which enhanced emission into the cavity mode was demonstrated [7–9], but also to experiments in which the opposite phenomenon was observed, where the emission of emitters could be inhibited if the cavity lacks a mode that matches the emission wavelength [8, 10–12]. Under normal circumstances and without a cavity, light and atoms do not interact very strongly. By placing atoms between the mirrors of a cavity, the interaction strength is significantly enhanced, as photons

are confined within the cavity, allowing them to interact multiple times with the atoms. This interaction strength is usually quantified by the so-called cooperativity parameter $C = g^2/\kappa\Gamma_o$, which is defined as the ratio between the atom–cavity coupling rate, g, the cavity loss rate, κ, and the spontaneous decay rate of the atoms, Γ_o.

The theoretical foundations of cavity QED were established by Jaynes and Cummings in 1963. They introduced a simple, fully quantized model of a single atom interacting with a single frequency mode of a cavity [13]. In the strong coupling regime, which is reached when the atom–cavity coupling rate exceeds both the spontaneous emission rate and the cavity loss rate, the radiative dynamics differ significantly from those of a free-space atom. The model predicts that spontaneous emission becomes a reversible process. A photon emitted into the cavity can return to the atom through coherent energy exchange with the cavity field. This causes the atom to oscillate between its ground and excited state at the Rabi frequency, a phenomenon known as vacuum Rabi oscillations. In the frequency domain, this results in new eigenstates of the coupled system, separated by the Rabi frequency, known as vacuum Rabi splitting.

The strong coupling regime was reached experimentally in the 1980s, driven by the pioneering work of Serge Haroche and his collaborators, who investigated the behavior of Rydberg atoms interacting with photons in low-loss superconducting microwave cavities. In the following years, researchers were able to observe Rabi oscillations [14–18] as well as the vacuum Rabi splitting [19–22] experimentally, demonstrating the quantized nature of the light field and achieving coherent control of quantum systems. For his pioneering work in this field, Serge Haroche was honored with the Nobel prize in physics in 2012 [23] along with David J. Wineland, who researched trapped ions [24].

Research on cavity QED has thus been instrumental for the fundamental understanding of light–matter interaction, but it also offers applications in many emerging quantum technologies [25–32].

In cavity QED, research focuses mostly on scenarios where emitters interact with a single longitudinal frequency mode of the cavity. In contrast, in waveguide QED, propagating photons interact with waveguide-coupled emitters during a single pass of light. In this regime, emitters interact with an infinite number of longitudinal modes that are guided in the waveguide, coupling them to a continuum of frequency modes.

Waveguide QED has been successfully implemented with various platforms such as quantum dots [33, 34], defect centers in solid state materials [35], or atoms [36] coupled to photonic crystal waveguides, superconducting qubits coupled to superconducting transmission lines

[37], and neutral atoms coupled to hollow-core fibers [38–40], or to optical nanofibers [41].

In this thesis, we study an experimental platform that is at the transition between cavity and waveguide QED. Depending on the experimental setting, it can exhibit the characteristic features of one or the other regime. The system is based on a nanofiber coupled to cold neutral cesium atoms. This situation is very close to an ideal configuration, in which a single propagating optical mode interacts with an ensemble of identical two-level systems distributed in one dimension. A nanofiber is an optical fiber that has been tapered to a sub-wavelength diameter in a heat-and-pull process. The guided mode along a nanofiber features a pronounced evanescent field, which allows for coupling of thousands of emitters to the guided mode. In this configuration, the atom–photon coupling is collectively enhanced, and the observed dynamics is very different compared to the case of single isolated atoms. This way, collective effects, such as superradiance or subradiance arise. In these phenomena, the spontaneous emission rate is modified by the presence of other atoms [36, 40, 42–44].

In the experiments described in this thesis, the nanofiber-based optical interface is integrated into a fiber-ring resonator. The strong collective coupling of atoms to the resonator allows us to study cavity QED in a system where we can systematically investigate the transition between waveguide and cavity QED by allowing for cavities with arbitrary lengths, where emitters interact with more than one cavity mode. Despite its conceptual significance, this transition regime has only been explored in a limited number of studies [45–49].

The majority of cavity QED systems reported in literature use short resonators, such as Fabry-Pérot cavities [50, 51] or whispering-gallery-mode resonators [52–54], with cavity lengths typically limited to the range of centimeters. Due to the length-independent cooperativity in our system, we can make our resonator unusually long, with cavity lengths presented in this work in the range of 5 m to 45 m. The case of waveguide QED can be conceptualized in this context as cavity QED with an infinitely long cavity. In the regimes that we discuss, the emitter linewidth is on the order or larger than the free spectral range of the cavity, allowing the emitters to interact with multiple cavity modes at the same time.

This way, we can experimentally explore the transition from cavity to waveguide QED and study the connection between the collective response of the atomic ensemble during a single pass of light and the corresponding ensemble–cavity dynamics.

This thesis is organized as follows: in Chapter 2 we describe our experimental platform, provide a comprehensive overview of the experimental setup, and present the theoretical modeling of the system

using a cascaded interaction model for a single pass of light, and an extension of the model when the system includes a resonator.

Chapter 3 focuses on the collective dynamics of a nanofiber-coupled ensemble excited by pulses of light. We observe collective Rabi oscillations after the pulse is turned on and superradiant decay after the pulse is turned off. These phenomena are explored by investigating the atom-by-atom dynamics and by comparing our observations with the predictions of our theoretical model. Additionally, we examine how the pulse interacts multiple times with the same ensemble via our very long cavity, which allows us to reach very high optical depths.

In Chapter 4 we study the decay dynamics following the switch-off of the excitation light field in more detail, both experimentally and theoretically. We demonstrate that after a short period of superradiant decay, ensembles prepared in the timed Dicke state pass through their subradiant states, where emission into the waveguide is inhibited.

Chapter 5 explores the transition between cavity and waveguide QED. By adjusting the length of our resonator, we adjust the number of longitudinal modes that interact with the atoms. Our findings demonstrate that Rabi oscillations vanish as the cavity length increases, and the system's response becomes dominated by repeating dynamics characteristic of waveguide QED.

In Chapter 6, we discuss the implementation of a nanofiber-based optical dipole trap in our experimental setup, and study the influence of mechanical oscillations of the nanofiber on the lifetime of atoms in these traps.

Finally, Chapter 7 concludes the thesis and outlines future perspectives for our experiment.

2 NANOFIBER-BASED ATOM–LIGHT INTERFACE

Our research focuses on a nanofiber-based atom–light interface, which provides a highly controlled and close to ideal system for observing light–matter interactions. What sets our experimental setup apart from other nanofiber-based systems is that we integrate the nanofiber within a very long fiber-ring resonator. Using a tunable fiber-coupler, we conduct experiments in both waveguide and cavity QED.

In the initial part of this thesis, we do not trap atoms around the nanofiber, as is common in other nanofiber experiments in our group. Instead, we interface cold atoms from a magneto-optical trap (MOT) directly with the evanescent field surrounding the nanofiber. In the final chapter of this thesis, we will discuss the implementation of trapping with the goal of achieving trapped atoms within a fiber-ring resonator.

The setup was primarily built by the previous PhD student on our experiment, who has extensively documented the experimental setup and its theoretical modeling in his thesis [55]. In this chapter, we provide a summary of the key components of the experimental setup, its current configuration, and the theoretical frameworks used to model our experimental data.

2.1 EXPERIMENTAL SETUP

A sketch of the setup of our nanofiber-based atom–light interface is shown in Figure 2.1. We generate a cloud of cold cesium atoms using a magneto-optical trap (MOT) inside a vacuum chamber. The cloud is overlapped with our nanofiber, which enables us to interface and probe the atoms with fiber-guided light via the evanescent field around the nanofiber. This transmitted or reflected light is then detected with single photon counting modules (SPCM). The nanofiber is integrated into a fiber-ring resonator that contains a tunable fiber coupler. With this coupler, we can modify the coupling rate to the resonator, allowing us to operate the cavity in different regimes according to the requirements of the measurement. Most experiments are performed close to critical coupling, but the resonator can also be completely overcoupled. In this case, light makes a single roundtrip,

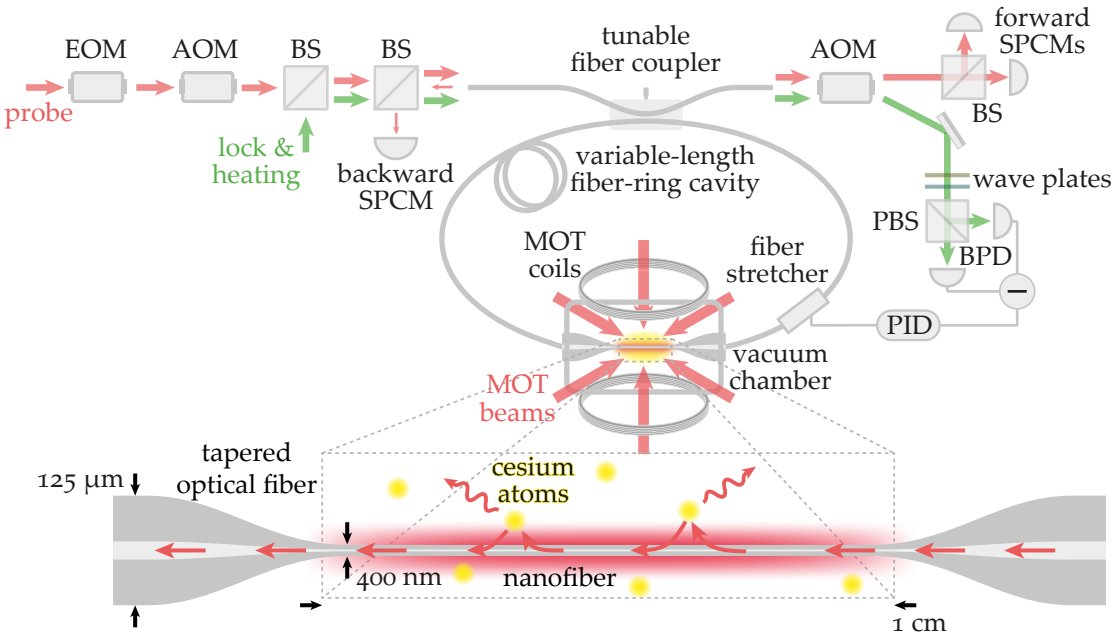

Figure 2.1: Schematic illustration of the most important parts of our experimental setup, which are explained in this section. EOM: electro-optic modulator, AOM: acousto-optic modulator, BS: beam splitter, SPCM: single-photon counting module, PBS: polarizing beam splitter, BPD: balanced photodiode, MOT: magneto-optical trap.

which is equivalent to having no cavity and allows experiments in waveguide QED.

The description of the setup that we present in the following is valid for the experiments Chapters 3, 4 and 5. In Chapter 6, we modified the setup to achieve trapping of atoms and the details of that setup are discussed in Section 6.2.

2.1.1 Nanofiber

The main tool in our experiments that we use to interface light with atoms is the optical nanofiber. Nanofibers guide a large part of light in the evanescent field, allowing us to couple guided light to atoms in the vicinity of the nanofiber along its entire length.

Nanofibers are produced by tapering standard optical fiber to a diameter smaller than the wavelength of light that is guided. Our group uses a flame-brushing technique, where a hydrogen–oxygen flame heats optical fiber above its glass transition temperature [55, 56]. By simultaneously pulling the fiber from both ends and moving the fiber along the flame with translation stages, we can produce precise taper profiles [57]. The nanofiber is then located at the waist of the tapered optical fiber, as sketched at the bottom of Figure 2.1. In our experiment, a 125-µm diameter fiber is tapered down to a

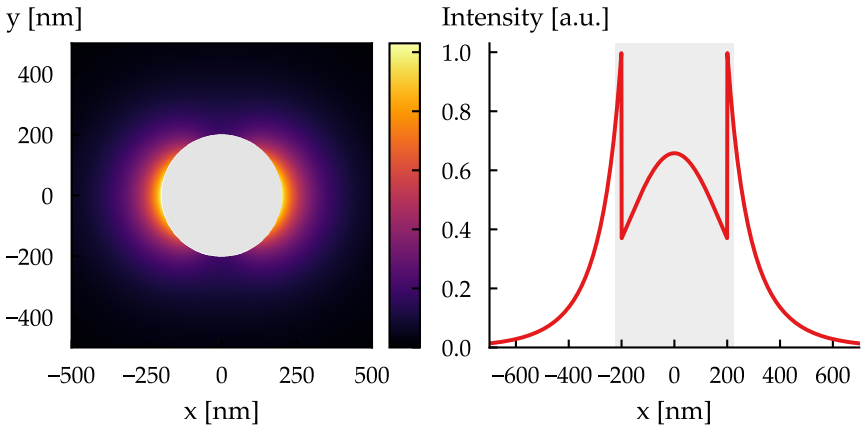

(a) Intensity distribution **(b)** Intensity cross section

Figure 2.2: Calculated intensity distribution of the guided mode in a nanofiber with a diameter of 400 nm for light with a wavelength of 852 nm that is quasi-linearly polarized along the x-direction. The values are normalized to the maximum intensity at the surface of the nanofiber. **(a)** shows the intensity distribution in the x–y plane and **(b)** depicts a cross-section of the intensity along $y = 0$.

nanofiber waist diameter of 400 nm with a length of 1 cm. It is possible to manufacture nanofibers with adiabatic tapers with transmissions close to 100%. In our pulling rig, we regularly achieve transmission values of about 99%. However, the transmission often degrades upon insertion into the vacuum chamber, a problem we encountered and discuss in Section 6.2.1. Additional details on the fabrication process of our nanofibers can be found in [55, 56, 58].

As the diameter of an optical fiber is reduced to below the wavelength of guided light, the light is not guided anymore by the refractive index difference between core and cladding, but rather at the glass–air interface. Along the taper transition, light is adiabatically transformed from the fundamental mode in the single-mode fiber to the fundamental mode in the nanofiber. Figure 2.2(a) shows the normalized intensity distribution of the guided mode in the x–y plane around our nanofiber and Figure 2.2(b) gives a cross-section of the distribution along $y = 0$. The light field that was launched in this simulation has a wavelength 852 nm and is linearly polarized in the x-direction. The simulation shows that almost 50% of the optical power is guided in the evanescent field around the nanofiber.

The key point of using nanofibers is then that the evanescent field decays exponentially with distance from the fiber on a length scale of $\approx \lambda/2\pi = 135$ nm. As a result, atoms only efficiently interact with the guided light when they are in close proximity to the fiber surface. Since the nanofiber also supports only a single optical mode, the interaction

Figure 2.3: Fluorescence image of the cloud of cold cesium atoms generated by our MOT. This cloud has an optical depth of about 30 when probed with fiber-guided light. The scattering of the cooler light also makes the nanofiber visible in the image.

predominately occurs along a narrow, almost one-dimensional region of the three-dimensional MOT cloud, which can be significantly longer than for a focused free-space laser beam, which diverges. As a result, the atoms are arranged along the nanofiber in a thin layer surrounding the fiber due to their selective excitation by the evanescent field.

2.1.2 Magneto Optical Trap

In order to be able to conduct experiments, in which light interacts with atoms, it is essential that the atoms remain sufficiently long in the evanescent field around the nanofiber. We achieve this by cooling cesium atoms to low temperatures using laser cooling in a magneto-optical trap (MOT). In expansion measurements in our setup, we measured temperatures of around 80 µK [55], corresponding to a velocity of 127 nm/µs, which is consistent with similar experiments and provides an interaction time on the order of 1 µs [59]. Figure 2.3 shows a fluorescence image of our MOT when it is overlapped with the nanofiber. When probed through the fiber, this cloud results in an optical depth of about OD = 30. The optical depth is a measure of the transmission through an atomic ensemble on resonance as $T = e^{-\mathrm{OD}}$ and the measurement is explained in Section 2.1.6.

A MOT combines laser light and magnetic fields to cool and trap neutral atoms. The basic setup contains three mutually orthogonal, counter-propagating pairs of laser beams and a pair of coils that creates a quadrupole magnetic field. The specific setup of the vacuum chamber, the laser setup and the magnetic coils for the MOT in our experiment is detailed in [55].

The principle of laser cooling is often referred to as Doppler cooling. Atoms that move towards a cooler laser field that is red-detuned from their resonance, are more likely to absorb photons as they perceive the light closer to resonance due to the Doppler effect. As atoms absorb the momentum of photons that propagate opposite to their movement

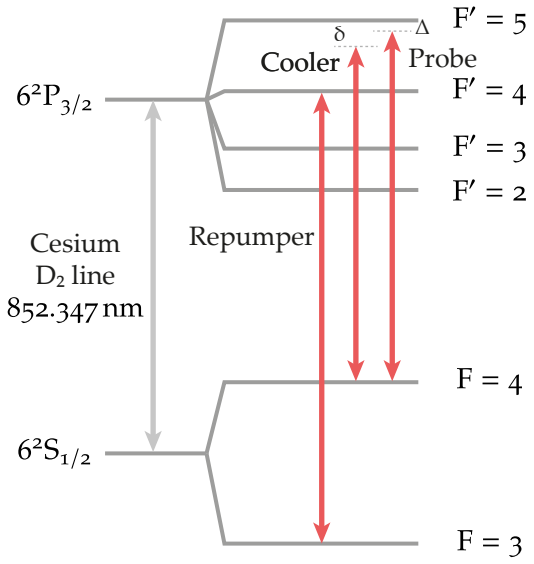

Figure 2.4: Level scheme of the cesium D_2 transition, illustrating the transitions the cooler, repumper, and probe lasers are locked to. Δ represents the detuning of the probe from atomic resonance, and δ indicates the detuning of the cooler.

direction, but re-radiate photons isotropically, they are, on average, slowed down. When there are three counter-propagating pairs of laser fields, atoms are slowed in all directions. Light thus exerts a friction or damping force on the atoms, similar to that experienced by particles in a viscous fluid such as honey or molasses, hence the name of this arrangement *optical molasses*. Although an optical molasses reduces the kinetic energy of atoms and therefore cools them, it does not confine atoms and they can still diffuse out of the illuminated region.

To achieve trapping in addition to cooling, a MOT incorporates a quadrupole magnetic field. The amplitude of the field strength increases linearly and changes sign at a zero-crossing of the magnetic field. This creates a spatially varying Zeeman shift of the energy levels. Additionally, the MOT laser beams are circularly polarized, which causes selective driving of σ^+ or σ^- transitions between the Zeeman-shifted levels. As a result, atoms moving outward are more likely to absorb photons from the MOT beams that become resonant with the Zeeman-shifted levels. The momentum imparted by these photons pushes the atoms back toward the zero-field region, trapping them there.

The cooler laser field excites cesium atoms on the so-called cycling transition from the $F = 4$ ground hyperfine state to the $F' = 5$ excited hyperfine state of the D_2-transition, as depicted in the level scheme in Figure 2.4. Here, F denotes the total angular momentum quantum

number. The cooler laser field is red-detuned by $\delta = 2.1\Gamma_o = 2\pi \times 11\,\mathrm{MHz}$. However, as atoms spontaneously decay back to their ground state, there is a non-zero probability that they end up in the $F = 3$ ground state, which is not resonant with the cooler laser field, thus removing them from the cooling cycle. In order to prevent atoms from accumulating in this state, an additional repumper laser field is used, which copropagates with the cooler laser fields. This repumper is tuned to the transition from $F = 3$ to $F' = 4$ and as atoms decay back from this state to $F = 4$ they can re-enter the cooling cycle, ensuring efficient cooling performance.

2.1.3 Nanofiber-Guided Light Fields

In our setup, we launch up to three light fields into the nanofiber: a blue-detuned heating laser, a lock laser and a probe laser (see Figure 2.1). These laser fields are prepared on a dedicated laser table in our laboratory, where their frequency and powers are controlled using acousto-optic modulators (AOMs). Once all laser fields are prepared, they are coupled into fibers that route the light to the experiment table, where they are combined into the resonator containing the nanofiber.

The heating laser has a wavelength of 780 nm and is used to heat the nanofiber, which prevents cesium atoms and other impurities from accumulating on the fiber surface. In the absence of the heating laser, the nanofiber transmission decreases on a timescale of seconds due to these deposits. Activating the heating laser reverses this effect to a certain extent. However, high heating laser powers also destabilize the resonator spectrum, as power fluctuations cause temperature-induced length fluctuations of the resonator, that cannot be compensated by our stabilization system (see also Section 2.1.5). Therefore, we limit the heating laser power to below 300 µW to keep the resonator spectrum stable. Additionally, we have also observed that when the linewidth of the heating laser field is too small, the resonator spectrum is also destabilized because frequency fluctuations of the laser fields are translated to power fluctuations of the intracavity field and therefore the cavity length. Therefore, we deliberately misalign the grating of the self-built external cavity diode laser to keep the diode running freely, which enhances system stability.

The lock and the probe laser fields both originate from the same commercial Toptica DL Pro laser system at wavelength 852 nm that is locked to a cesium vapor cell using Doppler-free saturation spectroscopy. The lock laser field is used for the active stabilization of the resonator, as detailed in Section 2.1.5. During locking of the resonator, this laser field is continuously kept on, but it is switched off shortly

before probing the system, as its power (~µW) is significantly higher than that of the probe laser field (~pW).

The probe laser field is resonant to the D_2 line of cesium on the $F = 4$ to $F' = 5$ transition, as illustrated in the level scheme of cesium in Figure 2.4. When scanning the frequency of the probe laser field with an AOM, its power changes due to frequency dependent diffraction efficiencies of the AOM. To compensate for these changes, the power of the probe light is stabilized using a photodiode on the experiment table and a PID controller that adjusts the amplitude of the signal that feeds the AOM.

In our experiments, it is necessary to be able to rapidly switch the probe field on and off and to generate boxcar-shaped pulses with rise and fall times smaller than the lifetime of the atoms. To achieve this, we use an electro-optic modulator (EOM) based on a Mach-Zehnder interferometer design (iXBlue NIR-MX800), which allows us to modulate the amplitude of light. The continuous-wave probe laser field is fed into the modulator via a fiber, where light is split into two paths. The relative phase between these two paths is modulated using an electro-optic material, specifically lithium niobate. By varying the applied voltage, this modulation results in either destructive or constructive interference at the output of the interferometer, allowing for precise and rapid modulation of the amplitude of the output light. However, the performance of the device is sensitive to the bias voltage which defines the operating point of the interferometer. Thermal drifts and accumulation of charges in the device cause the bias voltage to shift over time, resulting in imperfect interference. Therefore, before each measurement run, we calibrate the bias voltage by scanning it and measuring the transmission of light through the device to determine the bias voltage with the highest extinction. The electrical pulse that is used to rapidly modulate the input voltage is supplied by a fast pulse generator (Active Technologies PG-1000). For a pulse length of 150 ns, the generator produces electrical pulses with a measured single-shot 20-80% rise and fall time of 75 ps. When measured with a fast photodiode, we indeed observe a rise time on the order of 75 ps. However, in the actual experiment, we use very low optical powers which requires us to detect photons with SPCMs and therefore averaging over many pulses. Under these circumstances, the average detected pulse has a rise and fall time of ≈ 1 ns, due to timing jitter caused by the SPCMs and time tagging of the counts.

Even though the EOM allows us to switch light very fast, its extinction ratio is limited to about 20 dB. While this is sufficient for most of our measurements, we utilize an AOM alongside the EOM for scenarios that require the detection of very small signals after the EOM is switched off (see Figure 2.1). The AOM has a response time of

only $\approx 50\,\mathrm{ns}$, but it suppresses light such that the SPCM background counts become the limiting factor.

2.1.4 Detection Setup

As shown in Figure 2.1, we detect light both in transmission through the nanofiber as well as in reflection using SPCMs from Excelitas (SPCM-AQRH-14-FC). To remove background photons stemming from the heating laser and the environment, we use bandpass filters around our probe wavelength of 852 nm and narrow-linewidth volume Bragg gratings (not shown in Figure 2.1). While this allows us to remove most undesired photons, we cannot remove photons that are generated by Raman scattering of the blue-detuned heating laser field within the glass fiber, which extends into our probe wavelength range. In forward direction, we split light using a 50:50 beamsplitter and then use two SPCMs to detect it. This Hanbury Brown and Twiss configuration allows us to perform correlation measurements of the detected light, although we have not studied the correlations of the emitted photons in this thesis. Furthermore, having two detectors reduces the impact of the dead time of the SPCMs of about 25 ns and increases the maximum count rate. In backward direction, a single SPCM is sufficient as the rate of photons that are reflected off the ensemble is about two orders of magnitude lower than that of the transmitted photons. We record the clicks from the SPCMs using a Swabian Instruments Time Tagger 20 and a custom-built software that fetches the data from the Time Tagger and writes the data to file. Due to the low light power levels, we need to average the recorded counts over many experimental runs to obtain our data.

2.1.5 Fiber-Ring Resonator

The fiber-ring resonator in our setup is formed by connecting the two ends of the optical fiber containing the nanofiber section to a tunable four-port fiber coupler (Newport F-CPL-830-N-FA) as sketched in Figure 2.1. The coupler's variable coupling ratio allows precise control over the coupling rate, κ_{ext}, into and out of the cavity.

Due to the variable coupling rate, we can operate our experimental system in different regimes by adjusting the external coupling rate, κ_{ext}, relative to the intrinsic loss rate of the cavity, κ_0. Depending on their ratio, the system can operate in the undercoupled ($\kappa_{\mathrm{ext}} \ll \kappa_0$), critically coupled ($\kappa_{\mathrm{ext}} = \kappa_0$) or overcoupled ($\kappa_{\mathrm{ext}} \gg \kappa_0$) regimes. This flexibility allows us to transition from a waveguide QED system, where the resonator is overcoupled and light makes a single pass

through the ensemble, to a cavity QED system, where light makes multiple roundtrips through the cavity.

Our all-fiber resonator allows for easy modification of the cavity length by splicing different lengths of optical fiber between one port of the fiber coupler and the fiber containing the nanofiber section. In this thesis, the cavity length varies between about 5 m and 45 m.

Fiber resonators and, in general, all types of fiber interferometers are very sensitive to fluctuations. Fluctuations in the temperature of the fiber due to room temperature variations or laser power fluctuations, causes the associated optical path length to fluctuate. An optical path length change on the order of one wavelength shifts the resonator spectrum by one free spectral range. As we always average many experimental runs, fluctuations cause a broadening of the observed resonances, making narrow resonances challenging to resolve. To increase the stability of the resonator, the optical fiber is coiled around a massive aluminum block and housed in an acoustically and thermally insulated box. However, passive measures alone proved insufficient to prevent drifts, so active stabilization was additionally required. We actively stabilize the resonator by locking it to the probe laser field and thus the atomic resonance frequency using the Hänsch-Couillaud polarization spectroscopy locking technique [60–62]. Our system incorporates a piezo fiber stretcher as part of the resonator and uses the error signal derived from polarization spectroscopy to dynamically counteract optical path length changes. The lock laser field excites the polarization eigenmodes of the fiber-ring. Using a pair of polarizing beam splitters and photodiodes, we can analyze the change in polarization state of the lock laser field at the output of the birefringent resonator. Since this change depends on the resonator length, we can generate an error signal with steep slopes at the position of the cavity resonances that can be fed to a PID controller that in turn adjusts the fiber stretcher and counteracts changes in resonator length [55]. Due to the significant intensity of the lock light relative to the probe light, and because the lock light is resonant with the atoms, we temporarily disable the stabilization during the 0.5 ms probing time and allow the resonator to drift freely. As most of the drifts are temperature dependent and thus relatively slow, the system bandwidth, which is limited to about 300 Hz by the response of the piezo amplifier, is high enough to resolve the cavity resonances when averaging many experimental runs. When locking the 45-m-long resonator, we thus manage to stabilize the optical path length of the resonator to about ±10 nm, or 1% of the free spectral range.

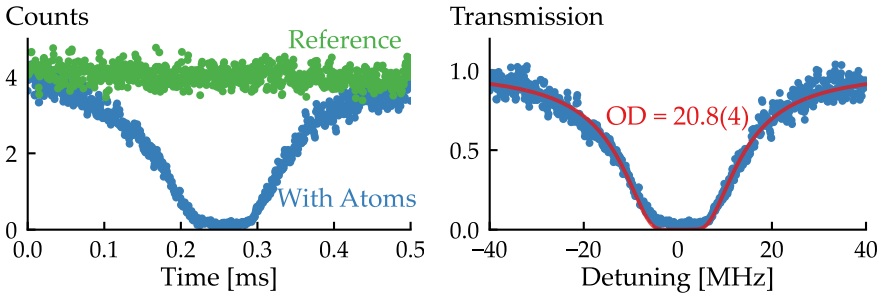

(a) SPCM counts

(b) Normalized and fitted transmission

Figure 2.5: A typical measurement of the optical depth of an ensemble. **(a)** shows the raw SPCM counts averaged over 50 experimental runs with atoms and a reference without atoms, and **(b)** shows the normalized and fitted transmission spectrum.

2.1.6 Experimental Control and OD Measurement

Our experiment is fully controlled via an ADwin Pro II system, which provides real-time synchronized control of multiple analog and digital outputs. The analog outputs deliver stable voltages to control devices in the laboratory such as the amplitude and frequency modulation inputs of the AOM drivers or the magnetic field currents. The digital outputs are used to trigger and synchronize the pulse generator, the Time Tagger for data acquisition, or control servo shutters. We use a custom-built interface in our group that allows easy programming of ADwin. This interface enables direct control of all outputs and the execution of complex sequences using a Python interface.

The most common measurement we perform in the laboratory is the determination of the optical depth of the atomic ensemble. The optical depth is defined by the on-resonance power transmission of light through a medium as $T = e^{-\mathrm{OD}}$. For large optical depths, this transmission becomes too small to measure as the photon count rate falls below the background count rate of our detectors. Therefore, we infer the optical depth by recording the transmission spectrum of the ensemble and fitting the data with a saturated Lorentzian, as described in the following.

To conduct this measurement, we first set the tunable fiber coupler to overcouple the resonator, such that light makes a single pass through the ensemble. Figures 2.5(a) and 2.5(b) show the collected and fitted data from this measurement. The measurement sequence begins by loading cesium atoms into a MOT for about 3 s. After a MOT is loaded, the cooler and repumper laser fields are turned off, letting the MOT cloud expand. We then probe the cloud of cold atoms by scanning the frequency of the probe laser field across the atomic transition in 0.5 ms,

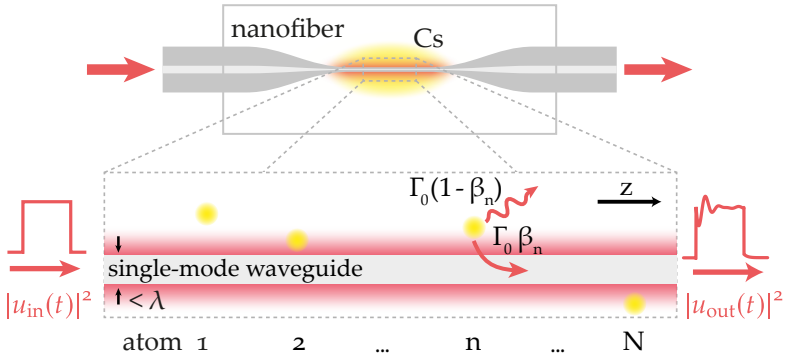

Figure 2.6: The situation considered in the cascaded interaction model assuming unidirectional propagation and emission of light into the waveguide. Cesium atoms from a MOT (depicted in yellow) interact sequentially with the guided mode of a single-mode waveguide, which is a sub-wavelength diameter nanofiber in our experimental system. Atoms scatter light with a rate of $\Gamma_o\beta_n$ into the forward-propagating mode of the waveguide and with $\Gamma_o(1-\beta_n)$ into free space. An incoming light pulse $|u_{\text{in}}(t)|^2$ interacts with the atoms to yield a modified outgoing pulse $|u_{\text{out}}(t)|^2$.

while the transmitted power is continuously measured with an SPCM. The magnetic fields of the MOT coils remain on during probing as they require about 10 ms to switch off. This measurement is repeated multiple times, with the counts averaged over many experimental runs. To obtain a reference, we repeat the same sequence without loading a MOT. This allows us to normalize the counts to a transmission, which we fit with a saturated Lorentzian of the form $T = \exp\left(\frac{-\text{OD}(\Gamma_o/2)^2}{\Delta^2+(\Gamma_o/2)^2}\right)$, where $\Delta = \omega - \omega_a$ is the detuning of the probe laser frequency, ω, from the atomic resonance frequency, ω_a, and Γ_o is the natural linewidth of the atomic transition. From this fit, we extract the optical depth of the ensemble.

2.2 THEORETICAL FRAMEWORK

This section outlines the theoretical framework we use to model the light-matter interaction in our system. We introduce the cascaded interaction model, which is the basis for our theoretical descriptions of the transmission of light through ensembles of nanofiber-coupled atoms. We then discuss the interaction of light and emitters in resonators and extend the description of the cascaded interaction model.

2.2.1 Cascaded Interaction Model

The core of the cascaded interaction model is that the probe field propagates along the waveguide and interacts sequentially with the atoms in a cascaded manner, hence the model's name. The model is very versatile and can be applied to a wide range of experimental situations where light interacts with emitters in a cascaded manner. It allows us to model all experimental scenarios in this thesis. This includes both the waveguide QED case, where light makes a single pass through the ensemble, and the more complex cavity QED case, where light interacts many times with atoms that are embedded within a resonator of arbitrary length. The basic principles of the cascaded interaction model are based on the formalism presented in References [48, 55, 63, 64], with our description closely following the work of Blaha et al. [48], who adapted the model to our experimental system.

The situation that we seek to describe is the propagation of a weak laser field through the waveguide-coupled ensemble, which puts the experiment in the low-excitation regime. Specifically, we assume that at any given time no more than a single excitation is shared between the waveguide mode and the atomic ensemble. In this case, the system's response is linear and the atoms behave as classical Lorentz oscillators. We note, however, that the Hamiltonians presented in the following can also be applied to the case when more excitations are present.

Unidirectional Model

The first case we want to discuss is when light makes a single pass through an ensemble of N two-level emitters coupled to a single-mode waveguide, a typical waveguide QED case, as shown in Figure 2.6. For now, we consider only unidirectional propagation and emission, meaning that light only propagates in one direction within the waveguide and that atoms scatter light only in this direction. We will see that this assumption accounts for most phenomena observed in our experiments as forward emission is collectively enhanced [42] and the atom–waveguide interaction is in general direction dependent [65] such that the atoms preferentially emit in forward direction. The

real-space, non-Hermitian Hamiltonian describing the system takes the following form [48]

$$\begin{aligned}\frac{\hat{H}}{\hbar} = \int_{-\infty}^{\infty} \Big\{ \hat{a}_z^\dagger \left(\omega - i v_g \frac{\partial}{\partial z}\right) \hat{a}_z \\ + \sum_{n=1}^{N} \delta(z - z_n) \Big[\Omega_{a,n} \hat{\sigma}_n^+ \hat{\sigma}_n^- \\ + V_n \left(\hat{\sigma}_n^+ \hat{a}_z + \hat{\sigma}_n^- \hat{a}_z^\dagger \right) \Big] \Big\} dz \,,\end{aligned} \tag{2.1}$$

where $\hat{a}_z^\dagger$ and $\hat{a}_z$ are the photon creation and annihilation operators of the field at position z and $\hat{\sigma}_n^+$ and $\hat{\sigma}_n^-$ are the raising and lowering operator of the nth atom at position z_n. ω is the probe light frequency, v_g is the group velocity of the waveguide mode, and $\Omega_{a,n} = \omega_a - i(1 - \beta_n)\frac{\Gamma_o}{2}$, where ω_a is the emitter's transition frequency and the factor $-i(1-\beta_n)\frac{\Gamma_o}{2}$ describes losses due to spontaneous emission into free space. Γ_o is the natural linewidth of the emitter and β_n is the beta factor of the nth atom. The coupling strength of the nth emitter to the propagating field is given by $V_n = \sqrt{v_g \beta_n \Gamma_o}$.

The β factor is a crucial parameter in our system. It represents the amount of light that is scattered by an atom into the guided mode of the nanofiber. It is defined as the ratio between the emission rate of an atom into the nanofiber and the total emission rate of an atom in free space Γ_o:

$$\beta = \Gamma_\mathrm{f} / \Gamma_o \,, \tag{2.2}$$

where we only consider emission into the forward-propagating guided mode with rate Γ_f. The β factor depends on the position of the individual atoms with respect to the nanofiber in both radial and azimuthal directions, as it depends on the overlap of the radiation mode of the atom and the guided mode of the fiber, see Figure 2.2.

By solving the time-independent Schrödinger equation, we can find solutions for several quantities that are important for our description of the experimental system. The generic state $|\psi\rangle$ of the coupled system for a single excitation in the system can be written as

$$|\psi\rangle = \int_{-\infty}^{\infty} \left[\varphi(z) \hat{a}_z^\dagger + \sum_{n=1}^{N} \delta(z - z_n) \phi_n \hat{\sigma}_n^+ \right] dz \, |0\rangle \,, \tag{2.3}$$

with $\varphi(z)$ as the probability amplitude of finding a photon at position z and ϕ_n as the probability amplitude of finding the nth atom in the excited state. The initial state of the coupled system is $|0\rangle = \left|0_\mathrm{ph}\right\rangle \otimes |g_1, ..., g_N\rangle$, with $\left|0_\mathrm{ph}\right\rangle$ as the vacuum state of the system and $|g_1, ..., g_N\rangle$ as the state where all atoms are in the ground state.

By solving the Schrödinger equation corresponding to the Hamiltonian in Equation (2.1), we can calculate the photon amplitudes after each atom $\varphi_0, \varphi_1, ...\varphi_N$, which can be expressed as $\varphi_n = t_{1,n}\varphi_{n-1}$. From this, we can find the steady-state amplitude transmission coefficients past the nth atom as

$$t_{1,n}(\Delta) = 1 - \frac{\beta_n \Gamma_o}{\frac{\Gamma_o}{2} + i\Delta}\,. \tag{2.4}$$

The amplitude transmission coefficient through an ensemble made up of N single atoms in our cascaded interaction model can then be obtained as the product of the transmission coefficients past N single atoms

$$t_N(\Delta) = \prod_{n=1}^{N} t_1(\Delta) = \prod_{n=1}^{N} \left(1 - \frac{\beta_n \Gamma_o}{\frac{\Gamma_o}{2} + i\Delta}\right) \overset{\beta_n = \beta}{=} \left(1 - \frac{\beta \Gamma_o}{\frac{\Gamma_o}{2} + i\Delta}\right)^N . \tag{2.5}$$

In this last step, we assume an average atom-light coupling strength, β, for all atoms. While this simplification does not account for the actual variation in the atomic positions relative to the nanofiber, which results in a distinct β_n for each atom, the predictions obtained under this assumption are consistent with the results averaged over many experimental runs.

From the solutions of the Schrödinger equation, the excited state amplitude $\phi_n(t)$ of the nth atom can be calculated as

$$\phi_n(t) = \mathcal{F}^{-1}\left\{ i \frac{\sqrt{v_g}}{\sqrt{\beta \Gamma_o}} \left[t_n(\Delta) - t_{n-1}(\Delta) \right] u_{\text{in}}(\Delta) \right\}, \tag{2.6}$$

with $u_{\text{in}}(\Delta) = \mathcal{F}\left[u_{\text{in}}(t)\right]$ as the Fourier transform of the input excitation field with scalar amplitude, $u_{\text{in}}(t)$. $\mathcal{F}^{-1}$ denotes the inverse Fourier transform in this context.

The time dynamics of the transmitted optical field $u_{\text{out}}(t)$ can be obtained from

$$u_{\text{out}}(t) = \mathcal{F}^{-1}\left[u_{\text{in}}(\Delta) \cdot t_N(\Delta) \right], \tag{2.7}$$

which, in the single-excitation regime, depends only on the input excitation field, $u_{\text{in}}(\Delta)$, and the amplitude transmission coefficient through N atoms, $t_N(\Delta)$.

We want to point out that the transmitted optical field, $u_{\text{out}}(t)$, can also be described as the interference of the incoming excitation field,

$u_{\text{in}}(t)$, and the light scattered by all atoms into the waveguide, $\chi_N(t)$. The fields are thus summed up as $u_{\text{out}}(t) = u_{\text{in}}(t) + \chi_N(t)$, with:

$$\chi_N(t) = \sum_{n=1}^{N} \frac{\sqrt{\beta_n \Gamma_o}}{i\sqrt{v_g}} \phi_n(t) \,. \tag{2.8}$$

The total transmitted light power through the system is then simply the amplitude square of the optical output field

$$P(t) = |u_{\text{out}}(t)|^2 \,. \tag{2.9}$$

Bidirectional Model

The unidirectional model assumes that atoms scatter light into the waveguide only in the forward direction and thus cannot account for the backward reflected light that we observe in our experiments. Therefore, a more general model that allows for scattering of photons in both the forward and backward directions is necessary to describe related effects. The corresponding Hamiltonian can be formulated as

$$\begin{aligned} \frac{\hat{H}}{\hbar} = \int_{-\infty}^{\infty} \Big\{ \hat{a}^\dagger_{z,\rightarrow} \left(\omega - i v_g \tfrac{\partial}{\partial z}\right) \hat{a}_{z,\rightarrow} + \hat{a}^\dagger_{z,\leftarrow} \left(\omega + i v_g \tfrac{\partial}{\partial z}\right) \hat{a}_{z,\leftarrow} + \\ \sum_{n=1}^{N} \delta(z - z_n) \Big[\Omega_{a,n} \hat{\sigma}^+_n \hat{\sigma}^-_n + V_n \left(\hat{\sigma}^+_n \hat{a}_{z,\rightarrow} + \hat{\sigma}^-_n \hat{a}^\dagger_{z,\rightarrow} + \right. \\ \left. \hat{\sigma}^+_n \hat{a}_{z,\leftarrow} + \hat{\sigma}^-_n \hat{a}^\dagger_{z,\leftarrow} \right) \Big] \Big\} \, dz \,, \end{aligned} \tag{2.10}$$

where $\rightarrow$ represents the forward direction and $\leftarrow$ the backward direction. For example, $\hat{a}^\dagger_{z,\rightarrow}$ represents the creation operator for a photon propagating in the forward direction at position z. In this model, we assume that the coupling strength between the atoms and the light field is direction independent, such that $\beta_n = \beta_{n,\rightarrow} = \beta_{n,\leftarrow}$. Consequently, the parameter $V_n = \sqrt{v_g \beta_n \Gamma_o}$ is identical for forward and backward propagating light. All other operators and quantities are the same as in the Hamiltonian of the unidirectional model in Equation (2.1).

The state of the system for a single excitation can be written as

$$\begin{aligned} |\psi\rangle = \int_{-\infty}^{\infty} \Big[\varphi_{\rightarrow}(z) \hat{a}^\dagger_{z,\rightarrow} + \varphi_{\leftarrow}(z) \hat{a}^\dagger_{z,\leftarrow} \\ + \sum_{n=1}^{N} \delta(z - z_n) \phi_n \hat{\sigma}^+_n \Big] dz \, |0\rangle \,, \end{aligned} \tag{2.11}$$

where $\varphi_{\rightarrow}(z)$ and $\varphi_{\leftarrow}(z)$ are the probability amplitudes of finding a photon propagating in forward and backward direction at position z, respectively.

By solving the Schrödinger equation associated with the Hamiltonian in Equation (2.10), we can again find the amplitude transmission coefficient in the same way as in Equation (2.4), and the amplitude reflection coefficient for a single atom can then be calculated as

$$r_{1,n}(\Delta) = -\frac{\beta_n \Gamma_o}{\frac{\Gamma_o}{2} + i\Delta} \,. \tag{2.12}$$

For an arbitrary number of atoms, it is useful to define the two quantities $t_n = \varphi_{\rightarrow,n+1}/\varphi_{\rightarrow,n}$ and $s_n = \varphi_{\leftarrow,n}/\varphi_{\rightarrow,n}$. $\varphi_{\leftarrow,n}$ indicates the field right before the nth atom propagating in the backwards direction and $\varphi_{\rightarrow,n}$ the field right after the nth atom propagating in the forwards direction. By solving the Schrödinger equation, we can derive recursive equations for these two quantities

$$t_n(\Delta) = 1 - \frac{\beta_n \Gamma_o + \beta_n s_{n+1} e^{-2ikz_n} \Gamma_o}{\frac{\Gamma_o}{2} + i\Delta + \beta_n s_{n+1} e^{-2ikz_n} \Gamma_o} \,, \tag{2.13}$$

$$s_n(\Delta) = (t_{1,n} - 1) e^{2ikz_n} + s_{n+1} t_{1,n} \,. \tag{2.14}$$

As we excite the system only in forward direction, the field propagating in the backwards direction towards the Nth atom is zero and therefore $s_{N+1} = 0$. These equations can thus be solved recursively for all N atoms and the ensemble amplitude transmission and reflection be calculated as

$$t_N(\Delta) = \prod_{n=1}^{N} t_n(\Delta) \,, \tag{2.15}$$

$$r_N(\Delta) = s_1(\Delta) \,. \tag{2.16}$$

The detected powers are again computed using Equations (2.7) and (2.9) by appropriately replacing the amplitude transmission and reflection.

Comparison of Unidirectional and Bidirectional Propagation Model

In our system, the spatial arrangement of the atoms is unknown and varies with each experimental run. These variations lead to changes in both the relative phase between individual atomic emissions and the β factor of each atom. For the unidirectional model, the relative axial distances between the atoms are not relevant because the excitation laser field imposes a fixed phase relationship on the atomic emissions. As a result, when calculating the output fields after multiple experi-

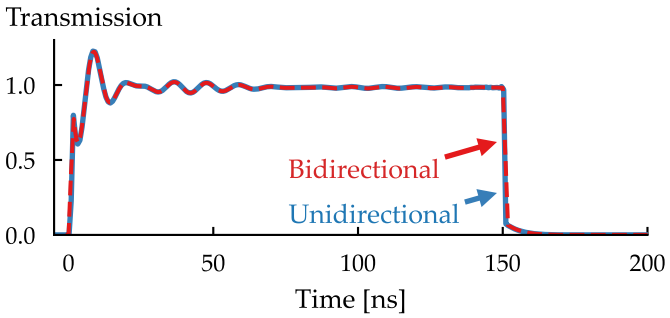

Figure 2.7: A comparison of the predictions for the transmission with the unidirectional and bidirectional model for a 150-ns-long pulse propagating through an atomic ensemble with optical depth OD = 19.3 and laser–atom detuning $\Delta = 17.3\Gamma_o$ shows a negligible difference between the two.

mental runs, it is sufficient to assume an average coupling rate β to determine the output fields. This simplifies the calculations since we do not have to average over the specific spatial arrangement of the atoms. On the other hand, for the bidirectional model, the relative axial positions of the atoms become significant as atoms can also scatter in backward direction, making the relative phases a relevant factor in the calculation. Consequently, we must average over multiple random atomic configurations to obtain accurate results, which makes the bidirectional model more computationally intensive than the unidirectional model. While for calculating the backward reflected light, a bidirectional treatment is essential to accurately capture the dynamics, the unidirectional model is sufficient for forward emission, as long as β is small and atoms are not periodically arranged at Bragg condition.

In a strict sense, unidirectional propagation of light is only an accurate representation in the case of chiral coupling, i.e., perfectly unidirectional coupling, between atoms and the propagating mode [65]. Nonetheless, our unidirectional model is still applicable for describing both the forward-scattered field and the atomic population dynamics in scenarios involving symmetric (non-chiral) coupling as long as the backward-scattered field amplitudes do not add up coherently. This criterion is met when atom are arranged randomly along the fiber, and also when they are arranged periodically, as is the case for trapped atoms. For a periodic arrangement, the spacing between atoms, Δz, must, however, sufficiently deviate from the Bragg condition, i.e., $\Delta z = n\frac{\lambda}{2}$, where n is a positive integer and λ is the wavelength of the probe light. For our situation, the ratio of backward emission to forward emission is on the order of 1:100. Additionally, even a single isolated atom preferentially couples to the

forward-propagating mode due to the chiral light-matter interaction in the evanescent field around a nanofiber [65, 66].

To illustrate that a unidirectional propagation model is appropriate for describing light transmission in forward direction in our experimental setting, we numerically compare the predictions of the unidirectional and the bidirectional model in Figure 2.7 for a 150-ns-long pulse propagating through an ensemble with OD = 19.3 and $\Delta = 17.3\Gamma_0$, i.e., the same situation as in the experiment depicted in Figure 3.3(a). For the calculation of the bidirectional model, we assume the atoms to be randomly distributed along the axis of the nanofiber, but to all have the same average light-atom coupling strength $\beta_n = \beta = 0.55\%$, as found in our experiment [62]. The depicted results shown for the bidirectional model are averaged over 10^4 random atom configurations. Given the negligible difference in the calculated temporal responses between the two models, we can confirm that for forward propagating light, the unidirectional propagation model is sufficient.

2.2.2 Light-Matter Interaction in Resonators

In our experimental setup, the nanofiber is part of a fiber-ring resonator. In order to correctly describe the atom–light interaction in this system, the theoretical model presented in the previous section requires an extension to include the resonator.

Jaynes-Cummings and Tavis-Cummings Model

The textbook case to describe the interaction of light with a quantum emitter in a cavity is based on the Jaynes-Cummings model [13] and its extension for multiple emitters, the Tavis-Cummings model [67, 68]. The Jaynes-Cummings model assumes a single two-level atom that is coupled to a single frequency mode of a cavity, where the Hamiltonian in the rotating wave approximation is given by

$$\frac{\hat{H}}{\hbar} = \omega_c \hat{a}^\dagger \hat{a} + \omega_a \hat{\sigma}^+ \hat{\sigma}^- + g\left(\hat{a}^\dagger \hat{\sigma}^- + \hat{a}\hat{\sigma}^+\right). \tag{2.17}$$

In this equation, ω_a and ω_c are the atomic and cavity resonance frequencies, $\hat{a}^\dagger$ and $\hat{a}$ the photon creation and annihilation operators, and σ^+ and σ^- the atomic raising and lowering operators. Here, the vacuum energy is omitted, and the zero point of the atomic energy is set to the ground state energy. The parameter $g = g_1$ represents the single-emitter–single-photon coupling strength in the Jaynes-Cummings model. The Tavis-Cummings model extends the Jaynes-Cummings model to N coupled emitters, where the coupling strength is enhanced to $g = \sqrt{N} g_1$.

Diagonalizing the Hamiltonian of the coupled system reveals an infinite number of eigenstates, which appear as pairs of states coupled by the interaction, the so-called dressed states, with energies

$$E_n^{\pm}(\Delta) = \left(n + \frac{1}{2}\right)\hbar\omega \pm \frac{\hbar}{2}\Omega_n(\Delta) \tag{2.18}$$

with $\Omega_n(\Delta) = \sqrt{4g^2(n+1) + \Delta^2}$ [69]. The lowest coupled pair for $n = 0$ photons in the cavity, is split by a frequency difference of $2g$ on resonance, corresponding to the familiar vacuum Rabi splitting [19].

To accurately describe the probing of a coupled atom–cavity system, the Hamiltonian has to be extended to include the coupling of an external probing light field with the cavity. Additionally, to account for losses in the cavity and spontaneous emission into free-space, complex atomic and cavity resonance frequencies are introduced. In the low saturation regime and in the steady state, solving the Schrödinger equation of the Hamiltonian allows us to calculate the amplitude transmission of the coupled ensemble–cavity system for the case of N atoms using the Tavis-Cummings (TC) model [48]:

$$t_{\mathrm{TC}}(\Delta) = \frac{g^2 + [(1-\beta)\Gamma_o/2 + i\Delta]\,[\kappa_0 - \kappa_{\mathrm{ext}} + i\Delta_c]}{g^2 + [(1-\beta)\Gamma_o/2 + i\Delta]\,[\kappa_0 + \kappa_{\mathrm{ext}} + i\Delta_c]}\,. \tag{2.19}$$

Here, $\Delta_c = \omega - \omega_c = \Delta + \omega_a - \omega_c$ represents the detuning of the probe field from the cavity resonance and κ_0 and κ_{ext} denote the intrinsic loss rate of the cavity and the external coupling rate into and out of the cavity. Using this transmission coefficient, we can calculate the response of the system to an incoming light field with amplitude $u_{\mathrm{in}}(t)$ equivalently to Equations (2.7) and (2.9).

The Jaynes-Cummings and Tavis-Cummings model have been instrumental in describing the behavior for a range of systems that are coupled to cavities, such as atoms [15, 17, 19], Bose-Einstein condensates [50, 70], molecules [71], quantum dots [33] and superconducting qubits [72].

However, a key assumption of the Jaynes-Cummings and Tavis-Cummings model is that the emitters interact with only a single mode of the cavity, even though most optical cavities support an infinite number of discrete frequency modes. For the Jaynes-Cummings and Tavis-Cummings model to remain valid, the resonator's free spectral range, ν_{FSR}, must be significantly larger than any other frequency in the system, specifically, larger than the natural linewidth of the emitter, Γ_o, and the emitter–resonator coupling strength, g. Additionally, due to the fact that these models assume that the cavity field reacts instantaneously to the presence of an atom, the single-pass optical depth must be small (OD $\ll 2$) [48]. If the optical depth is too large, the

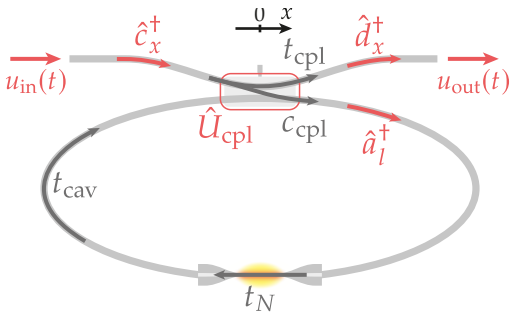

Figure 2.8: A sketch of the ring resonator together with all relevant quantities given in the Hamiltonian.

resonator field is modified upon a single pass through the ensemble, causing emitters further along the propagation direction to experience a different field.

Extension of Cascaded Interaction Model to Includes a Resonator

The atom–resonator system in our experiment falls outside the validity range of the Jaynes-Cummings and Tavis-Cummings models as we couple many emitters with large optical depth to very long cavities. Consequently, the free spectral range is comparable to the linewidth of cesium and the atoms couple to multiple longitudinal cavity modes. To accurately describe our system for all parameter ranges, we therefore modify the cascaded interaction model to include a resonator.

The Hamiltonian describing the ring-resonator system is an extension of the one in Equation (2.1), but it involves additional terms to account for the light fields in the coupling waveguide, i.e., the incoming and outgoing light fields, as well as the coupling of these fields into and out of the resonator via a fiber coupler. A sketch of the situation and the involved fields and transmission coefficients is given in Figure 2.8. We assume solely unidirectional propagation of light as discussed previously in Section 2.2.1 such that the resulting Hamiltonian reads [48, 55]:

$$\begin{aligned}\frac{\hat{H}}{\hbar} = \hat{U}_{\mathrm{cpl}} &+ \int_{-\infty}^{0}\left[\hat{c}_x^\dagger\left(\omega - iv_g\frac{\partial}{\partial x}\right)\hat{c}_x\right]dx \\ &+ \int_{0}^{\infty}\left[\hat{d}_x^\dagger\left(\omega - iv_g\frac{\partial}{\partial x}\right)\hat{d}_x\right]dx \\ &+ \int_{0}^{L}\Bigg\{\hat{a}_l^\dagger\left(\omega + iv_g\frac{\partial}{\partial l}\right)\hat{a}_l \\ &\quad + \sum_{n=1}^{N}\delta(l-l_n)\Big[\Omega_a\hat{\sigma}_n^+\hat{\sigma}_n^- \\ &\qquad + V\left(\hat{\sigma}_n^+\hat{a}_l + \hat{\sigma}_n^-\hat{a}_l^\dagger\right)\Big]\Bigg\}\,dl\,.\end{aligned} \tag{2.20}$$

In this description, the light field propagating inside the resonator of length L at position l is represented by the photon creation and annihilation operators $\hat{a}_l^\dagger$ and $\hat{a}_l$ and the rest of the operators are the same as in Equation 2.1, but assuming the same β for all emitters, which is the reason for the missing subscript n on the operators when comparing to the previous, more general, description.

The resonator interacts with incoming and outgoing fields characterized by the creation and annihilation operators, $\hat{c}_x^\dagger$ and $\hat{c}_x$, as well as $\hat{d}_x^\dagger$ and $\hat{d}_x$, respectively. These fields couple into and out of the resonator at the fiber coupler, which is modeled by a unitary operator $\hat{U}_{\mathrm{cpl}}$ corresponding to the action of a beamsplitter. The resulting coupler matrix $\hat{U}_{\mathrm{cpl}}$ is given by

$$\begin{aligned}\hat{U}_{\mathrm{cpl}} &= i v_g t_{\mathrm{cpl}} \hat{c}_{\mathrm{o}} \hat{d}_{\mathrm{o}}^\dagger + v_g c_{\mathrm{cpl}} \hat{c}_{\mathrm{o}} \hat{a}_{\mathrm{o}}^\dagger \\ &+ t_{\mathrm{cav}} \left(i v_g t_{\mathrm{cpl}} \hat{a}_L \hat{a}_{\mathrm{o}}^\dagger + v_g c_{\mathrm{cpl}} \hat{a}_L \hat{d}_{\mathrm{o}}^\dagger \right) .\end{aligned} \tag{2.21}$$

In this matrix, the subscripts on the operators indicate their respective positions within their coordinate systems so that $\hat{a}_L$, for instance, refers to the annihilation operator in the cavity at position $l = L$, where L is the length of the cavity. It thus describes a cavity photon that is annihilated when it reaches the coupler after one roundtrip. t_{cpl} and c_{cpl} denote the amplitude transmission and coupling coefficients of the coupler, satisfying the relation $|t_{\mathrm{cpl}}|^2 + |c_{\mathrm{cpl}}|^2 = 1$. Additionally, t_{cav} represents the amplitude transmission of the cavity over a single roundtrip. These quantities can be related to the typical quantities used in cavity QED as

$$\begin{aligned} t_{\mathrm{cpl}} = \sqrt{1 - \frac{2\kappa_{\mathrm{ext}}}{\nu_{\mathrm{FSR}}}}, \quad c_{\mathrm{cpl}} = \sqrt{\frac{2\kappa_{\mathrm{ext}}}{\nu_{\mathrm{FSR}}}} \\ t_{\mathrm{cav}} = \sqrt{1 - \frac{2\kappa_{\mathrm{o}}}{\nu_{\mathrm{FSR}}}} . \end{aligned} \tag{2.22}$$

where κ_{ext} is the coupling rate to the cavity, κ_{o} is the intrinsic loss rate of the resonator and $\nu_{\mathrm{FSR}} = v_g / L_{\mathrm{cav}}$ is the free spectral range of the resonator with length L_{cav} and v_g as the group velocity of light in the resonator.

The general state of the system for a single excitation that is coupled to the resonator via the coupling waveguide can be described by

$$\begin{aligned} |\psi\rangle = \Bigg[&\int_{-\infty}^{0} \varphi_c(x)\, \hat{c}_x^\dagger dx + \int_{0}^{\infty} \varphi_d(x)\, \hat{d}_x^\dagger dx \\ &+ \int_{0}^{L} \left(\varphi_a(l)\, \hat{a}_l^\dagger + \sum_{n=1}^{N} \delta(l - l_n) \phi_n \hat{\sigma}_n^+ \right) dl \Bigg] |0\rangle , \end{aligned} \tag{2.23}$$

where $\varphi_c(x)$, $\varphi_d(x)$ and $\varphi_a(l)$ are the probability amplitudes of finding a photon in the incoming or outgoing arm of the coupling waveguide at position x and inside the resonator at position l, respectively. ϕ_n is the probability amplitude of finding the nth atom at position l_n in the excited state.

By inserting this state into the eigenvalue problem $\hat{H}\,|\psi\rangle = E\,|\psi\rangle$, we can solve the time-independent Schrödinger equation and derive the transmission amplitude through the whole system as [48]

$$t(\Delta) = \frac{e^{-i\Delta_c/\nu_{\mathrm{FSR}}} t_{\mathrm{cav}} t_N(\Delta) - t_{\mathrm{cpl}}}{e^{-i\Delta_c/\nu_{\mathrm{FSR}}} t_{\mathrm{cav}} t_N(\Delta) t_{\mathrm{cpl}} - 1}\,, \tag{2.24}$$

where $\Delta_c = \omega - \omega_c = \Delta + \omega_a - \omega_c$ represents the detuning of probe light from the frequency of the cavity resonance nearest to the atomic resonance frequency ω_a. In our experiments $\Delta_c \approx \Delta$ because we tune the cavity into resonance with the atoms. Furthermore, $t_N(\Delta)$ is the single-pass amplitude transmission through the ensemble of N atoms as given in Equation (2.5).

When probing the resonator with a pulse $u_{\mathrm{in}}(t)$, we can calculate the output field $u_{\mathrm{out}}(t)$ that is transmitted through the coupled ring-resonator by first calculating the frequency distribution of the pulse as $u_{\mathrm{in}}(\Delta) = \mathcal{F}\left[u_{\mathrm{in}}(t)\right]$. The output state is then obtained from the inverse Fourier transform as $u_{\mathrm{out}}(t) = \mathcal{F}^{-1}\left[u_{\mathrm{in}}(\Delta)\cdot t(\Delta)\right]$. The total transmitted power through the system is again simply the modulus squared of $u_{\mathrm{out}}(t)$.

Another important quantity that we consider in our discussion is the intracavity field in the resonator after passing through the atoms. The amplitude of this field, $E_{\mathrm{cav}}(\Delta)$, just before light exits through the fiber coupler can be calculated for an input field $u_{\mathrm{in}}(t)$ as

$$E_{\mathrm{cav}}(\Delta) = \frac{i t_N(\Delta)}{e^{-i\Delta_c/\nu_{\mathrm{FSR}}} t_{\mathrm{cav}} t_N(\Delta) t_{\mathrm{cpl}} - 1} \mathcal{F}\left[u_{\mathrm{in}}(t)\, c_{\mathrm{cpl}}\right]\,. \tag{2.25}$$

The time-domain representation of the resonator field is then given by the inverse Fourier transform of this quantity, $E_{\mathrm{cav}}(t) = \mathcal{F}^{-1}\left[E_{\mathrm{cav}}(\Delta)\right]$.

3 COLLECTIVE RADIATIVE DYNAMICS

The results presented in this chapter have been published in [64]:
Riccardo Pennetta, Martin Blaha, Aisling Johnson, Daniel Lechner, Philipp Schneeweiss, Jürgen Volz, and Arno Rauschenbeutel.
Collective Radiative Dynamics of an Ensemble of Cold Atoms Coupled to an Optical Waveguide.
Physical Review Letters, 128(7):073601, 2022.

Dicke's seminal work [73] laid the foundation for research into collective effects among quantum emitters. It introduced a comprehensive framework for calculating the spontaneous emission of a cloud of N two-level emitters that are confined in a space smaller than their emission wavelength λ, a situation illustrated in 3.1(a). When one photon excites this system, the excitation is shared among the atoms in the ensemble, causing the ensemble to exhibit superradiant emission, i.e., emission with a decay rate faster than that of an isolated emitter. In this case, the ensemble is prepared in what is called the *Dicke state*:

$$|D\rangle = \frac{1}{\sqrt{N}} \sum_{n=1}^{N} |n\rangle \,, \tag{3.26}$$

where $|n\rangle$ denotes the state in which only the nth atom is excited, while the other atoms remain in the ground state. The excitation is thus coherently distributed among all atoms in the ensemble and it is

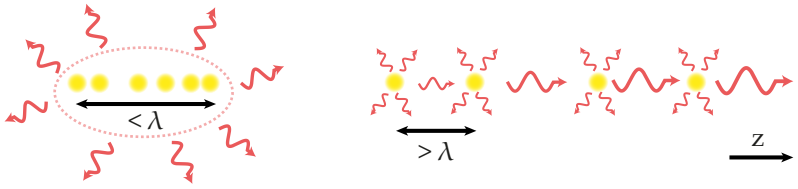

(a) Dicke state **(b)** Timed Dicke state

Figure 3.1: Illustration of a one-dimensional, atomic ensemble prepared in **(a)** a Dicke state and in **(b)** a timed Dicke state, where the arrows refer to the respective emission properties. In the Dicke state, all emission amplitudes interfere constructively leading to superradiant emission, while in the timed Dicke state, constructive interference only occurs in the $+z$-direction.

not known which of the atoms is excited. However, the phenomenon of superradiance does not depend on the atoms being indistinguishable, i.e., all of them being in approximately the same position. Instead, it relies on the fact that it is impossible to distinguish from which atom a photon was emitted. Consequently, if all emitters couple to the same optical mode, as in a waveguide, superradiance can occur. In light of this understanding, the phenomena originally outlined by Dicke are also observable in extended ensembles with length scales greater than λ [43], a scenario that more closely matches many experimental setups as long as there is a common optical mode. Super- and also subradiance have been observed in a variety of systems such as cold atom clouds [36, 40, 44, 74–78], Rydberg atoms [79, 80] and ensembles of nuclei [81].

The excitation of extended ensembles by absorption of a photon with a wavevector $\boldsymbol{k}$ prepares a *timed Dicke state*:

$$|TD\rangle = \frac{1}{\sqrt{N}} \sum_{n=1}^{N} e^{i\boldsymbol{k}\cdot\boldsymbol{r}_n} |n\rangle \ , \tag{3.27}$$

where $\boldsymbol{r}_n$ denotes the position of the nth atom. This state is characterized by spatial phase factors $e^{i\boldsymbol{k}\cdot\boldsymbol{r}_n}$ due to the propagation of the exciting photons through the ensemble, which break the state's symmetry. In the timed Dicke state (see Figure 3.1(b)), the atoms are all initially excited with the same probability. This system exhibits enhanced collective emission of light in the direction of the exciting optical mode with wavevector $\boldsymbol{k}$ as the emission from different atoms are *timed* such that they constructively interfere as depicted in Figure 3.1(b) [43].

Recent theoretical work has explored the non-trivial time evolution of this state in three-dimensional disordered atomic clouds [82, 83]. The findings in such complex systems, however, do not lead to an intuitive understanding of the microscopic dynamics of individual atoms. We therefore take a step back and explore these issues in a one-dimensional system, which is experimentally realized with an ensemble of cold atoms interfaced via a single-mode optical nanofiber. Our theoretical analysis based on the cascaded interaction model provides insight into the emergence of the phenomena of superradiance and collective Rabi oscillations [84] on a microscopic, atom-by-atom scale. This analysis demonstrates that these phenomena gradually build up along the atomic ensemble in the direction of light propagation. This dynamics is independent of the spacing between the atoms, except for atoms arranged in the Bragg condition.

This chapter begins with a description of the experimental setup where we excite an atomic ensemble with a boxcar-shaped light pulse.

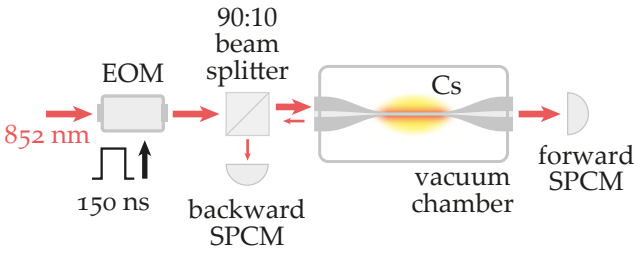

Figure 3.2: Scheme of the experimental setup, where 150-ns-long excitation pulses are launched into an optical fiber containing a nanofiber section. A cloud of cesium (Cs) atoms (in yellow) from a magneto-optical trap interacts with the pulse in the evanescent field of the nanofiber and the forward transmitted and backward reflected light is collected on a single photon counting module (SPCM).

We then analyze the temporal dynamics of the transmitted light and discuss the observed collective Rabi oscillations that emerge at the switch-on of the pulse and the superradiant decay of the ensemble after the pulse switches off. We examine the superradiant emission in more detail by varying the optical depth of the ensemble and the effect of detuning the excitation pulse. The chapter concludes with an investigation of the dynamics observed when the pulse passes repeatedly through the same ensemble in our cavity system.

3.1 EXPERIMENTAL SETUP

The schematic experimental setup used for our measurements is depicted in Figure 3.2. Cesium atoms are loaded into a MOT and the atomic cloud is overlapped with the nanofiber section of an optical fiber. When light is launched into this fiber, it interacts with the atoms through the evanescent field that extends into free space around the fiber. In this experiment, the variable fiber coupler of the resonator was set to be completely overcoupled, causing light to only make a single pass through the ensemble. We probe the atomic ensemble with 150-ns-long boxcar-shaped light pulses resonant with the D_2 transition of cesium ($6S_{1/2}$, $F = 4 \rightarrow 6P_{3/2}$, $F' = 5$). These pulses are prepared with an EOM as detailed in Section 2.1.3 and their rise and fall times of around 1 ns are much shorter than the excited state lifetime of cesium atoms of $2\pi/\Gamma_0 = 30.4$ ns. To ensure a linear response of the atoms, the mean pulse power is much smaller than one single photon energy per atomic lifetime, i.e., on the order of 1 pW. This puts our experiment in the low saturation regime. Light transmitted through the ensemble in forward direction is detected using an SPCM. Additionally, a small part of the light is reflected by the ensemble, which is measured on

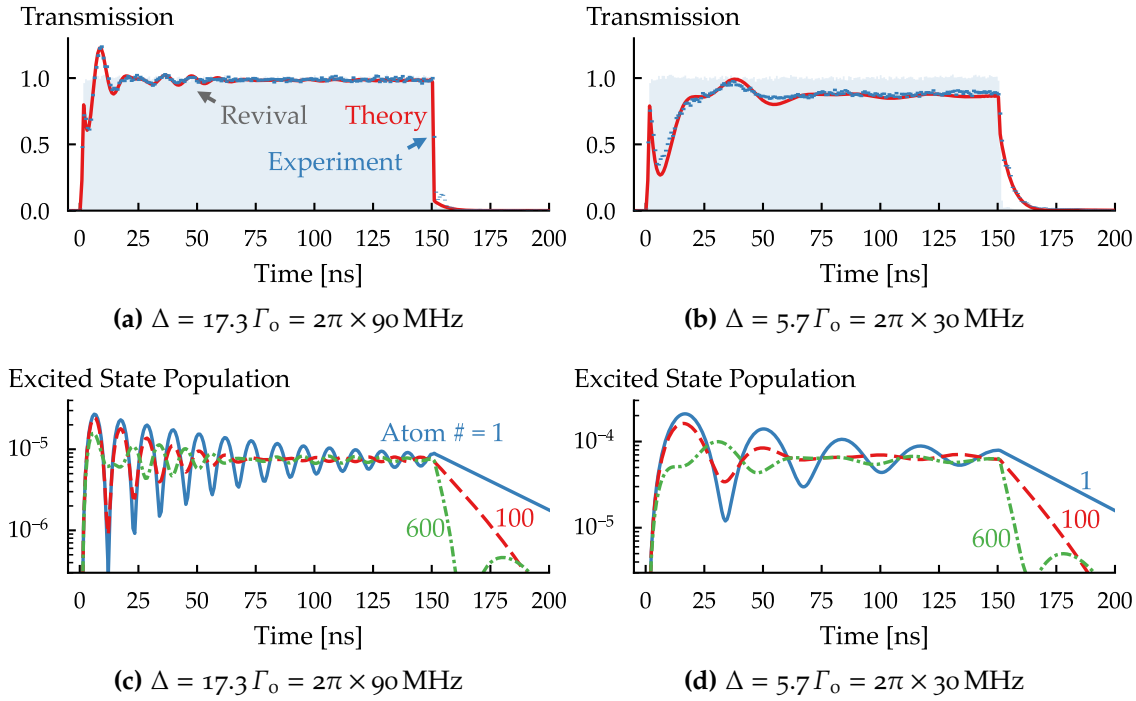

(a) $\Delta = 17.3\,\Gamma_0 = 2\pi \times 90\,\mathrm{MHz}$ **(b)** $\Delta = 5.7\,\Gamma_0 = 2\pi \times 30\,\mathrm{MHz}$

(c) $\Delta = 17.3\,\Gamma_0 = 2\pi \times 90\,\mathrm{MHz}$ **(d)** $\Delta = 5.7\,\Gamma_0 = 2\pi \times 30\,\mathrm{MHz}$

Figure 3.3: Measured transmissions through the atomic ensemble after pulsed excitation for a total optical depth of the prepared ensemble of OD = 19.3 for detunings of **(a)** $\Delta = 17.3\Gamma_0 = 2\pi \times 90\,\mathrm{MHz}$ and **(b)** $\Delta = 5.7\Gamma_0 = 2\pi \times 30\,\mathrm{MHz}$, where Γ_0 is the natural linewidth of Cs. The data was averaged over 3.75×10^6 pulses. The blue rectangles show the measured data with their height corresponding to the statistical error, and the red lines are fitted theoretical predictions. The light blue shaded area represents the transmitted optical pulse in the case when no atoms are present. Complex collective Rabi oscillations are visible after the switch-on of the pulse and superradiant decay after the switch-off. **(c)** and **(d)** show the microscopic dynamics of the excited state populations for the same detunings for the first, 100th and 600th atom in the chain.

the backward SPCM. In the experimental sequence, a cesium MOT is prepared for 3 s and then released for 0.5 ms by switching off the MOT laser fields. During this time, 50 probe pulses are launched into the fiber and detected on the SPCMs. Afterward, the MOT fields are turned on again to recapture and recool the atoms for 200 ms. The data is collected over many of these cycles and the results are averages over millions of excitation pulses.

3.2 COLLECTIVE RABI OSCILLATIONS AND MICROSCOPIC DYNAMICS

In this section, we present and discuss the collective radiative dynamics of the atomic ensemble. Figure 3.3 shows two examples where we measured the temporal response of our system following the excitation with 150-ns-long pulses. The ensemble has an optical

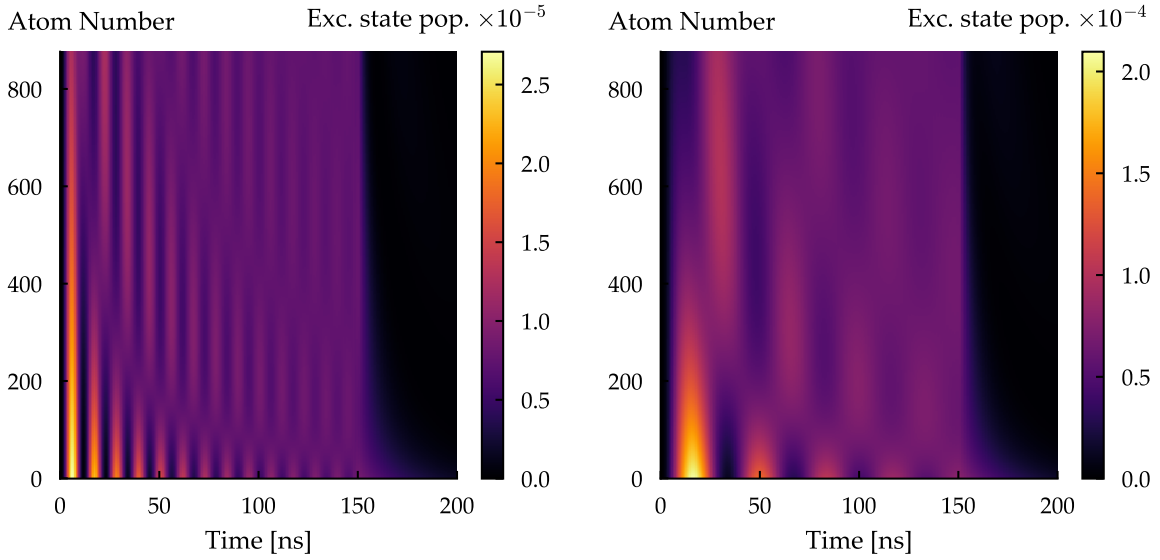

(a) $\Delta = 17.3\,\Gamma_0 = 2\pi \times 90\,\mathrm{MHz}$ **(b)** $\Delta = 5.7\,\Gamma_0 = 2\pi \times 30\,\mathrm{MHz}$

Figure 3.4: Temporal evolution of the excited state populations for individual atoms along the chain of atoms for the same parameters as in Figure 3.3. Each atom undergoes Rabi oscillations with a frequency similar to the detuning, Δ, of the probe laser field. Atoms further back in the chain are, however, excited by a field that is the sum of the probe field and the emitted field of the previous atoms, causing them to reverse their oscillation phase one or multiple times which can be clearly seen in this figure. The total complex collective dynamics in Figure 3.3 is then caused by the sum of the emission of all atoms in the chain.

depth of about OD = 19.3, i.e., it comprises about $N = 900$ atoms as $\mathrm{OD} = 4\beta N$, with an average atom–field coupling strength $\beta = 0.55\%$ [62]. We probe the ensemble with light that is detuned from the atomic resonance and show the time-resolved transmissions measured for the two detunings $\Delta = 17.3\Gamma_0 = 2\pi \times 90\,\mathrm{MHz}$ in Figure 3.3(a) and $\Delta = 5.7\Gamma_0 = 2\pi \times 30\,\mathrm{MHz}$ in Figure 3.3(b). The blue rectangles represent the measured data, with their height corresponding to the statistical error. Throughout this thesis, we assume that the clicks follow a Poissonian distribution and the errors shown in the plot indicate ± the standard deviation $\sigma = \sqrt{\#\,\mathrm{counts}}$. The red lines are theoretical predictions without free parameters with the unidirectional cascaded interaction model, as detailed in Section 2.2.1. The shaded area in light blue represents the excitation pulse, which was measured without atoms and used to normalize the measurement.

At the beginning of the pulse, the dynamics is characterized by pronounced collective Rabi oscillations. However, these oscillations are not simple damped sinusoidal oscillations as would be expected for a single atom, but they oscillate in a more complex manner. For example, the dynamics in Figure 3.3(a) shows first a collapse of the

oscillation amplitude after about 25 ns and then a subsequent revival between 30 ns to 50 ns.

To understand the origin of these complex dynamics, we calculate the microscopic, i.e., atom-by-atom dynamics of the ensemble using our cascaded interaction model. In Figures 3.3(c) and 3.3(d), we calculate the excited state populations of the first, 100th, and 600th atom in the one-dimensional chain of atoms for our system. Furthermore, the excited state populations of all atoms in the ensemble are shown in a two-dimensional map in Figure 3.4. Two distinct features emerge from this analysis: firstly, the phase of the oscillation for atoms deeper in the ensemble reverses during the pulse, and, secondly, the emergence of superradiant decay rates following the switch off of the excitation pulse.

The individual atoms in the ensemble, when excited by the probe pulse, undergo Rabi oscillations as they oscillate between their ground and excited states. The generalized Rabi frequency of the system is $\widetilde{\Omega} = \sqrt{\Omega^2 + \Delta^2}$, but as we are in the weak driving regime, the Rabi frequency Ω is much smaller than Δ and the resulting oscillation frequency is therefore close to the detuning of the drive Δ. While all atoms oscillate at the same frequency, they exhibit different amplitudes and phases, as well as oscillation collapse and revival, depending on their position in the chain. Only the first atom in the ensemble shows damped sinusoidal Rabi oscillations, behaving as if it were decoupled from the remainder of the ensemble. Subsequent atoms in the chain are driven by a field that results from the interference of the incoming probe pulse and the emitted light from the preceding atoms. Since the light emitted by atoms is π-phase shifted relative to the incoming probe light, this can lead to a reversal of the oscillation phase for atoms further along the chain. This process can repeat multiple times for atoms positioned further down the chain. For example, the 100th atom in Figure 3.3(c) reverses its oscillation phase at around 90 ns, whereas the 600th atom experiences its first reversal at approximately 15 ns, and again at about 75 ns, to eventually oscillate in phase again with the first atom. The reversal of the oscillation phase can also be observed very well in Figure 3.4, where the excited state population is plotted for every individual atom along the chain. The phase reversal can be seen at longer times for atoms earlier in the chain and at shorter times for atoms later in the chain. Consequently, each atom along the chain displays a different dynamics, in contrast to the standard Dicke case where all atoms behave identically. The system's intricate temporal dynamics is then a result of the collective effects, as the transmission through the waveguide depends on the sum of the fields scattered by each atom (see also Equation (2.8)).

3.3 MEASUREMENT OF SUPERRADIANCE

Superradiance is a phenomenon where an ensemble of atoms decays to the ground state faster than a single atom would. We observe superradiance in the measurements in Figures 3.3(a) and 3.3(b) at the moment the incident pulse switches off ($t = 150\,\mathrm{ns}$): the ensemble decays much faster than an isolated cesium atom, which decays on a time scale of $\tau_{\mathrm{at}} = 1/\Gamma_o = 30.4\,\mathrm{ns}$. This rapid decay becomes even more evident in the microscopic atom-by-atom dynamics depicted in Figures 3.3(c) and 3.3(d), where the decay rate of the first atom corresponds to that of a single atom, while the 100th and 600th atom decay increasingly faster. In Figure 3.4 this can also be observed.

In experiments, the shape of the temporal dynamics can be easily measured. By fitting an exponential to the initial decay, we can extract a decay rate. This work refers to this decay rate of the light intensity emitted into the considered mode as the *pulse decay rate*, $\Gamma_{\mathrm{pulse}}(t)$. It can be calculated from the decays of the individual atoms as

$$\Gamma_{\mathrm{pulse}}(t) = -\frac{\partial}{\partial t}\left[\log\left(\frac{|\chi_N(t)|^2}{|\chi_N(0)|^2}\right)\right] = -\frac{\frac{\partial}{\partial t}|\sum_{n=1}^{N}\phi_n(t)|^2}{\sum_{n=1}^{N}|\phi_n(t)|^2}\,. \tag{3.28}$$

In our case, $\chi_N(t)$ is the complex amplitude of the light field after passing the Nth or last atom in the chain and $\phi_n(t)$ is the excited state amplitude of the nth atom.

In some discussions on super- and subradiance [75–77, 80], the pulse decay rate, which is easy to access experimentally, is often taken as equivalent to the *collective ensemble decay rate*. However these two quantities are typically not the same. The collective decay rate of an ensemble of atoms, $\Gamma_{\mathrm{ens}}(t)$, is defined as the rate at which the total excited state population decays. This can be expressed as the ratio between the energy loss rate and the energy stored in the ensemble:

$$\Gamma_{\mathrm{ens}}(t) = -\frac{\sum_{n=1}^{N}\frac{\partial}{\partial t}|\phi_n(t)|^2}{\sum_{n=1}^{N}|\phi_n(t)|^2} = \Gamma_{\mathrm{fs}} + \Gamma_{\mathrm{ens,wg}}(t)\,, \tag{3.29}$$

where $\Gamma_{\mathrm{fs}} = (1-\beta)\Gamma_o$ is the decay rate into free space, assuming an average atom-waveguide coupling strength β. The ensemble decay rate into the waveguide, $\Gamma_{\mathrm{ens,wg}}(t)$, is defined by the ratio of the energy leaving the ensemble via the guided mode and the energy stored in the ensemble:

$$\Gamma_{\mathrm{ens,wg}}(t) = \frac{v_g|\chi_N(t)|^2}{\sum_{n=1}^{N}|\phi_n(t)|^2}\,, \tag{3.30}$$

where v_g is the group velocity of the guided mode in the waveguide.

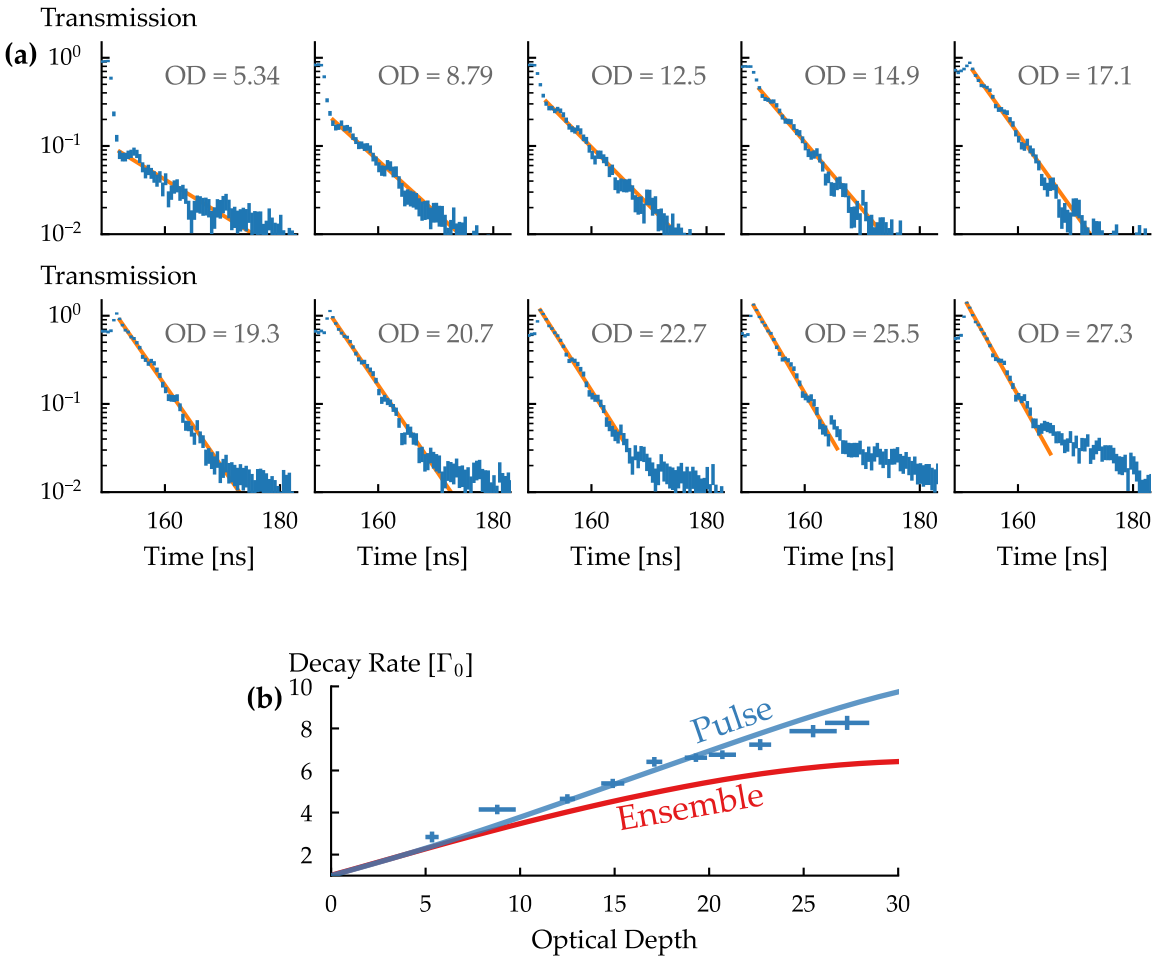

Figure 3.5: The temporal dynamics after an excitation pulse is turned off are shown for varying opticals depths and for a detuning of $\Delta = 3.8\Gamma_0 = 2\pi \times 20\,\mathrm{MHz}$. **(a)** The experimental data for increasing optical depth is shown in blue with its statistical errors, and the data is fit with an exponential fit, depicted as an orange line. **(b)** The extracted pulse decay rates are shown as a function of optical depth, where the calculated decay rates are represented by a blue solid line. The calculated ensemble decay rate into the waveguide is plotted in red. Overall, the ensemble shows superradiant decay into the waveguide with a collectively enhanced decay rate that monotonically increases with optical depth.

A comparison of Equations (3.28) and (3.29) reveals that the measured pulse decay rate and the ensemble decay rate are, in general, not the same. Estimating $\Gamma_{\mathrm{ens}}(t)$ requires knowledge of the entire state of the system, which is experimentally challenging. However, we can estimate it using the cascaded interaction model, which allows us to predict the state of each atom.

3.3.1 Superradiance as a Function of Optical Depth

To study the observed superradiant behavior in more detail, we examine the decay of the transmission through the ensemble after the

probe pulse switches off for various optical depths and extract the initial decay rate, i.e., the pulse decay rate, from an exponential fit to the data. Figure 3.5(a) shows the data in blue and the fits used to estimate the pulse decay rate in orange for optical depths ranging from OD = 5.3 to OD = 27.3 with a constant laser–atom detuning of $\Delta = 3.8\Gamma_0 = 2\pi \times 20\,\text{MHz}$ for cesium. For an optical depth up to 20.7, the data was fit over a time period of 30 ns, while for higher optical depths the period was reduced to 15 ns to account for the faster decay rates and the observation that the decay deviates from exponential behavior for later times with the appearance of a distinct shoulder in the emission. This behavior stems from the ensemble passing through a subradiant state, a feature we will discuss in more detail in the next chapter. This is also the reason why we performed this measurement with detuned light as, on resonance, the subradiant effects play a larger role, making the measurement of superradiance more difficult. The extracted pulse decay rates as a function of optical depth are plotted in Figure 3.5(b) alongside the theoretical predictions. The error bars correspond to ±1 standard deviation and the calculated pulse decay is shown as a solid blue line. The theoretical values were obtained using the same fitting procedure as for the data, but now applied to the calculated pulse.

We observe the pulse decay rate to increase by almost an order of magnitude with a nearly linear relationship in the optical depth. An increased pulse decay rate alone does not indicate superradiance, however, as we have discussed at the beginning of this section. The quantity that we compare to is the aforementioned collective ensemble decay rate Γ_{ens} or, in our experiment, the ensemble decay rate into the waveguide $\Gamma_{\text{ens,wg}}$. Determining Γ_{ens} or $\Gamma_{\text{ens,wg}}$ requires averaging of the decay rates of the individual atoms, weighted by their excited state amplitudes, as illustrated in Figures 3.3(c), 3.3(d) and 3.4. The red line in Figure 3.5(b) depicts this calculated ensemble decay rate into the waveguide $\Gamma_{\text{ens,wg}}$ as a function of optical depth. This rate also exceeds the natural decay rate Γ_o of the ensemble, indicating superradiant emission.

We also observe that the ensemble decay rate saturates at large optical depths, where it no longer increases linearly. This occurs because the ensemble absorbs so much light that adding more atoms to the interaction has little additional impact on the interaction. However, in the case of the pulse decay rate, these additional atoms absorb the emitted light from the ensemble, resulting in an increased observed decay rate.

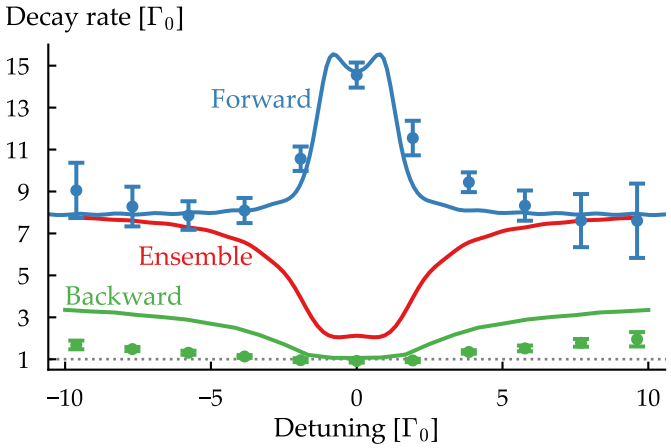

Figure 3.6: The measured and predicted pulse decay rates in forward and backward direction are shown as blue and green filled circles and lines, respectively, for OD = 26 as a function of detuning. The ensemble decay rate in forward direction is shown as a solid red line and deviates most from the pulse decay rate around resonance while it approaches the measured decay rates for larger detunings, when the ensemble is being prepared in a timed Dicke state.

3.3.2 Superradiance as a Function of Detuning

To understand better why the pulse decay rate in Figure 3.5(b) approaches the ensemble decay rate only for low optical depth, we also examine the superradiant behavior as a function of detuning. Figure 3.6 illustrates the measured pulse decay rates in forward and backward direction and the calculated ensemble decay rate in forward direction for an optical depth of OD = 26. Here, forward and backward direction refers to the propagation direction of the probe light. The difference between the measured pulse decay rate and the ensemble decay rate is largest on resonance, where the pulse decay rate has its largest value, while the ensemble decay rate is at its minimum.

At high optical depth, the ensemble becomes essentially opaque to an on-resonance excitation pulse. Consequently, atoms located at the far end of the chain remain initially unexcited. These atoms, therefore, do not contribute to the enhanced collective decay rate of the ensemble. In this case, it is not possible to approximate the ensemble by a timed Dicke state, as the excitation is not uniform across all atoms. As detailed in the next chapter, the initial ensemble decay rate and the pulse decay rate are equivalent only for ensembles prepared in the timed Dicke state, see Equation (4.33). Therefore, in the case of high optical depth and on-resonance excitation, fewer atoms are involved in the interaction, resulting in a lower ensemble decay rate. The significantly increased pulse decay rate on resonance can be attributed to the fact that, when the excitation pulse is switched

off, the initially unexcited atoms absorb the light emitted by the atoms at the beginning of the chain of atoms. Due to this absorption, the power of the emitted light quickly drops, resulting in a larger pulse decay rate. The combination of these two phenomena explain the noticeable discrepancy between the pulse and ensemble decay rates near resonance. This discrepancy was also observed in Figure 3.5(b). In that case, the detuning was moderate with $\Delta = 3.8\Gamma_o$ and the ensemble decay rate deviated from the pulse decay rate only for higher optical depth, consistent with what we just explained. For larger laser-atom detunings, the ensemble becomes less opaque, allowing a larger fraction of the atomic ensemble to be excited. As the ensemble state then approximates a timed Dicke state, the collective nature of the emission is enhanced, resulting in an increase in the ensemble decay rate, and it causes the pulse and ensemble decay rates to converge, see also Equation (4.33).

To confirm our understanding of these phenomena, Figure 3.6 also shows the decay rate of light scattered in the backward directions. In particular, near resonance, we measure very large pulse decay rates in forward direction, while the backward reflected light decays at the intrinsic rate Γ_0. This asymmetry results primarily from the fact that the photons detected in the backward direction are mainly emitted by atoms positioned at the beginning of the chain. To a first approximation, the probability of detecting a photon in the backward direction emitted by the nth atom in the chain decays exponentially with n as $\approx r_1 t_1^{2(n-1)}$, where r_1 and t_1 represent the single-atom reflection and transmission coefficients with constant $\beta_n = \beta$, as detailed in Section 2.2.1. As the excitation pulse is detuned, the coupling between light and atoms becomes weaker. As a result, photons reflected from atoms deeper in the ensemble now have a higher chance to leave in the backward direction, leading to an increase in the observed decay rate of the back-reflected pulse as more atoms from inside the ensemble take part in the collective interaction. Our theoretical model of the backward pulse decay rate, represented by a solid green line, qualitatively captures this behavior. The discrepancies between the predicted and observed decay rates can be attributed to inhomogeneous broadening of the atomic transition frequencies, possibly due to the proximity of the atoms to the nanofiber surface [85] or due to stray magnetic fields. In forward direction, these effects are negligible as the dynamics are mostly governed by the collective behavior of the atomic ensemble.

The strong quantitative and qualitative differences between the measured pulse decay rates in the forward and backward directions again highlight that, in contrast to the standard Dicke case, the atomic dynamics is highly position dependent.

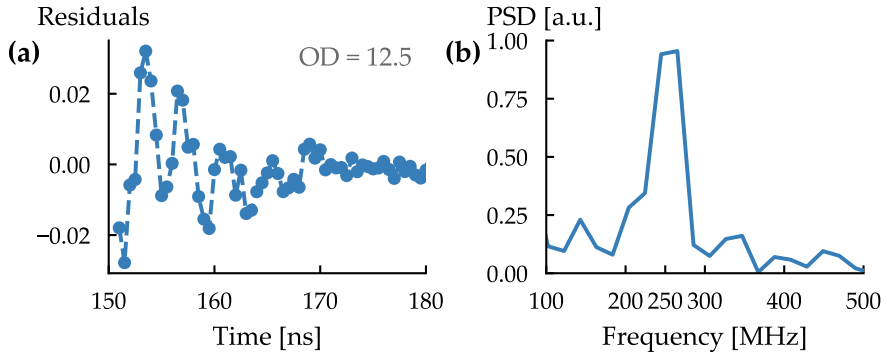

Figure 3.7: (a) The residuals between the exponential fit of the turn-off dynamics for OD = 12.5 show small amplitude oscillations attributed to quantum beats between the $F' = 4$ and $F' = 5$ states of the $6P_{3/2}$ excited state manifold. **(b)** The power spectral density distribution of the residuals in (a) shows a clear peak around 250 MHz, which agrees with the energy difference between the two states of 251 MHz.

3.3.3 Quantum Beats

Further analysis of the data shown in Figure 3.5(a) reveals the presence of small-amplitude oscillations superimposed on the pulse decay that are present for all measurements regardless of optical depth. These oscillations are ascribed to quantum beats resulting from the interference between photons emitted from the two excited states $F' = 4$ and $F' = 5$ of the $6P_{3/2}$ manifold. Although the frequency of the excitation pulse is tuned to excite the atoms from $6S_{1/2}$, $F = 4$ to the $6P_{3/2}$, $F' = 5$ state, some population also ends up in the $6P_{3/2}$, $F' = 4$ state. In order to better observe these oscillations, we plot in Figure 3.7(a) the residuals between the experimental data at OD = 12.5 and the exponential fit of the pulse decay alongside the power spectral density of the residuals in Figure 3.7(b). A pronounced peak in the power spectral density is observed around 250 MHz, which corresponds closely to the energy level difference between the $F' = 4$ and $F' = 5$ states of 251 MHz. In our analysis of superradiant decay, we averaged over these oscillations.

3.4 MULTIPLE PASSES THROUGH THE SAME ENSEMBLE

In our previous analysis, we demonstrated that collective effects build up successively with each atom that takes part in the interaction along the propagation direction of light. These collective phenomena

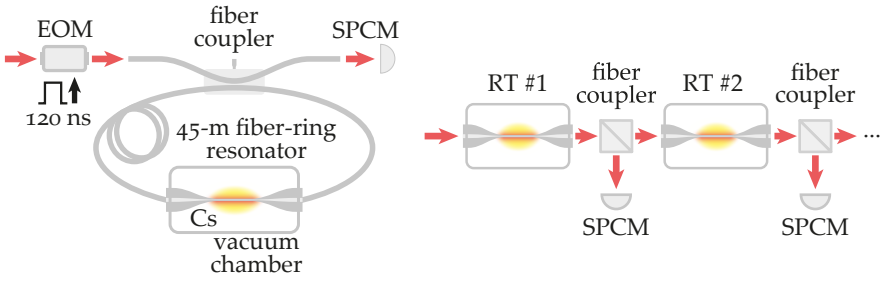

(a) Cavity setup

(b) Single pass through multiple ensembles

Figure 3.8: (a) The nanofiber is embedded within a 45-m-long fiber-ring resonator. A 120-ns-long light pulse is launched into the cavity via a fiber coupler and the transmission through the system is measured on a single photon counting module (SPCM). **(b)** For the short excitation pulses used in this experiment, the system can be viewed as a single pass through multiple ensembles separated by 45 meters, allowing us to observe the gradual build up of collective effects along the propagation direction.

emerge regardless of the distance between the atoms and even when the inter-atomic distance is much larger than the spatial extent of the excitation pulse or the distance light travels within an atomic lifetime. Theoretical studies have shown interest in such a regime [83, 86], but experimental investigations have been elusive so far. Our nanofiber-based atom-light interface allows us to enter this regime as it is embedded within a very long fiber-ring resonator.

Figure 3.8(a) depicts the experimental setup which includes the fiber-ring resonator. A single excitation pulse enters the cavity at the coupler and propagates along the fiber-ring. After being transmitted past the atomic ensemble, a part of the light is coupled out at the fiber coupler and is detected on an SPCM. The remaining light continues to propagate in the cavity, interacting with the ensemble each successive roundtrip.

The fiber-ring cavity is approximately 45 m long and thus has a roundtrip time of $t_{\mathrm{rt}} = 219.7\,\mathrm{ns}$. Since the pulses that we launch are shorter than the roundtrip time ($t_{\mathrm{pulse}} = 120\,\mathrm{ns}$), there is no build up of an intracavity field. The time between a pulse returning to the atoms in the cavity is also longer than the decay time, τ_{at}, of the atoms ($t_{\mathrm{rt}} - t_{\mathrm{pulse}} = 100\,\mathrm{ns} \gg \tau_{\mathrm{at}} = 30.4\,\mathrm{ns}$ for cesium [87]). The atoms therefore have enough time to revert to their ground state before the arrival of the next pulse. Furthermore, the roundtrip time of the resonator is also smaller than the average transit time of the atoms through the evanescent field of the nanofiber of $\approx 1\,\mu\mathrm{s}$ [59]. As a result, the interaction of each pulse with the ensemble is independent of the previous interaction as the ensemble has no memory of it. Therefore,

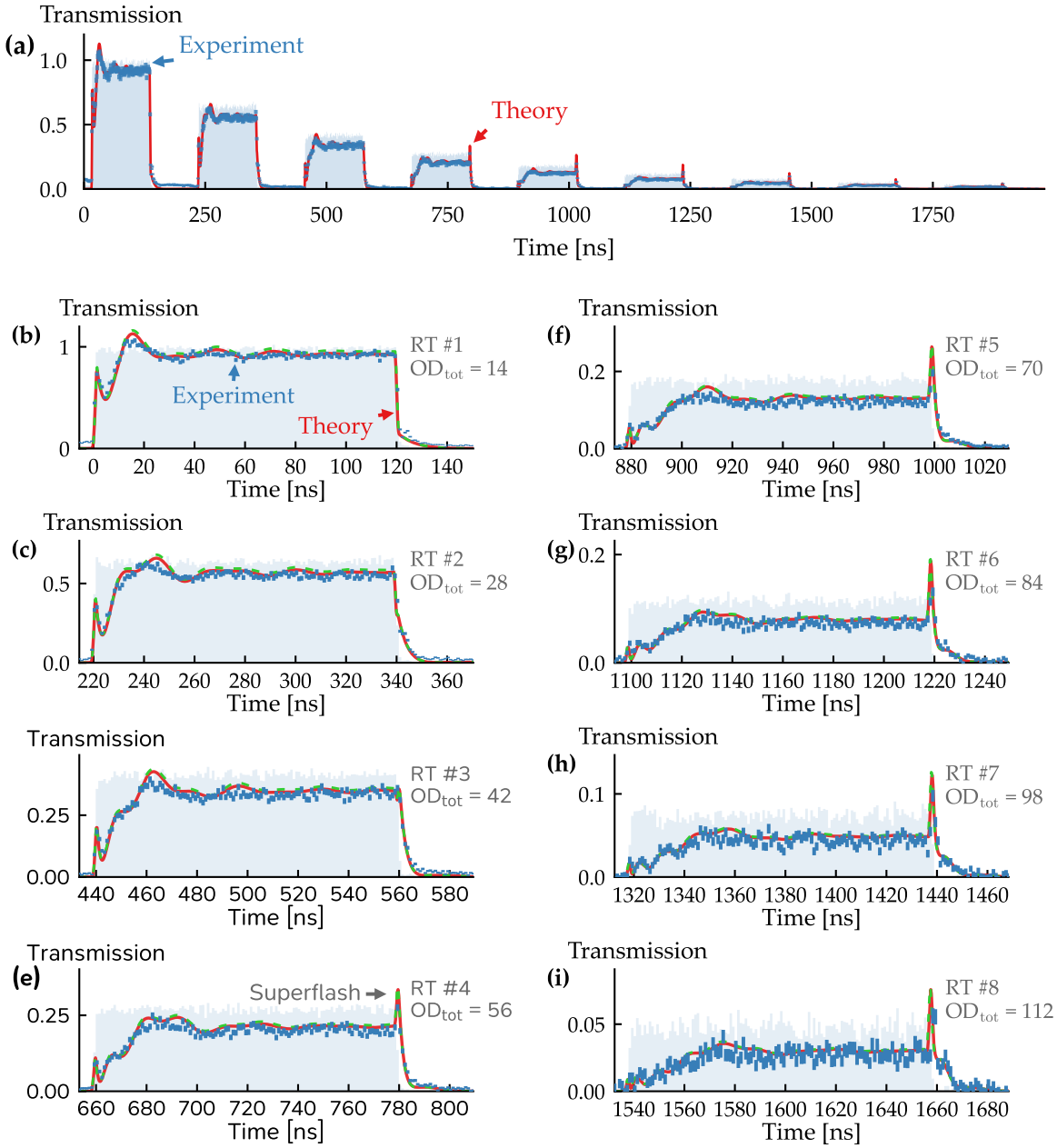

Figure 3.9: (a) The time trace of transmitted light through the system after a single light pulse is launched into the cavity for an atomic ensemble with $OD_{sp} = 14$ and a laser–atom detuning of $\Delta = 8.7\Gamma_0 = 2\pi \times 45\,\text{MHz}$. The data was obtained by averaging over 9×10^6 excitation pulses. **(b) - (i)** show the outcoupled pulses after the mth roundtrip. The solid red line corresponds to the comprehensive theoretical description of a pulse propagating in a cavity (see Section 2.2.2), while the green dashed lines correspond to the calculated single-pass dynamics (see Section 2.2.1), for an ensemble with total optical depth of $OD_{tot} = m \times OD_{sp}$.

the time dynamics of the ensemble observed in the light field after the mth roundtrip through the cavity is approximately the same as for a

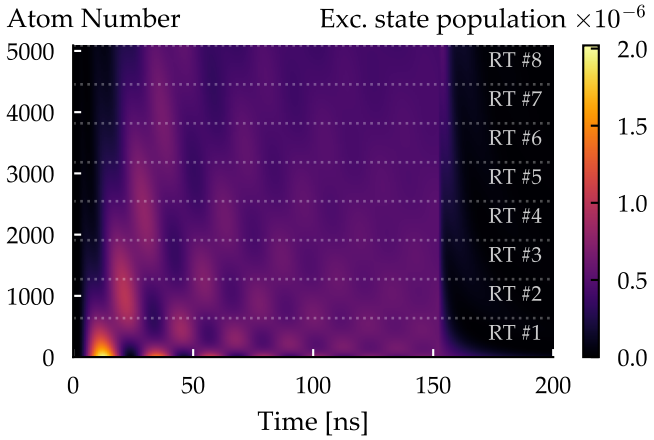

Figure 3.10: The time evolution of the calculated excited state populations for individual atoms along the propagation direction of light are plotted up to the eighth roundtrip through our ensemble which corresponds to a total optical depth of $OD_{tot} = 112$. Atoms are added to the atom number again as light completes another roundtrip. The laser–atom detuning here is $\Delta = 8.7\Gamma_0 = 2\pi \times 45\,\mathrm{MHz}$.

single pass through an ensemble with a larger total optical depth of $OD_{tot} = m \times OD_{sp}$, where OD_{sp} is the single-pass optical depth.

As a consequence, the system can be regarded as a pulse making a single pass through multiple ensembles located 45 m away from each other, as depicted in Figure 3.8(b). As some light is outcoupled in between the ensembles, we can thus directly observe the progressive growth of collective effects in a position-resolved measurement. Furthermore, much higher optical depths of above OD = 100 can be reached that would otherwise not be possible in our setup.

Figure 3.9(a) shows the time trace of the transmitted light after launching a 120-ns-long excitation pulse in the cavity. The atomic ensemble has a single-pass optical depth of $OD_{sp} = 14$ and the laser-atom detuning is $\Delta = 8.7\Gamma_0 = 2\pi \times 45\,\mathrm{MHz}$. The blue shaded area represents the measured transmission in the absence of atoms, serving as a reference. The blue squares depict the experimental data in the presence of atoms, where the height of each square indicates the statistical error of the counts. The solid red line illustrates the theoretical prediction made by our model, as detailed in section 2.2.2, without the use of free parameters.

The individually outcoupled pulses are shown in Figures 3.9(b) - 3.9(i) for the first eight cavity roundtrips corresponding to an increasing total optical depth from $OD_{tot} = 14 - 112$. With each roundtrip, the switch-on dynamics of the pulse becomes more complex and the collective Rabi oscillations diverge more from the simple sinusoidal oscillations of single atoms. In particular, for high optical depths

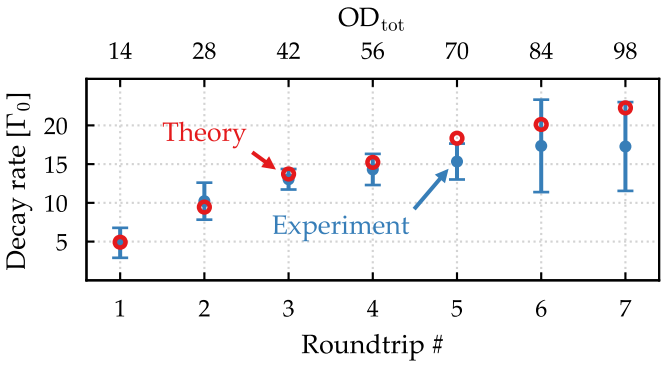

Figure 3.11: The measured (blue dots) and calculated (red circles) decay rates after the switch-off of the excitation pulse in Figure 3.9 increase linearly with each roundtrip due to the increase in total optical depth. We observe an increased decay rate of more than 20 times the single atom decay rate.

starting from OD = 56, as shown in Figures 3.9(e) - 3.9(i), additional oscillation frequencies start to emerge. These oscillations occur at frequencies much higher than the expected Rabi frequency Δ and show considerable dependence on optical depth.

To achieve a microscopic understanding of these phenomena, Figure 3.10 illustrates the excited state populations of individual atoms over time for the parameters of this experiment calculated using our cascaded interaction model, extending up to the eighth roundtrip. Atoms early in the chain are located at the bottom of the color map, and oscillate at a frequency close to the Rabi frequency. However, atoms positioned further towards the end of the chain invert their oscillation phase even before the first atoms complete a single Rabi cycle. For instance, at $t = 25\,\mathrm{ns}$, the 700th to the 2000th atom in the color map are predominantly in the excited state, while the preceding atoms are in the ground state. This phase inversion leads to the additional oscillations in the output field, contributing to the observed complexity of the dynamics.

The switch-off dynamics is characterized by superradiant decay, consistent with the measurements presented in Figure 3.5(a). Figure 3.11 summarizes the fitted pulse decay rates for each individual roundtrip. We fit only the inital decay rate where the decay can still be characterized by an exponential. The fit's accuracy decreases for later roundtrips due to increased experimental uncertainties, but the theoretical values are still within the error bar. The decay rate of the eighth roundtrip has been omitted due to insufficient data points for a reliable fit.

The shape of the switch-off dynamics in Figure 3.9 changes above an optical depth of $\mathrm{OD_{tot}} = 56$. Above this value, the collectively emitted light field develops a distinct shoulder after the initial superradiant de-

cay. This shoulder can be explained by the ensemble passing through a subradiant state, a phenomenon which will be discussed in detail in the following chapter.

Moreover, starting from Figure 3.9(e), the measurements reveal the emergence of a coherent superflash of light with increasing optical depth, a phenomenon discussed in [88]. In the steady state, which is approximately reached before the pulse switches off, the transmitted intensity must be lower than the incident intensity. However, this does not mean that the scattered field has to be smaller than the incident field. Since they are complex quantities, the scattered field can be out of phase with the incident field. In principle, the scattered field can have a maximum amplitude of up to twice that of the input field. When the input field is abruptly switched off, the output field consists solely of the scattered field, producing a short superflash with an intensity up to four times that of the incident light. The maximum intensity depends on a combination of the detuning of the excitation laser field and the optical depth of the ensemble. In our measurements, the superflash reached a maximum intensity of approximately one and a half times the incident intensity.

In Figures 3.9(b) - 3.9(i), we also compare two sets of theoretical predictions that describe the temporal dynamics. The solid red lines correspond to the comprehensive description of our system with the cascaded interaction model that includes the resonator, as described in Section 2.2.2. The green dashed lines, on the other hand, are the predictions for a single pass through an ensemble characterized by a total optical depth of $\mathrm{OD}_{\mathrm{tot}} = m \times \mathrm{OD}_{\mathrm{sp}}$ with the unidirectional propagation model described in Section 2.2.1. The two predictions agree very well for our measurements, confirming our claim that the emergence of collective effects is independent of the interatomic distance and that the waveguide mediates the interactions between atoms over an infinite range.

3.5 SUMMARY AND CONCLUSIONS

In this chapter, we explored the collective radiative dynamics of a one-dimensional ensemble of atoms excited by boxcar-shaped pulses in the vicinity of a nanofiber. Our focus in the analysis was on two key phenomena: collective Rabi oscillations and superradiant decay of the ensemble. Additionally, we examined the effects of the pulse interacting multiple times with the ensemble within a 45-m-long fiber-ring resonator.

First, we discussed the collective Rabi oscillations observed at the turn-on of the excitation pulse. By fitting the dynamics with the cascaded interaction model, we analyzed the excited state probabilities on an atom-by-atom basis. Each atom oscillated with its Rabi frequency, but atoms located further back in the one-dimensional ensemble were found to oscillate out of phase compared to atoms in the beginning, as they were excited by the incident field plus the emission from preceding atoms. As the observed complex dynamics emerges from the cumulative sum of the individual atomic emissions, the collective effects build up gradually along the chain and with the number of involved emitters.

Next, we investigated the superradiant decay of the ensemble after the excitation pulse switched off. We found that the observed pulse decay rate increases approximately linearly with optical depth, whereas the calculated collective ensemble decay rate deviates for higher optical depths from the measured pulse decay rate, exhibiting a slower growth rate and a saturation behavior. Furthermore, we observed that the discrepancy between the pulse decay rate and the ensemble decay rate was greatest on resonance. Conversely, for increased detuning their values approached each other. For high optical depths and on-resonance excitation, the ensemble is not being excited into a timed Dicke state where all atoms share the same excitation, as only a smaller number of atoms is excited at the beginning of the one-dimensional atomic ensemble while the following atoms remain in the ground state. The discrepancy between the pulse and ensemble decay rates arises because they only coincide when the ensemble is in a timed Dicke state at $t = 0$.

By integrating our nanofiber into a 45-m-long fiber-ring resonator, we demonstrated that the dynamics of an ensemble with a single-pass optical depth, $\mathrm{OD}_{\mathrm{sp}}$, after the mth roundtrip are equivalent to those of an ensemble with a total optical depth $\mathrm{OD}_{\mathrm{tot}} = m \times \mathrm{OD}_{\mathrm{sp}}$. This experiment allowed us to observe the gradual build up of collective effects with the number of involved atoms. This showed that the distance between emitters is not a determining factor for collective effects as long as the interaction is mediated by the same optical mode.

4 COHERENT COUPLING BETWEEN SUPER- AND SUBRADIANT STATES

The results presented in this chapter have been published in [89]:
Riccardo Pennetta, Daniel Lechner, Martin Blaha, Arno Rauschenbeutel, Philipp Schneeweiss, and Jürgen Volz.
Observation of Coherent Coupling between Super- and Subradiant States of an Ensemble of Cold Atoms Collectively Coupled to a Single Propagating Optical Mode.
Physical Review Letters, 128(20):203601, 2022.

In the previous chapter, we examined the superradiant decay of an atomic ensemble following the switch-off of a light pulse. We observed a distinct shoulder in the emission pattern after an initial superradiant decay. In this chapter, we explore these emission dynamics in more detail and explain their origin in the context of the ensemble passing through subradiant states.

Dicke [73] described the collective emission of N quantum emitters that share a number of excitations and are spaced closer than the wavelength of the emitted light (see Equation (3.26) and the situation in Figure 3.1(a)). He decomposed the Hilbert space of such an ensemble into a superradiant state, which features an N times enhanced decay rate to the ground state, and into $N-1$ orthogonal subradiant states for which decay into the ground state is suppressed. In this framework, these states do not couple to each other so that an ensemble initially prepared in a superradiant state will remain in that state and simply decay with an enhanced, superradiant rate.

In many experimental settings, however, the spacing between emitters is often larger than the wavelength of light, a situation which requires a description using timed Dicke states (see Equation (3.27) and the situation in Figure 3.1(b)). Again, similarly to the Dicke state, the Hilbert space can be decomposed into a superradiant and many subradiant states. As such systems are so ubiquitous, considerable effort has been made in describing their temporal dynamics [42, 83, 90–93]. Unlike in the traditional Dicke model, the superradiant and subradiant states are coupled to each other for the emission of extended ensembles.

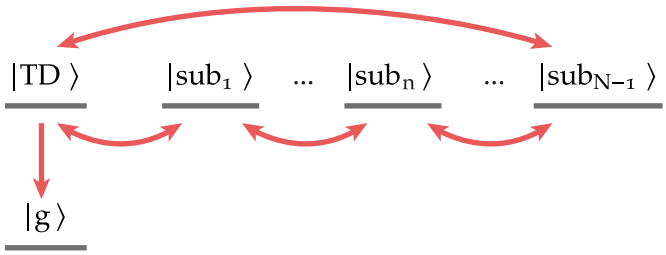

Figure 4.1: In the single excitation limit, the collective quantum state of an extended ensemble of N atoms is composed of a superradiant timed Dicke state, $|\mathrm{TD}\rangle$, and $N-1$ subradiant states, $|\mathrm{sub}_n\rangle$. These states are orthogonal to each other and span up the Hilbert space of the ensemble. All states are coupled to each other, but only the timed Dicke state decays to the collective ground state, $|\mathrm{g}\rangle$. As the ensemble decays, it transitions from the timed Dicke state sequentially through each of the subradiant states.

This chapter examines these dynamics using a simple experimental system consisting of a one-dimensional ensemble of N atoms that are coupled via a single optical mode of a waveguide. We introduce a theoretical framework that enables us to derive analytical solutions for this experimental scenario, allowing for a detailed study of the microscopic temporal dynamics of the ensemble. The model demonstrates that all basis states of the Hilbert space are coherently coupled, and that an ensemble initially prepared in the timed Dicke states passes, one after the other, through all its $N-1$ subradiant states, as sketched in Figure 4.1. When an ensemble is in a subradiant state, the emission into the guided mode is suppressed due to destructive interference of the emission from all atoms. These phenomena occur regardless of the number of atoms or their coupling strength to the optical mode. This behavior is predicted to manifest even with as few as two emitters and arbitrarily weak coupling [94], unlike in the case of three-dimensional atom clouds [83].

We validate the theoretical predictions through experiments with our system of cesium atoms coupled to a nanofiber's guided mode. We investigate the temporal response of the emitted light from the ensemble following the switch-off of boxcar-shaped excitation pulses and then analyze the phase of the emitted light using a homodyne measurement. We also study how the temporal dynamics change when varying the optical depth of the ensemble and when the excitation light is detuned. Finally, we conclude with further theoretical insight into the prepared state in the experiment and provide approximate solutions to the problem. Additionally, we show that the basis states are orthogonal and discuss the influence of nonuniform coupling strengths on the dynamics.

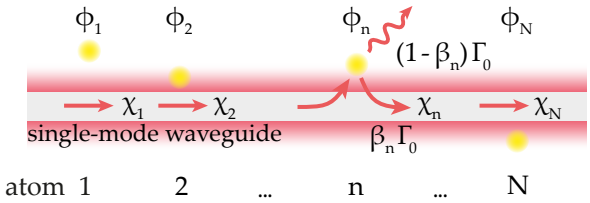

Figure 4.2: The situation under consideration of N atoms that are coupled to a single-mode waveguide via its evanescent field. The excited state amplitudes of the atoms are denoted as ϕ_n and the light field amplitude in the waveguide after the nth atom as χ_n. Atom number n emits light into the waveguide with a rate $\beta_n\Gamma_o$ and into free space with a rate $(1-\beta_n)\Gamma_o$. To prepare this ensemble into the timed Dicke state, a short δ-like pulse is launched into the system.

4.1 THEORETICAL DESCRIPTION FOR THE TIMED DICKE STATE

This section presents and discusses a theoretical description of our system, providing analytical solutions derived from the cascaded interaction model for an ensemble excited into the timed Dicke state. Afterwards, we show an approximation that is valid for large ensembles and small light–matter coupling strengths β.

4.1.1 Analytical Solutions

Figure 4.2 depicts the situation under consideration, where N atoms are coupled to a single-mode waveguide via its evanescent field. $\phi_n(t)$ is the excited state amplitude of the individual atoms and $\chi_n(t)$ is the light field amplitude after the nth atom in the waveguide. Excited atoms can decay into the waveguide or into free space with the rates $\beta_n\Gamma_o$ or $(1-\beta_n)\Gamma_o$, respectively, where Γ_o is the spontaneous emission rate of the atom in free space.

To prepare such an ensemble in the timed Dicke state, a very short δ-like pulse with field amplitude $u_{\text{in}}(t) \propto \delta(t)$ can be launched into the waveguide, ensuring that each atom has an equal probability of being excited. When one excitation is in the system, all atoms share that excitation, i.e., the excited state amplitude of each atom is $\phi_n(t=0) = 1/\sqrt{N}$. As we assume unidirectional propagation of light, the light field after an atom, $\chi_n(t)$, is proportional to the sum of the excitation amplitudes of the preceding n atoms.

Under these conditions and assuming an average β for all atoms, Equation (2.6) can be solved analytically to obtain

$$\phi_n(t) = \frac{1}{\sqrt{n}} e^{-\frac{\Gamma_o}{2}t} L_{n-1}^{(0)}(\beta\Gamma_o t)\,, \tag{4.31}$$

$$\chi_n(t) = \frac{\sqrt{\beta\Gamma_o}}{i\sqrt{v_g}} \sum_{m=1}^{n} \phi_m(t) = \frac{\sqrt{\beta\Gamma_o}}{i\sqrt{v_g n}} e^{-\frac{\Gamma_o}{2}t} L_{n-1}^{(1)}(\beta\Gamma_o t)\,, \tag{4.32}$$

where $L_m^{(\alpha)}$ are generalized Laguerre polynomials. The derived solutions reveal that, apart from the factor $e^{-\frac{\Gamma_o}{2}t}$, the dynamics is only influenced by the product $\beta\Gamma_o t$ and the atom number n. Therefore, the dynamic behavior remains fundamentally the same for all values of the emitter-mode coupling strength β, provided that the observation time is adjusted appropriately. For $\beta = 1$, these results are consistent with those obtained from a master equation approach [90].

Using these analytical equations, it can be shown that the pulse and ensemble decay rates are equal for an ensemble in the timed Dicke state at $t = 0$. By using the property of Laguerre polynomials given by $\frac{d}{dt}L_n^{(0)}(t) = \frac{d}{dt}L_{n-1}^{(0)}(t) - L_{n-1}^{(0)}(t)$, we can solve Equations (3.28) and (3.29) for $t = 0$ and obtain

$$\Gamma_{\text{ens}}(t = 0) = \Gamma_{\text{pulse}}(t = 0) = N\beta\Gamma_o + (1 - \beta)\Gamma_o\,. \tag{4.33}$$

This equality holds only for an ensemble prepared in a timed Dicke state at $t = 0$. Thus, deducing Γ_{ens} from Γ_{pulse} at $t \neq 0$ or for differently prepared states will yield inaccurate results.

To understand the time evolution of the timed Dicke state, it is easier to start from a simple system consisting of only four atoms. As the time evolution of the excited state amplitudes, $\phi_n(t)$, and the field amplitudes, $\chi_n(t)$, completely determine the state of the system, it is possible to compute experimentally observable quantities such as the total waveguide-coupled optical power $|\chi_N(t)|^2$ and the ensemble decay rate $\Gamma_{\text{ens}}(t)$. These two quantities are plotted in Figure 4.3(a) and 4.3(b) for a system with $N = 4$ atoms and an average atom-waveguide coupling strength $\beta = 0.4$. The blue curve represents the case for four atoms and the gray curve for a single atom.

Initially, at $t = 0$, the ensemble is in the timed Dicke state and decays into the guided mode of the waveguide with a superradiant decay rate that is N times enhanced compared to the decay of a single atom, i.e., $\Gamma_{\text{ens,wg}}(0) = N\beta\,\Gamma_o$. At this point, the total ensemble decay rate has its maximum value of $\Gamma_{\text{ens}}(t = 0) = \Gamma_{\text{ens,wg}}(0) + \Gamma_{\text{fs}} = N\beta\Gamma_o + (1 - \beta)\Gamma_o$, which is depicted as the upper gray bar in Figure 4.3(b).

As the system evolves, the waveguide-coupled power reduces three times to zero for the situation of four atoms depicted in Figure 4.3(a).

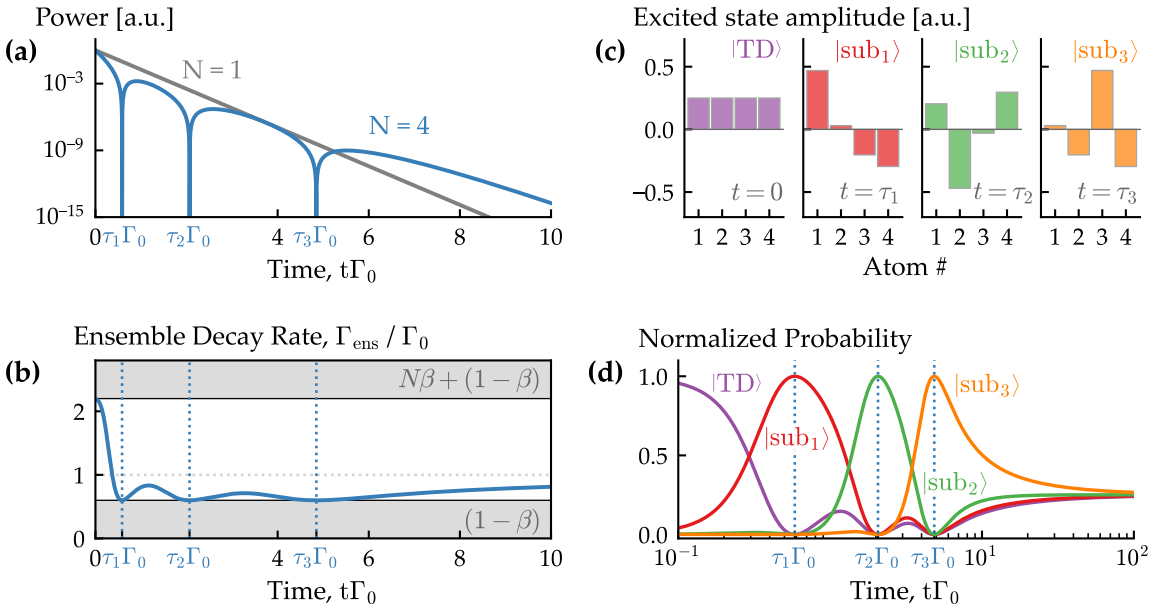

Figure 4.3: The evolution of a system of $N = 4$ atoms and $\beta = 0.4$ prepared in a timed Dicke state based on the exact analytical solutions. **(a)** The calculated power emitted into the waveguide $|\chi_N(t)|^2$ in blue shows a sharp drop in emission every time the ensemble enters a subradiant state at normalized time $\tau_n\Gamma_o$. The case of a single atom is shown for comparison in gray. **(b)** The ensemble decay rate $\Gamma_{\text{ens}}(t)$ is maximum in the superradiant timed Dicke state at $t = 0$ where the decay into the waveguide is $N\beta$-times enhanced. The decay rate is minimal when the system is in a subradiant state, depicted by vertical dotted lines, where the system emits solely into free space with a rate $(1-\beta)$. **(c)** In the timed Dicke state, the normalized excited state amplitudes add up and the emission into the guided mode is enhanced, while in the subradiant states, subensembles emit out of phase causing complete destructive interference into the waveguide. **(d)** The projection of the quantum state of the atoms that still contain a residual excitation on the timed Dicke and the subradiant states shows how all basis states are coupled and that the ensemble passes through all of them until it reaches a superposition of all states at long times, where the ensemble decay rate is then equal to Γ_o.

In general, the emission dynamics goes through $N-1$ zeros for $t > 0$. The times τ_m, with $m = 1, \ldots, N-1$, when the system reaches a zero are the roots of the generalized Laguerre polynomial $L^{(1)}_{N-1}(\beta\Gamma_o t)$, see Equation (4.32) for $n = N$. At these times, the system is subradiant with respect to the waveguide mode and the complete set of subradiant states is given by

$$|\text{sub}_m\rangle = \sum_{n=1}^{N} e^{ikz_n}\phi_n(\tau_m)\hat{\sigma}_n^+|0\rangle \ . \tag{4.34}$$

For these states, the waveguide-coupled light is zero, i.e., the decay rate into the waveguide $\Gamma_{\text{ens,wg}}(\tau_m) = 0$. On the other hand, the light emitted into free space at these times remains unchanged and when the system is in a subradiant state the total ensemble decay rate

reaches its bottom limit of $\Gamma_{\text{ens}}(\tau_m) = \Gamma_{\text{fs}} = (1-\beta)\Gamma_o$ as depicted by a gray bar at the bottom of Figure 4.3(b). We note that when setting $z = 0$ in Equation (4.34), the resulting states are also subradiant in the standard Dicke model.

To understand the dynamics better, Figure 4.3(c) presents the excited state amplitudes, ϕ_n, of the individual atoms for the superradiant timed Dicke state, $|\text{TD}\rangle$, and the subradiant states, $|\text{sub}_m\rangle$. The excited state amplitudes were normalized so that in each case the absolute value of the excited state amplitudes add up to one. Initially, in the timed Dicke state, all atoms share the same excitation. The excited state amplitudes of individual atoms then evolve over time. When the first subradiant state, $|\text{sub}_1\rangle$, is reached, the first two and the last two atoms of the ensemble emit light with opposite phase causing the waveguide-coupled light to be destructively interfered away, which causes the first zero in Figure 4.3(a). After the first subradiant state, each successive subradiant state has a similar structure in which subensembles of consecutive atoms radiate in phase opposition, but the number of these subensembles increases by one for each subradiant state. For instance, the second subradiant state has three distinct subensembles radiating in antiphase, and the third one has four. The phase differences between the excited states amplitudes are relative to the first excited atom in the ensemble.

Figure 4.3(d) presents an analysis that provides further insight into the dynamics of the system. It shows the decomposition of the quantum state of the atoms with the residual excitation projected onto the basis of the timed Dicke and superradiant states, and how they evolve. All states are coupled to each other, and the system transitions from the inital timed Dicke state through each of the subradiant states. Eventually, it reaches a superposition of the timed Dicke and the subradiant states with an equal probability of $1/N$ for $t \gg \tau_{N-1}$. In Figure 4.3(b) it can be observed that, for such long times, the ensemble decay rate, Γ_{ens}, asymptotically converges to the decay rate of a single atom, Γ_o. The progression through all states remains qualitatively unchanged for any atom number N and coupling strength β.

4.1.2 Approximate Solutions for $N \gg 1$ and $\beta \ll 1$

In our experiments, there is often a large number of atoms involved and the coupling between the waveguide and the atoms is usually small, i.e., $N \gg 1$ and $\beta \ll 1$. For large N, Laguerre polynomials can be approximated with the following relation

$$L_n^{(\alpha)}(x) \approx \frac{n^\alpha}{\sqrt{x}^\alpha} e^{x/2} J_\alpha(2\sqrt{nx}), \tag{4.35}$$

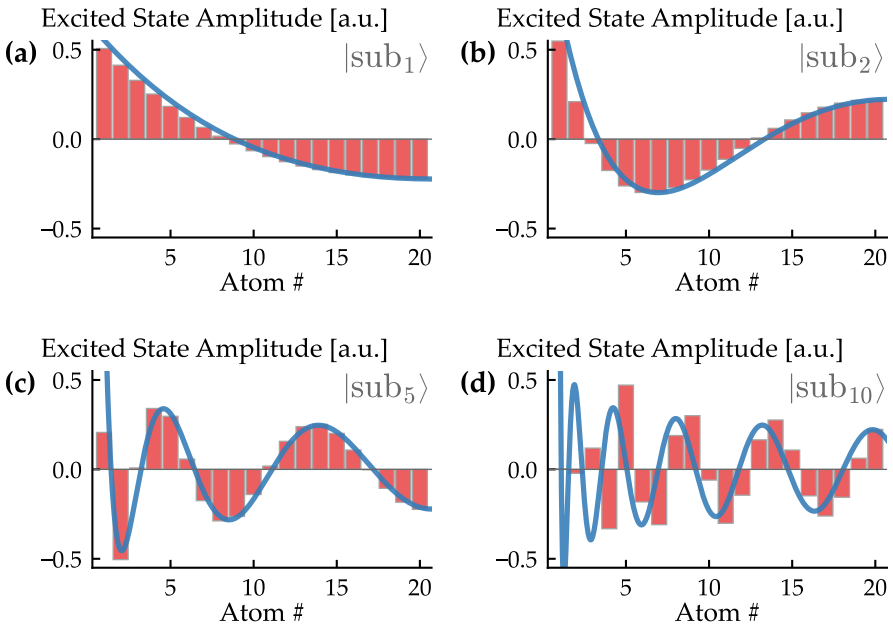

Figure 4.4: The comparison of the exact solutions of the excited state amplitudes (red bars) and the approximation with Bessel functions (blue solid lines) for $N = 20$ atoms for the subradiant states $|\mathrm{sub_m}\rangle$ with **(a)** $m = 1$, **(b)** $m = 2$, **(c)** $m = 5$ and **(d)** $m = 10$ shows that the approximation is only appropriate when the number of the subradiant state $m \ll N$.

where $J_\alpha(x)$ are the Bessel functions of the first kind. It thus becomes possible to simplify (4.31) and (4.32) to yield

$$\phi_n(t) \simeq \frac{1}{\sqrt{N}} e^{-\frac{\Gamma_0}{2}t} J_0\left(\sqrt{\Gamma_0 \,\mathrm{OD}\, \frac{n-1}{N}}\, t\right) \tag{4.36}$$

$$\chi_N(t) \simeq \frac{\sqrt{\mathrm{OD}}}{i\sqrt{4 v_g \beta t}} e^{-\frac{\Gamma_0}{2}t} J_1(\sqrt{\Gamma_0 \,\mathrm{OD}\, t})\,. \tag{4.37}$$

These relations are relevant for experiments with a large number of emitters and are consistent with findings from studies on continuous resonant media [90, 95].

The argument of the Bessel functions depends only on $\mathrm{OD} \simeq 4\beta N$, indicating that the dynamics of the system is well described even when the coupling strength of individual emitters varies, provided that $\beta_n \ll 1$. This claim has been verified by numerical analysis. The dependence of the dynamics only on OD is consistent with the findings in Figure 4.8(i) where the time of the subradiant states does not depend on the β-factor but rather on the overall OD.

The Laguerre polynomials that describe the exact solution have $N - 1$ roots, which leads to zeros in the emitted field, whereas Bessel functions exhibit infinite zeros. Consequently, the approximation

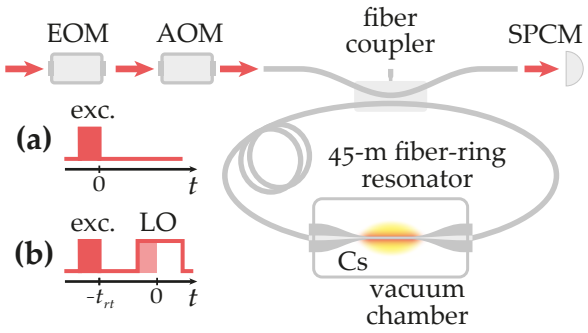

Figure 4.5: Overview of the experimental setup in our studies. **(a)** We use a 100-ns-long excitation pulse generated by an electro-optic modulator (EOM) and an acousto-optic modulator (AOM) and subsequently measure the emission of the atomic ensemble on a single photon counting module (SPCM). **(b)** For phase-resolved or homodyne measurements, we launch a sequence of an excitation pulse and a 240-ns-long local oscillator pulse. The excitation pulse completes one roundtrip in the fiber-ring resonator in the time t_{rt} before exiting the resonator to interfere with the local oscillator pulse on the SPCM. The shaded area is used to illustrate when the excitation pulse leaves the resonator and starts to interfere with the local oscillator. The zeros in the timeline mark the zero time points in our measurements.

using Bessel functions has limitations, especially for timescales when the number of zeros becomes comparable to the number of atoms. To illustrate these limits, Figure 4.4 compares the predictions of the exact and the approximated model for the first, second, fifth and tenth subradiant states for the situation of $N = 20$ atoms. The bars show the excited state amplitudes for the exact solution while the solid line represents the approximate solution. Despite using only twenty atoms in this simulation, the Bessel function closely approximates the exact solution for lower order subradiant states, $|\mathrm{sub}_m\rangle$, as long as $m \ll N$. However, for higher order subradiant states, as shown in Figure 4.4(d), the discrepancies between the exact and approximate solutions become more pronounced. For even higher subradiant states, the Bessel functions fail to match the exact solution. This divergence is expected because, as previously mentioned, the Bessel function approximation allows for an infinite number of subradiant states, while the exact solution is limited to $N - 1$ subradiant states.

4.2 EXPERIMENTAL OBSERVATION OF SUBRADIANT STATES

This section presents experimental measurements of the temporal evolution of the emission from an atomic ensemble following excitation

with a light pulse. We first observe the temporal evolution of the emission, and then analyze the phase of the emitted light by interfering it with a local oscillator. Additionally, we investigate how the dynamics change when varying the optical depth of the ensemble and detuning of the light field.

The general setup that is used to analyze the temporal dynamics of the system is shown in Figure 4.5. The ensemble state is prepared by launching a 100-ns-long excitation pulse. We then detect the emitted light after the falling edge of the pulse on a SPCM. The pulse energy is set to be less than one photon per atomic lifetime, i.e., on the order of 1 pW, ensuring that, on average, less than one excitation is stored in the ensemble. To minimize the background noise after the pulse switches off, we use a slow-switching acousto-optic modulator (AOM) in conjunction with a fast-switching electro-optic modulator (EOM), since the EOM has an extinction ratio of only 20 dB. As soon as the AOM switches off our detection is limited only by the dark counts of the SPCM. To measure the temporal dynamics directly, we use the pulse sequence shown in Figure 4.5(a), while for phase measurements, we use the sequence in Figure 4.5(b).

4.2.1 Temporal Evolution Through Subradiant States

Figure 4.6(a) presents the time-resolved measurements of the emitted optical power after the excitation pulse turns off. In this measurement, we use the pulse sequence depicted in Figure 4.5(a). The optical depth of the ensemble was determined to be $\mathrm{OD} = 31 \pm 1$ from a fit of our unidirectional propagation model (see Section 2.2.1) to the experimental data with the OD as the only fit parameter. The error margin of the OD corresponds to the 99% confidence interval of the fit.

Immediately following the switch-off of the excitation pulse at $t = 0$, the ensemble undergoes superradiant decay. Subsequently, the ensemble evolves and goes through two minima in emitted power, occurring at times $t = 6.1\,\mathrm{ns}$ and $t = 30.6\,\mathrm{ns}$. As shown in Figures 4.7(b) and 4.7(c), the ensemble is in a subradiant state with respect to the nanofiber mode at these times. Just as described previously in the simple case of four atoms, when the ensemble is in the first subradiant state, the first part of the ensemble radiates with opposite phase compared to the second part of the ensemble. In the second subradiant state, three subensembles emit light such that their emission into the guided mode destructively interferes. Related dynamics have been observed in other systems, such as continuous, resonant media [95–97].

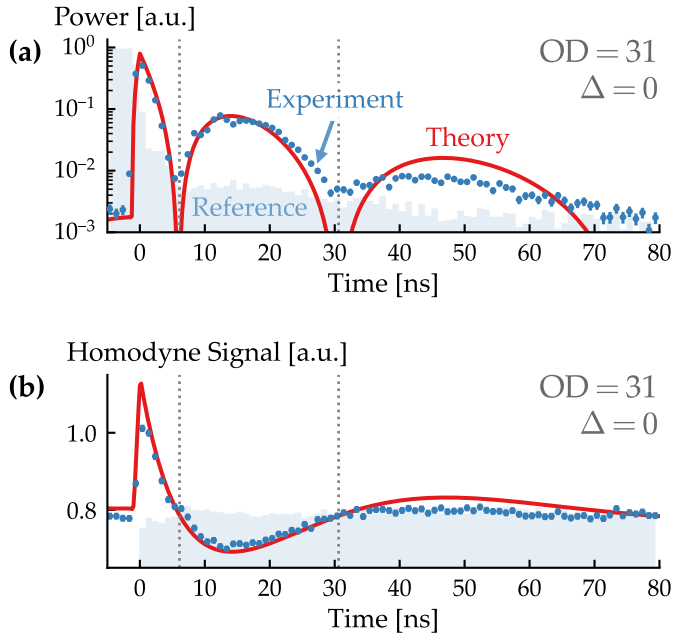

Figure 4.6: (a) Time-resolved measurement of the emitted power into the waveguide from an ensemble with OD = 31 after the switch-off of a resonant excitation pulse. Initially, the ensemble exhibits superradiant decay, followed by temporary drops in emitted power as it transitions through the first two subradiant states. The vertical dotted lines mark the calculated times at which these subradiant states occur. The theoretical predictions are displayed as a solid red line and the experimental data as dots with error bars representing the standard deviation of the counted photons. The reference pulse measured in the absence of atoms is shown as a shaded area. **(b)** The homodyne measurement for the same parameters shows that the phase of the emitted light changes as the ensemble passes through a subradiant state.

4.2.2 Phase of Emitted Light

Our theoretical predictions suggest that each time the ensemble passes through a subradiant state, the projection of the ensemble state onto the timed Dicke state, and hence the amplitude of the emitted light field reverse their signs. To study these phase changes experimentally, we repeated the measurement shown in Figure 4.6(a) but interfered the emitted light with a local oscillator in a homodyne measurement. This was realized using our long fiber-ring cavity and the pulse sequence depicted in Figure 4.5(b). First, the same excitation pulse as before is launched into the resonator. Then another 240-ns-long local oscillator pulse is launched which is timed to coincide with the excitation pulse as it leaves the resonator after a full roundtrip through the cavity, which occurs after $t_{\mathrm{trt}} = 219.7\,\mathrm{ns}$. The excitation pulse, the light emitted by the atoms, and the local oscillator then travel towards the SPCM, where we measure their interference.

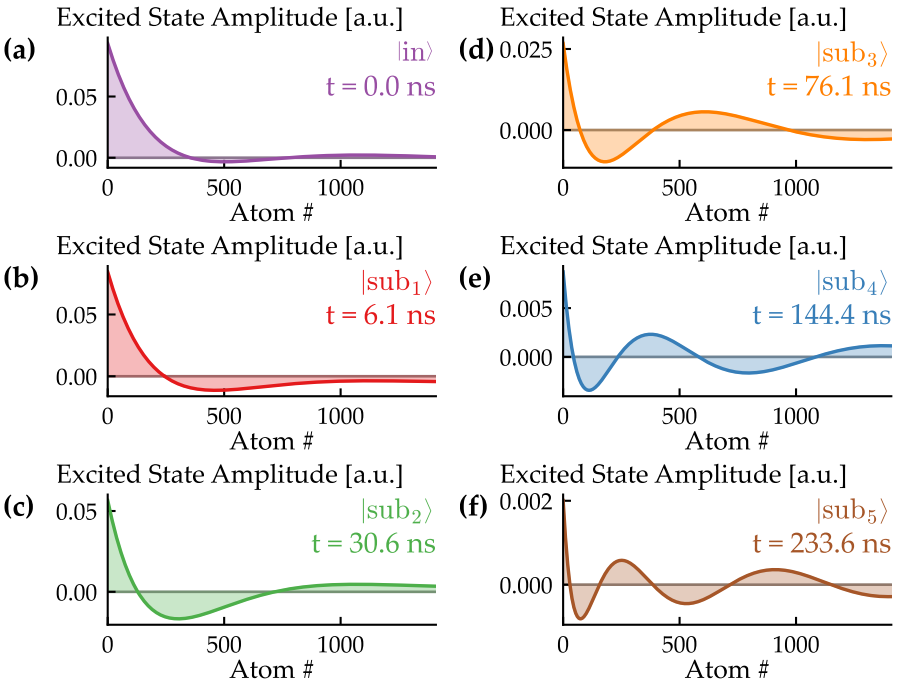

Figure 4.7: The excited state amplitudes, $\phi_n(t)$, of the individual atoms for **(a)** the ensemble state, $|\text{in}\rangle$, initially prepared in the experiment for OD = 31 and $\Delta = 0$ after turning off a 100-ns-long excitation pulse and **(b) - (e)** the first five subradiant states, $|\text{sub}_m\rangle$, that the system evolves through, where multiple subensembles radiate out of phase causing their emission to destructively interfere.

The result of this measurement is shown in Figure 4.6(b), where the shaded area is the signal without atoms, which serves as a reference. The signal shows initially constructive interference with the local oscillator. As soon as the system passes through the first subradiant state, the detected signal is below that of the reference, revealing that the phase of the emitted light has changed. After passing through the second subradiant state, the interference is constructive again. The shape of the interference and the times at which the change in phase occurs agrees very well with our theoretical predictions and also with the zeros in the directly measured emission as depicted by vertical dotted lines in Figure 4.6. Concerning the absolute value of the phase, we note that the light that is emitted by the atoms is π-phase shifted relative to the excitation pulse. The excitation pulse undergoes a π phase shift as it crosses the fiber coupler twice. Therefore, the interference with the local oscillator is predicted to be constructive at $t = 0$, consistent with our measurements.

4.2.3 Ensemble State Prepared in the Experiment

The state that we prepare in our experiments is actually not the timed Dicke state for which we presented the analytical solutions in Section 4.1. To experimentally prepare a timed Dicke state in a one-dimensional ensemble of atoms, very short Dirac δ-like laser pulses would have to be used. Due to their large spectral distribution, these short pulses are less likely to be absorbed by atoms at the beginning of the ensemble, allowing the pulse to propagate further into the ensemble and excite all atoms equally. However, most of the pulse passes through the ensemble without interacting with the atoms at all. This method is therefore very inefficient and hinders reliable data collection of the emitted light due to poor signal-to-noise ratio. The same is true for a detuned excitation pulse that we discuss in Section 4.2.5. To address this challenge, we opted for a compromise by using longer boxcar-shaped pulses to excite the ensemble. Although this prepares a different state, the temporal dynamics of this state are qualitatively similar to those of the timed Dicke state and can be achieved with considerably higher probability.

Figure 4.7 shows the excited state amplitudes of the atoms for the state that we prepare initially and the first five subradiant states for the situation in the experiment. To calculate them, we numerically solve Equation (2.6) for OD = 31 and a 100-ns-long excitation pulse, the same parameters as in the measurements. In the initially prepared state, mostly the first part of the ensemble is excited unlike in the timed Dicke state where all atoms share the same excitation. However, the system still evolves through multiple subradiant states where subensembles of atoms radiate in phase opposition such that the waveguide-coupled light exhibits destructive interference, as depicted in Figures 4.7(b) – 4.7(f). Furthermore, since initially not all atoms have the same excited state amplitude, the system does not start with a maximally superradiant state and thus it has a reduced initial decay rate compared to the timed Dicke state, which has an $N\beta$-times enhanced decay rate.

4.2.4 Subradiant States as a Function of Optical Depth

So far we have described the dynamics of the emitted light for one specific case. Now we explore how the temporal dynamics depend on the optical depth of the ensemble. Figures 4.8(a) - 4.8(f) show the emission dynamics of the ensemble following the switch-off of the excitation pulse for increasing optical depths ranging from 12 to 31.

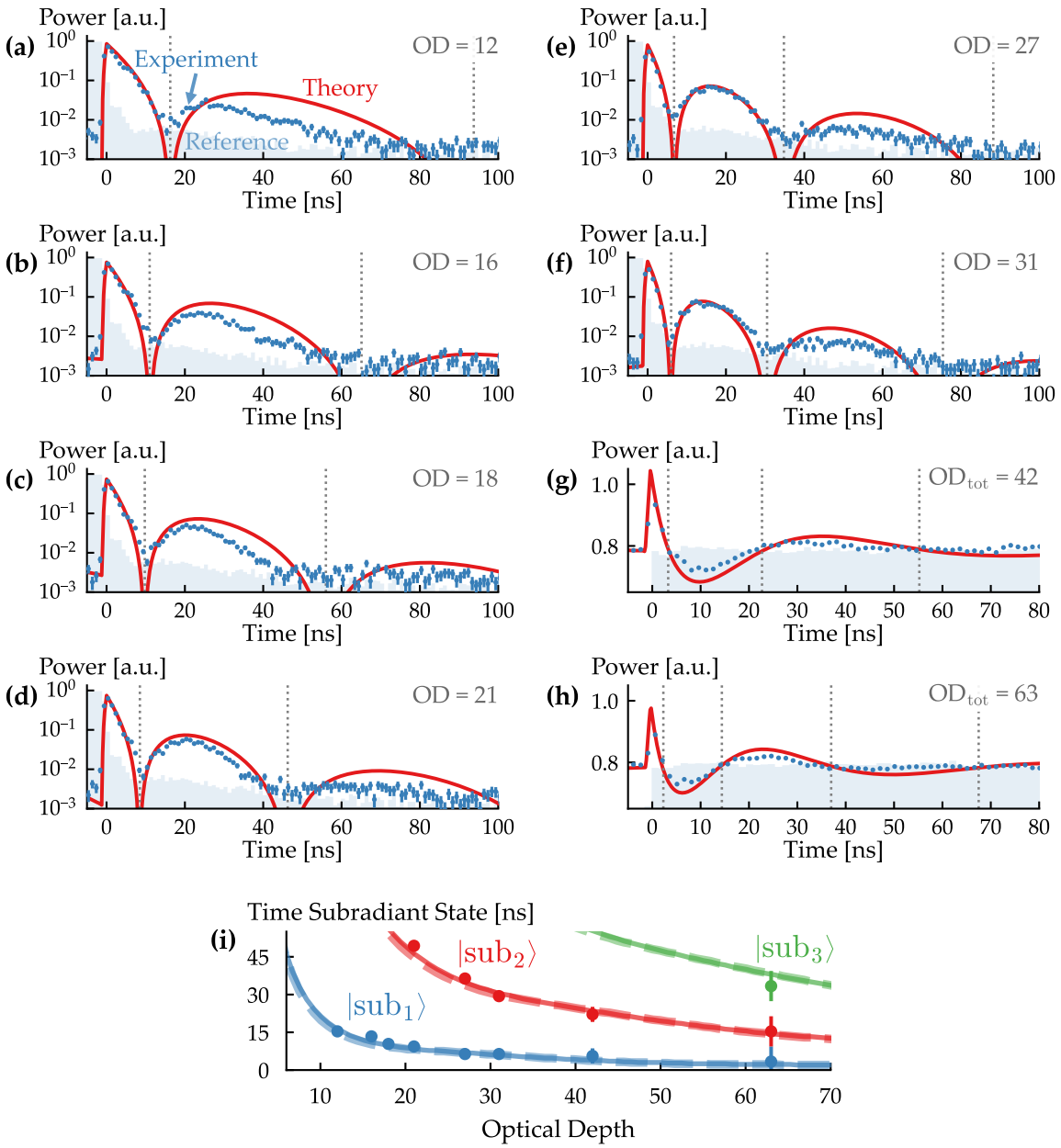

Figure 4.8: Measurements of the time of the subradiant states for increasing optical depth. **(a) - (f)** The temporal dynamics observed after the switch-off of the excitation pulse for ODs ranging from 12 to 31 show that for increasing ODs, the subradiant states occur earlier. **(g) - (h)** Homodyne measurements taken after two and three roundtrips through the cavity to achieve higher total optical depths for an ensemble with a single-pass optical depth of $OD_{sp} = 21$. The vertical dotted lines across all panels indicate the theoretically calculated times at which subradiant states occur. **(i)** The extracted times of the first three subradiant states as a function of optical depth are compared with theoretical predictions for $\beta = 0.55\%$ (solid line) and $\beta = 20\%$ (dashed line). The agreement of the data and the two predictions reveals that the dynamics are primarily influenced by the optical depth.

As the optical depth increases, the emission dynamics compresses in time and the ensemble reaches its subradiant states earlier.

It is challenging to achieve higher optical depths in our system, which would allow us to study higher-order subradiant states. As previously discussed in Section 3.4, the light that is outcoupled from the cavity after the mth roundtrip is equivalent to the results of a single pass through an ensemble with a total optical depth of $OD_{tot} = m \times OD_{sp}$, with OD_{sp} as the single-pass OD. This configuration enables us to conduct experiments at optical depths, which are difficult to achieve in a single-pass setup. However, each roundtrip through the cavity results in a decrease in signal, complicating the observation of higher-order subradiant states due to lower signal-to-noise ratio. To address this issue, we employed the local oscillator technique to measure the progression of the ensemble for higher optical depths. By measuring the interference of light fields in this homodyne setup, we achieved greater sensitivity compared to a direct measurement of the emitted light. From the results, which are shown in Figures 4.8(g) and 4.8(h), we can observe the system dynamics for equivalent ODs of $OD_{tot} = 2 \times OD_{sp} = 42$ and $OD_{tot} = 3 \times OD_{sp} = 63$. Notably, Figure 4.8(h) shows the passage of the state of the ensemble up to the third subradiant state. The calculated times when the ensemble transitions through its subradiant states are illustrated by dotted vertical lines in Figures 4.8(a) – 4.8(h).

Figure 4.8(i) shows the times extracted from the experiment when the ensemble reaches the first three subradiant states as a function of optical depth. The experimental data is represented by points with error bars that indicate the temporal uncertainty in determining the minimum transmission or phase change. The solid lines in the graph represent predictions with our theoretical model, calculated for the average β value in our experiment of $\beta = 0.55\%$. Conversely, the dashed lines are based on calculations assuming $\beta = 20\%$, which is the upper limit achievable in nanofiber-based atom-light interfaces [98]. The good agreement between the two theory predictions and our experimental results verifies that for $N \gg 1$, the temporal dynamics is influenced by the optical depth rather than the atom number as discussed in Section 4.1.2 for approximate solutions of the system.

4.2.5 Subradiance for Detuned Excitation

After studying the response of the ensemble for on-resonance excitation, we now want to assess the influence on the dynamics when the excitation pulse is detuned from resonance. We therefore repeat the experiments from Section 4.2.1, but with detuned light. The measurements are presented in Figure 4.9, where the optical power emitted by an ensemble with OD = 28 is plotted around the time of the first

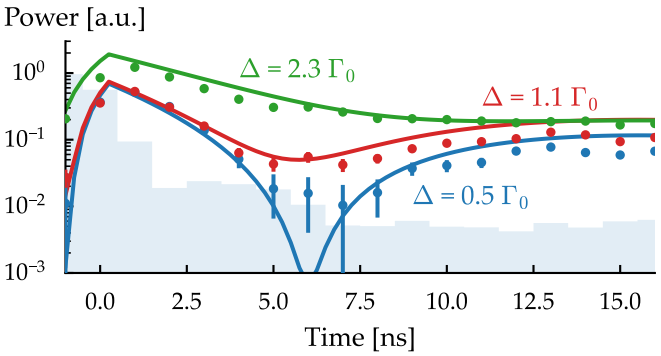

Figure 4.9: The temporal dynamics of the emission from an ensemble with OD = 28 after the excitation pulse turns off is shown for laser–atom detunings of $\Delta = 0.5\Gamma_o$ (blue), $\Delta = 1.1\Gamma_o$ (red) and $\Delta = 2.3\Gamma_o$ (green). As the detuning increases, the zero in emission disappears as the dispersive action of the atoms disrupts the destructive interference that causes the subradiant states.

subradiant state for the three detunings $\Delta = 0.5\Gamma_o$ in blue, $\Delta = 1.1\Gamma_o$ in red, $\Delta = 2.3\Gamma_o$ in green. The solid lines represent calculations based on our theoretical model. We observe that for increasing detuning, the emitted power still exhibits minima that, however, no longer reach zero emission. This is due to the fact that when light is moderately detuned from resonance and excites atoms, their dispersive properties alter the phase of the scattered light, which is no longer π out of phase with the incident field. Consequently, the phase shift between the different atoms is also no longer zero or π [99]. This disrupts the interference of the collective emission and prevents perfect destructive interference so that the light emitted into the waveguide does not reach zero.

To analyze this situation in more detail, we study how the emission evolves with increasing detuning. Figure 4.10 presents calculations of the light emitted from an ensemble across a detuning range of $\Delta = \pm 10\Gamma_o$ for OD = 28. The emitted power into the waveguide is represented by the colors in the colormap. At zero detuning, the emission shows multiple zeros in the waveguide-coupled power as the system passes through its subradiant states consistent with our measurements. As the detuning increases, these zeros gradually disappear as the destructive interference is suppressed due to the additional phase shift caused by the dispersive action of the atoms. When light is far detuned, the dispersion of the atoms becomes negligible, again allowing for destructive interference between subensembles. The emitted power consequently displays multiple minima. In this case, the ensemble state approximates a timed Dicke state due to the weak interaction between the excitation pulse and the ensemble, which results in a more uniform excitation of the atoms in the ensemble. Despite the

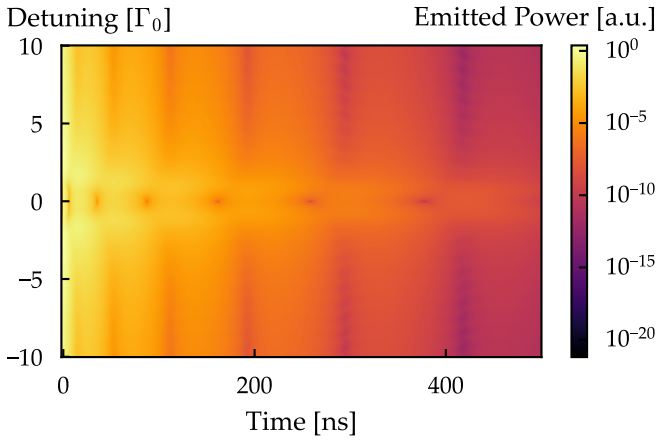

Figure 4.10: The calculated temporal response of the emitted power by the ensemble for detunings changing in the range $\Delta = \pm 10\Gamma_o$ and OD = 28. Depending on the degree of detuning, the dynamics change. Around $\Delta = 0$, we see the dynamics that we discussed so far, where the ensemble passes through subradiant states. For moderately detuned light, however, the subradiant states gradually disappear as the interference is not destructive any longer, while for larger detuning, they reappear, albeit at later times. This can be attributed to the ensemble being prepared in a timed Dicke state for large detunings, which displays similar dynamics to those observed in the ensemble state prepared in our experiments.

difference in timing of these minima compared to the zero detuning case, the qualitative dynamics remain similar.

4.3 ADDITIONAL CONSIDERATIONS

In this section, we present and discuss some additional considerations about the theory and the phenomena that we observed in the experiments, namely, the analytical solutions for the ensemble state that we prepared in the experiment, the orthogonality of the involved states and the influence of a nonuniform β distribution.

4.3.1 Analytical Solutions for the Ensemble State in the Experiment

We can also analytically solve the system for the excitation pulse used in the experiment that we discussed in Section 4.2.3. Given that the length of the excitation pulse is sufficiently long to allow the system to approximately reach a steady state ($100\,\text{ns} > 3\tau_{\text{at}} = 3 \times 30.4\,\text{ns}$) and that we are only interested in the dynamics after the pulse switches off, we can model the pulse as a Heaviside θ-like pulse ($u_{\text{in}}(t) \propto \theta(-t)$).

This allows us to solve Equation (2.6) analytically in terms of Laguerre polynomials with additional correction terms. When we regard the simple system with $N = 4$ atoms that we discussed previously, the amplitudes of the excited states can be determined as follows

$$\phi_1(t) = \frac{e^{-\frac{\Gamma_0}{2}t}}{\sqrt{N}} L_0^{(0)}(\beta\Gamma_0 t)\,, \tag{4.38}$$

$$\phi_2(t) = \frac{e^{-\frac{\Gamma_0}{2}t}}{\sqrt{N}} \left[L_1^{(0)}(\beta\Gamma_0 t) - 2\beta\right]\,, \tag{4.39}$$

$$\phi_3(t) = \frac{e^{-\frac{\Gamma_0}{2}t}}{\sqrt{N}} \left[L_2^{(0)}(\beta\Gamma_0 t) - 4\beta + 2\beta^2(2 + \Gamma_0 t)\right]\,, \tag{4.40}$$

$$\begin{aligned}\phi_4(t) = \frac{e^{-\frac{\Gamma_0}{2}t}}{\sqrt{N}} \Big[&L_3^{(0)}(\beta\Gamma_0 t) - 2\beta(3 + 6\beta - 4\beta^2) + \\ &+ \beta^2(6t\Gamma_0 - 4\beta t\Gamma_0 - \beta^2 t^2 {\Gamma_0}^2)\Big]\,.\end{aligned} \tag{4.41}$$

These solutions share properties with those described for the timed Dicke state in Equation (4.31), in that they are composed of polynomials where each polynomial for the nth atom has $n-1$ distinct zeros. As a result, the overall temporal dynamics of the system are qualitatively similar. However, there are variations in the exact composition of the $N-1$ subradiant states and in the times at which the system transitions into these states.

4.3.2 Orthogonality of the Timed Dicke and Subradiant States

To ensure that the superradiant timed Dicke state and the subradiant states provide a complete description of the Hilbert space of an ensemble where a single excitation is shared among all emitters, these basis states have to be orthogonal to each other. Although we are currently unable to provide a general proof that the timed Dicke and all subradiant states are orthogonal to each other based on Equations (4.31) and (4.32), we have numerically verified this property up to $N = 200$. Furthermore, when using the simplified solutions given in Equations (4.36) and (4.37) for large numbers of emitters and $\beta \ll 1$, the orthogonality of the subradiant states can be proved based on the properties of Bessel functions. For the ith and jth subradiant state with $i \neq j$ it can be demonstrated that the overlap between two Bessel functions is zero

$$\int_0^N J_0\left(x_i\sqrt{\tfrac{n-1}{N}}\right) J_0\left(x_j\sqrt{\tfrac{n-1}{N}}\right) dn = 0\,, \tag{4.42}$$

where x_m is the mth zero of the Bessel function $J_1(x)$. Substituting $(n-1)/N = \xi^2$ and $dn = 2N\xi d\xi$ the integral can be rewritten as

$$\begin{aligned} & 2N \int_0^1 \xi J_0(x_i\xi) J_0(x_j\xi) d\xi = \\ = \quad & \frac{x_i J_0(x_j) J_1(x_i) - x_j J_0(x_i) J_1(x_j)}{x_i^2 - x_j^2} \overset{i\neq j}{=} 0, \end{aligned}$$

which proves that the subradiant states are orthogonal.

4.3.3 Ensembles with Nonuniform Coupling Strengths

So far we have discussed solutions for the scenario where all atoms are equally coupled to the propagating mode with a coupling strength β. In an experiment this is not the case, as each atom has a slightly different coupling strength β_n with the guided mode. Finding simple analytical solutions for the time evolution of the system becomes challenging when β varies from atom to atom. Nevertheless, it is reasonable to assume an average β value for all atoms, since most relevant properties remain qualitatively unchanged.

To demonstrate this claim, we plot in Figure 4.11(a) the calculated waveguide-coupled power, $|\chi_N(t)|^2$, once for the same parameters as in Figure 4.3(a) of $N = 4$ atoms and a uniform $\beta_n = 0.4$ in blue and once for a nonuniform β distribution of $\beta_1 = 0.2$, $\beta_2 = 0.3$, $\beta_3 = 0.5$ and $\beta_4 = 0.6$ in green, which has the same average β. This comparison shows that the differences in coupling strength primarily affect the response of the system on longer time scales. This can be explained intuitively by recognizing that the light immediately before the nth atom is influenced only by the sum of the excitation amplitudes of the atoms before it, each weighted by their respective β factors, see also Equation (4.32). Consequently, as long as the ensemble can be segmented into sufficiently large sub-ensembles that smooth out the atom-to-atom variations in β, the overall temporal evolution remains unaffected. Figure 4.11(b) shows, for example, the normalized excited state amplitudes of the first subradiant state for a nonuniform and uniform beta distribution which still have the same shape. On longer time scales, however, the sub-ensembles exhibit a number of phase reversals proportional to the number of atoms, see for example the excited state probabilities in Figure 4.4 for higher subradiant states, making the system increasingly sensitive to variations in β.

To explore the impact of a nonuniform β distribution on the dynamics, we calculated the power coupled to the waveguide for a worst-case scenario of β uniformly distributed between 0% and 20%. The distribution of atoms around the nanofiber has not been characterized

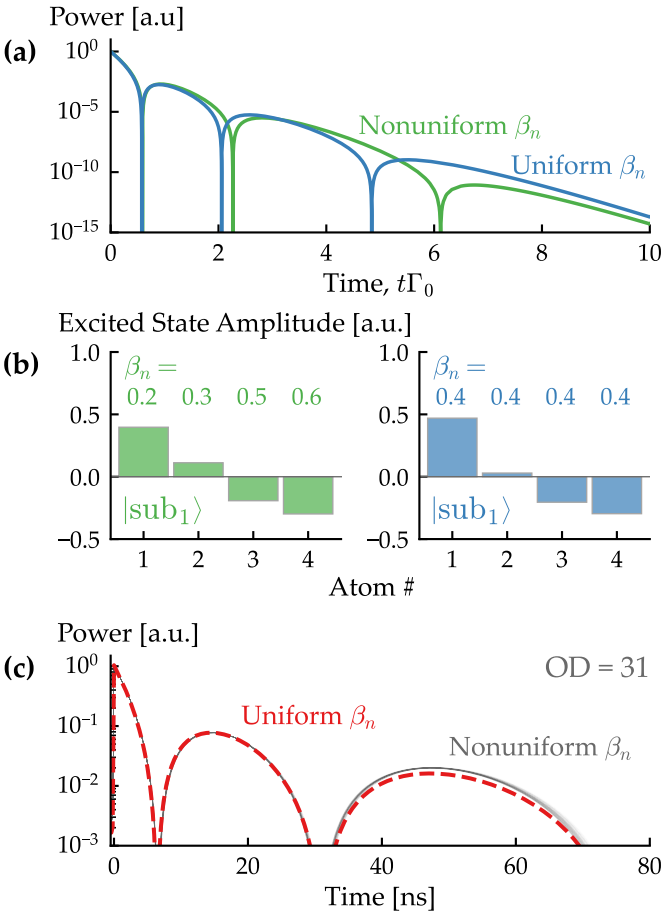

Figure 4.11: Comparison of a uniform and a nonuniform distribution of atom-light coupling strength β_n on the dynamics. **(a)** The temporal response of the waveguide-coupled power $|\chi_N(t)|^2$ for $N = 4$ atoms with a uniform coupling strength $\beta_n = 0.4$ is shown in blue and for a nonuniform distribution $\beta_1 = 0.2$, $\beta_2 = 0.3$, $\beta_3 = 0.5$ and $\beta_4 = 0.6$ in green. Qualitatively the dynamics are very similar, but the times of the subradiant states is different. **(b), (c)** The excited state amplitudes of the first subradiant states in case of a uniform and a nonuniform distribution are similar. **(d)** Comparing the calculated optical power in the waveguide for the parameters in our experiment of OD = 31 for, in red, an average uniform $\beta = 0.55\%$ and, in gray, for 250 different β values randomly distributed between 0 and 20% reveals that the dynamics are the same for the time scales relevant to our experiment and that it depends mainly on OD.

and only the average β value was measured [62], which was found to be $\beta = 0.55\% \pm 0.13\%$. From theoretical calculations, it is known that β ranges between 0% and about 20% for atoms far away or on the surface of the nanofiber [98], respectively. Figure 4.11(c) shows the individual curves for 250 random β configurations as gray lines and as a comparison the results for the uniform β value of our experiment as a red-dashed line. The unidirectional model (Section 2.2.1)

assumes the same experimental situation depicted in Figure 4.6(a) with an optical depth of OD = 31 and excitation with a 100-ns-long boxcar-shaped pulse. The comparison of these two predictions reveals that, within the time scales relevant to our experiment, even such a broad distribution of β values has only a marginal effect on the temporal dynamics, which depend primarily on OD. Additionally, the geometric configuration of the system tends to favor smaller β values, further reducing the relevance of this effect.

4.4 SUMMARY AND CONCLUSIONS

This chapter presented an in-depth study of the collective emission dynamics of an ensemble of atoms coupled via a single optical mode. For an ensemble consisting of N emitters prepared in a timed Dicke state where a single excitation is shared, we derived analytical solutions of the cascaded interaction model based on Laguerre polynomials. The temporal evolution of the emission of the ensemble evolves from the superradiant timed Dicke state sequentially through its $N-1$ subradiant states. When the ensemble is in a subradiant state, its emission into the waveguide mode is suppressed due to destructive interference of subensembles emitting out-of-phase.

We validated the theoretical predictions using our experimental system, where an ensemble of cesium atoms is coupled via the evanescent field around a nanofiber. We prepared the ensemble by launching boxcar-shaped light pulses on resonance with the cesium D_2 transition. This preparation method produces a state with qualitatively similar dynamics to the timed Dicke state, but with a much higher preparation probability than using very short pulses or far-detuning the light. We analyzed the temporal emission dynamics following the switch-off of the excitation pulses and observed the ensemble passing through the first two subradiant states, characterized by a drop in the emitted power to zero. Using homodyne measurements, we found that the phase of the emitted light changes each time the ensemble passes through a subradiant state, further confirming theoretical predictions. Furthermore, we investigated the influence of the optical depth on the emission dynamics and found that increasing the optical depth causes subradiant states to occur earlier in time. The extracted times for the subradiant states agreed very well with theoretical predictions, which we found to depend largely on the total optical depth, $\mathrm{OD} \simeq 4\beta N$, rather than on the absolute number of emitters, N, or the atom-waveguide coupling strength, β. This finding is supported by approximate solutions for large numbers of emitters

and small β, which show a dependence only on OD. Additionally, assuming a nonuniform distribution of β values for each emitter does not qualitatively influence the dynamics further confirming that the dynamics depend mostly on OD.

5 TRANSITION BETWEEN CAVITY AND WAVEGUIDE QED

The results presented in this chapter have been published in [100]:
Daniel Lechner, Riccardo Pennetta, Martin Blaha, Philipp Schneeweiss, Arno Rauschenbeutel, and Jürgen Volz.
Light-Matter Interaction at the Transition between Cavity and Waveguide QED.
Physical Review Letters, 131(10):103603, 2023.

Experiments on light–matter interactions, are typically performed within the frameworks of either cavity QED or waveguide QED, which are usually considered as distinct regimes. In this chapter, we will explore the connection between these regimes experimentally and theoretically, and discuss the transition between the two in regimes that have so far been the subject of limited research.

Depending on the cavity length, it is possible to identify different regimes of cavity QED by comparing the roundtrip time, t_{rt}, to the emitter lifetime, τ_{at}, as shown in Figure 5.1. In very short cavities, where $t_{\mathrm{rt}} \ll \tau_{\mathrm{at}}$, the system operates in the single-mode cavity QED regime, where the free spectral range of the cavity is much larger than the linewidth of the emitter. The emitter can thus only interact with a single cavity mode. This regime is well-described by the Jaynes-Cummings and Tavis-Cummings models and is usually studied in the strong coupling regime, where the coupling rate between the cavity field and the quantum emitter, g, exceeds the cavity's and the emitter's decay rates. In the frequency domain, the typical signature of strong interaction is the splitting of the resonator mode, the phenomenon of vacuum Rabi splitting [19]. In the time domain, this corresponds to vacuum Rabi oscillations, where the quantum emitter and the cavity field coherently exchange energy [17, 18] with the vacuum Rabi frequency $2g$.

However, as the cavity length increases, the dynamics can deviate drastically from the single-mode cavity QED case. The extreme limit of this is reached in the case of waveguide QED, which can be regarded as cavity QED with the cavity mirrors at infinite distance, meaning $t_{\mathrm{rt}} \to \infty$. In waveguide QED, propagating photons interact successively with emitters that are coupled to the guided mode of a waveguide.

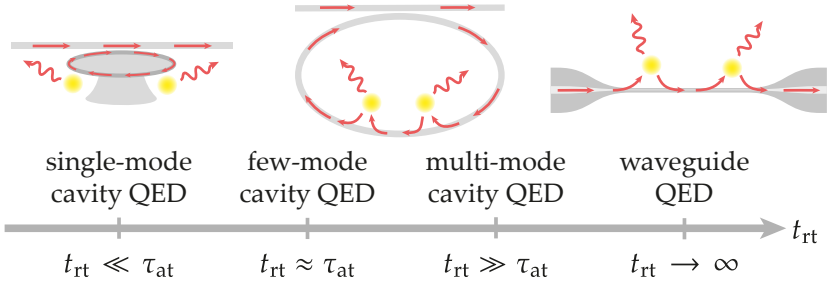

Figure 5.1: Overview of the regimes of light-matter interaction considered in this chapter. These regimes are distinguished by the ratio between the resonator roundtrip time, t_{rt}, and the atomic lifetime, τ_{at}, which influences the behavior of light-matter interaction within a cavity. The waveguide QED case can be considered as a special case of an infinite-length cavity, where $t_{rt} \to \infty$. Emitters are shown to be coupled to different resonators typical for the respective regime: a whispering-gallery mode resonator in the single-mode cavity QED regime, a fiber-ring resonator in the few-mode and multi-mode cavity QED regimes, and a nanofiber in the waveguide QED regime.

This corresponds to the situation in our experiment when light makes a single pass through an atomic ensemble coupled to a nanofiber. As $\nu_{FSR} \to 0$ in this case, the emitters interact with a continuum of frequency modes. As a result, phenomena such as the vacuum Rabi splitting loose their meaning and light–matter coupling strength is instead measured for a single atom by the β factor or by the ensemble's optical depth (OD $\approx 4\beta N$) which determine the dynamics of the transmitted light.

Despite the extensive study of single-mode cavity QED and waveguide QED, there has been limited research on the regimes that lie between these two regimes. The lack of research can be attributed to the challenges of increasing the length of conventional free-space cavities, such as Fabry-Pérot cavities, which are predominately used in experimental setups in cavity QED. In these cavities, the cavity length cannot arbitrarily be changed. Due to diffraction, an increase in the distance between the mirrors requires a corresponding increase in mirror diameter to maintain the size of the beam waist at the focus. This ensures that the coupling strength with the atoms remains unchanged, which limits cavity lengths to centimeters. For most quantum emitters, such short cavities still support only a single frequency mode, making it challenging to study multi-mode interactions.

In our system, we can overcome these limitations as our nanofiber-based atom–light interface is embedded within a fiber-ring resonator whose length can easily be changed. The negligible propagation loss of optical fibers ensure that the cooperativity parameter is independent of

the cavity length, which enables our system to operate in the collective strong coupling regime for arbitrary cavity lengths. By varying the length of the fiber-ring, we can thus control the density of frequency modes of the cavity and explore regimes where more than one cavity mode interacts with the coupled emitters.

Previous work in our group has already started to explore the regime of multi-mode cavity QED, where emitters are strongly coupled to a resonator with $t_{rt} \gg \tau_{at}$. In the literature, this regime has been termed superstrong coupling [46, 48, 62] or multi-mode strong coupling [47, 101] regime of cavity QED , and it is characterized by many longitudinal cavity modes interacting with the emitters. However, the few-mode cavity QED regime that we describe in this chapter, where $t_{rt} \approx \tau_{at}$, has so far not been explored. This regime offers valuable insights into the transition from cavity to waveguide QED and into the nature of ensemble–cavity dynamics.

To investigate these phenomena, we perform measurements and calculations for three cavity lengths, examining the regimes where $t_{rt} \ll \tau_{at}$, $t_{rt} \approx \tau_{at}$, and $t_{rt} \gg \tau_{at}$. Considering the excited state lifetime of cesium of $\tau_{at} = 30.4\,\text{ns}$, we compare cavities with lengths $L_{cav} = 5\,\text{cm}$ ($t_{rt} = 241.7\,\text{ps}$), $L_{cav} = 5.8\,\text{m}$ ($t_{rt} = 28.3\,\text{ns}$), and $L_{cav} = 45.4\,\text{m}$ ($t_{rt} = 219.7\,\text{ns}$). Our current system is not designed for the very short cavities required to reach single-mode cavity QED experiments, so we rely on calculated results. This is not an issue, as this regime has already been extensively studied in literature [17, 19, 102, 103]. For the presented data, we have chosen the system parameters such that the ratio between the ensemble–cavity coupling rate, g, and the dominating loss rate in the system ($g/\max(\kappa, \Gamma_o/2)$) is approximately equal in the different settings. In the Tavis-Cummings model, this ratio determines the number of Rabi oscillations the system undergoes before a steady-state is reached. For short cavities, the dominating loss rate is usually the cavity loss rate, κ, while in long cavities the spontaneous emission rate, Γ_o, dominates.

In this chapter, we first characterize the empty cavity response to extract the cavity parameters. We then discuss the system response in the different regimes with coupled atoms in the time and frequency domain, focusing on phenomena such as Rabi oscillations and their dependence on cavity length. Finally, we study the influence of various system parameters and present measurements with a probe laser field detuned from the central cavity resonance.

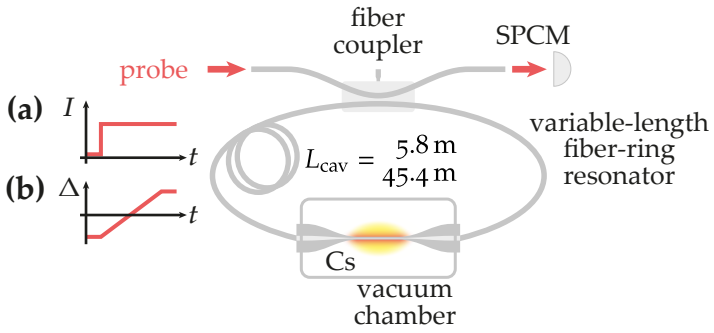

Figure 5.2: The experimental setup and probe sequence of a fiber-ring resonator coupled to an ensemble of cesium (Cs) atoms. The resonator length can be adjusted by varying the length of the optical fiber in the fiber-ring, with measurements shown for two lengths: L_{cav} = 5.8 m and 45.4 m, corresponding to the few-mode and multi-mode cavity QED regimes. **(a)** For time domain measurements, the probe laser field is rapidly turned on. **(b)** For frequency domain measurements, the probe laser field is swept across the atomic resonance. The transmitted light in the coupling fiber is recorded using a single photon counting module (SPCM).

5.1 EMPTY RESONATOR MEASUREMENTS AND CAVITY PARAMETERS

We begin our discussion by characterizing the response of the empty cavity without atoms. This allows us to determine the cavity parameters by fitting the cascaded interaction model to the response, which is useful for the following analysis involving atoms as it reduces the number of free parameters for the fit. We investigate the response of our system after turning on a laser field that is resonant to the cavity mode, which in turn is tuned to the atomic resonance frequency, as depicted in the sketch of the setup in Figure 5.2(a). The rise time of the laser field of $\approx$ 1 ns is much faster than τ_{at} = 30.4 ns.

Figure 5.3 shows the transmitted light in the absence of atoms for the three cavity lengths that we compare in this chapter: 5 cm, 5.8 m and 45.4 m. These lengths correspond to the single-mode cavity QED regime, the few-mode cavity QED regime and the multimode cavity QED regime. For the 5-cm-long single-mode resonator in Figure 5.3(a), we only present the theoretical transmission as our current experimental system does not extend into this regime. Figures 5.3(b) and 5.3(c) show the measured transmitted light power after turning on a resonant laser field for the 5.8-m and 45.4-m-long resonator, respectively, alongside the fits using the cascaded interaction model extended for resonators (see Section 2.2.2). The free parameters of the model used for fitting are the amplitude transmission coefficient of the coupler, t_{cpl}, the amplitude roundtrip transmission coefficient of the

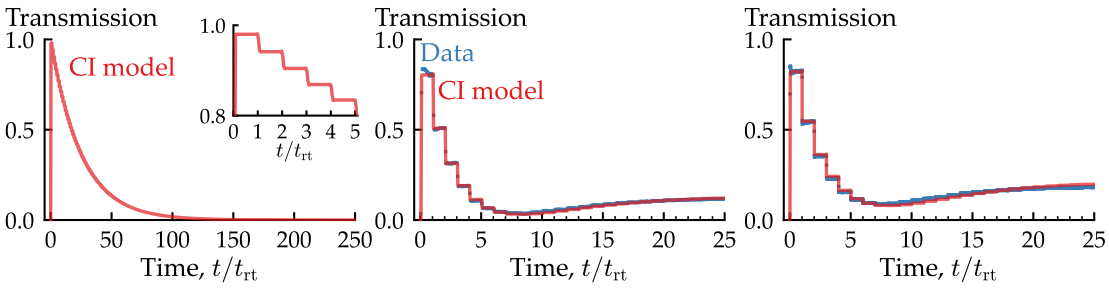

(a) Single-mode cavity QED, $t_{rt} \ll \tau_{at}$, $L_{cav} = 5\,\text{cm}$

(b) Few-mode cavity QED, $t_{rt} \approx \tau_{at}$, $L_{cav} = 5.8\,\text{m}$

(c) Multi-mode cavity QED, $t_{rt} \gg \tau_{at}$, $L_{cav} = 45.4\,\text{m}$

Figure 5.3: Transmission measurements in the time domain normalized to the cavity roundtrip time t_{rt} for an empty cavity in the three considered regimes. Experimental data (blue squares) and the fitted cascaded interaction (CI) model (red solid lines) are shown until a steady state is reached. An inset for the single-mode cavity QED case shows a toom of the behavior for short time scales, also revealing a stepwise decrease in transmission, similar to the other two cavities. This feature would be difficult to observe in experiments due to the limited time resolution of most detectors.

cavity, t_{cav}, the laser–cavity detuning, Δ_c, and the cavity roundtrip time, t_{rt}. The model's fit closely matches the measured data. The parameters extracted from the fit as well as additional typical cavity parameters are displayed in Table 5.1. The parameters for the calculated 5-cm-long cavity are chosen to be critically coupled, while the 5.8-m-long and the 45.4-m-long experimental cavities are slightly overcoupled. This increases the amount of light that is outcoupled each roundtrip, which increases the visibility of the dynamics that we want to observe later.

The transmitted power decreases over time. It decreases quasi continuously for the single-mode cavity QED case in Figure 5.3(a) and in steps for the cavities in the few-mode and multi-mode cavity QED regimes shown in Figures 5.3(b) and 5.3(c). Due to long roundtrip times in these cases, we can actually observe the transmission decreasing as the cavity field builds up stepwise. In the case of a single-mode cavity, we show these steps in the inset of Figure 5.3(a), however, these steps would only be visible in experiments with very fast photodetectors. To explain the steps, it is necessary to first understand what happens when light couples to the ring resonator and the cavity field builds up. There are two light fields that contribute to the dynamics: the light field that is coupled into the resonator at the fiber coupler and propagates inside the resonator, and the light field that is transmitted through the fiber coupler and continues in the coupling waveguide. The field that remains in the coupling fiber then interferes with the light that is outcoupled each roundtrip. The amount of light coupled into the resonator is determined by the amplitude coupling coefficient of the coupler, $c_{cpl} = \sqrt{1 - t_{cpl}^2}$, and the fraction of light that remains in the coupling waveguide is determined by the amplitude transmission

Table 5.1: Cavity parameters for the three resonators considered in this chapter. Some parameters are extracted from the fit of the measured time domain data with the cascaded interaction model, while others are derived from these parameters. Values in parenthesis indicate the 95% confidence interval of the measured parameter, propagated from the fit errors. For the D_2 line of cesium, the excited state decay rate is $\Gamma_0 = 2\pi \times 5.23(3)\,\mathrm{MHz}$, which corresponds to an excited state lifetime of $\tau_{at} = 30.4(2)\,\mathrm{ns}$ [87].

		$t_{rt} \ll \tau_{at}$	$t_{rt} \approx \tau_{at}$	$t_{rt} \gg \tau_{at}$
cavity length	$L_{cav} = \frac{c_0 t_{rt}}{n}$	5.0 cm	5.843(5) m	45.423(5) m
cavity roundtrip time	t_{rt} (from fit)	241.67 ps	28.26(3) ns	219.70(3) ns
free spectral range	$\nu_{FSR} = \frac{1}{t_{rt}}$	4.14 GHz	35.38(3) MHz	4.5517(6) MHz
optical depth	OD (from fit)	1.42	6.61(7)	14.4(1)
average laser–cavity detuning	Δ_c (from fit)	0	307(2) kHz	60.2(1) kHz
ensemble–cavity coupling rate	$g = \sqrt{\frac{OD}{4}\Gamma_0 \nu_{FSR}}$	$2\pi \times 34.98\,\mathrm{MHz}$	$2\pi \times 6.98(4)\,\mathrm{MHz}$	$2\pi \times 3.70(2)\,\mathrm{MHz}$
total cavity loss rate	$\kappa = \kappa_{ext} + \kappa_{int}$	$2\pi \times 13.11\,\mathrm{MHz}$	$2\pi \times 919.6(3)\,\mathrm{kHz}$	$2\pi \times 114.2(1)\,\mathrm{kHz}$
external cavity loss rate	$\kappa_{ext} = \frac{\nu_{FSR}}{2}(1 - t_{cpl}^2)$	$2\pi \times 6.55\,\mathrm{MHz}$	$2\pi \times 554(1)\,\mathrm{kHz}$	$2\pi \times 65.0(1)\,\mathrm{kHz}$
intrinsic cavity loss rate	$\kappa_{int} = \frac{\nu_{FSR}}{2}(1 - t_{cav}^2)$	$2\pi \times 6.55\,\mathrm{MHz}$	$2\pi \times 365(1)\,\mathrm{kHz}$	$2\pi \times 49.2(1)\,\mathrm{kHz}$
amplitude transmission coefficient coupler	t_{cpl} (from fit)	0.99	0.896(4)	0.9060(1)
amplitude transmission coefficient cavity	t_{cav} (from fit)	0.99	0.9329(2)	0.9295(1)
total roundtrip transmission	$T_{RT} = \lvert t_{cav} t_{cpl} \rvert^2$	96.1%	69.9(2)%	70.91(4)%
intrinsic Finesse	$F = \pi \nu_{FSR} / \kappa_{int}$	315.7	48.4(2)	46.2(1)
cooperativity	$C = \frac{g^2}{\kappa \Gamma_0}$	17.84	10.1(1)	22.9(2)
ratio between g and dominating loss rate	$g / \max(\kappa, \Gamma_0/2)$	2.67	2.67(2)	1.413(6)

coefficient of the coupler, t_{cpl}, see also the sketch in Figure 2.8. From $t = 0$ until $t = t_{rt}$, the observed light at the output is the light that remains in the coupling fiber, with a transmitted power proportional to $|t_{cpl}|^2$. At $t = t_{rt}$, the transmitted power reduces by a step. This happens because the light in the resonator completes its first full roundtrip and is outcoupled at the fiber coupler, where it interferes with the light that remains in the coupling fiber. Each time light couples across a fiber coupler, it accumulates a $\pi/2$ phase shift, resulting in a π phase shift when it is outcoupled again, leading to destructive interference between the outcoupled light and the light in the coupling waveguide. The light that is not outcoupled at the coupler after one roundtrip then stays in the resonator and constructively interferes with the light that is incoupled at the coupler. This constructive interference is what

causes a cavity field to build up. The combined fields propagate through the cavity for another roundtrip, and at $t = 2t_{rt}$, a fraction of this light is outcoupled again. As the overall field in the cavity increases with each roundtrip, the transmitted power also reduces stepwise. This process repeats with each roundtrip, and the overall transmission decreases as the cavity field builds up until a steady state is reached.

Overall, the observed transmission drops on a timescale that is determined by $1/\kappa$, where $\kappa = \kappa_0 + \kappa_{ext}$ represents the total cavity loss rate. In the calculated case of the 5-cm-long single-mode resonator in Figure 5.3(a), the transmission decays to zero. However, the measured data in Figure 5.3(b) and 5.3(c) initially decreases to near zero but then increases before settling at a non-zero steady state power. This behavior arises because the cavity is slightly overcoupled [104] rather than critically coupled, as assumed in the calculated case. As the cavity field builds up, the transmitted light drops to a minimum when the outcoupled field is equal to the field that remains in the coupling fiber. Beyond this point, the outcoupled field dominates, leading to a non-zero steady-state transmission and a π-phase shift in the overall output field. The transmitted power in the steady state is also influenced by the laser–cavity detuning, Δ_c, relative to the cavity resonance. Due to unavoidable shot-to-shot fluctuations ($\approx$1% of ν_{FSR}), some detuning is always present. In our model, we assume an average laser–cavity detuning for this effect.

5.2 MEASUREMENTS WITH ATOMS

We now study the response of the system when it is coupled to an ensemble of atoms. Figure 5.4 presents the response of the system in both the frequency and time domain. For the single-mode cavity, we only show calculated curves. In order to measure the time domain response, we rapidly turn on the probe laser field and record the transmitted light (Figure 5.2(a)), while for measuring the frequency spectra, we sweep the frequency of the probe laser field across the atomic resonance (Figure 5.2(b)). The fits in the plots with the cascaded interaction model were calculated with the OD as the only free parameter. All other cavity parameters were taken from the empty cavity measurements. The calculations based on the Tavis-Cummings model were performed with the values that were obtained from the cascaded interaction fit.

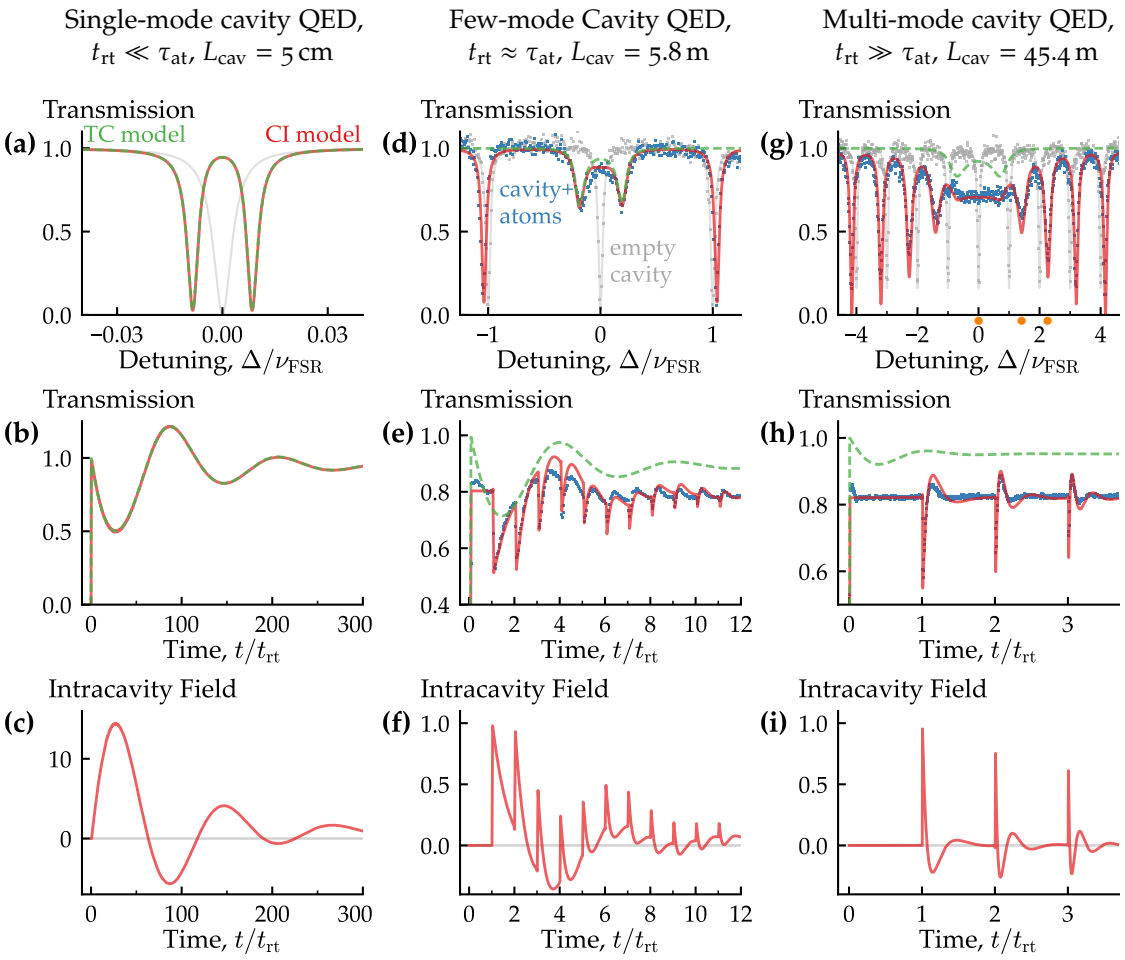

Figure 5.4: Ensemble–cavity responses for three ring cavities with increasing lengths, L_{cav}, in **(a, d, g)** the frequency domain, in **(b, e, h)** the time domain and **(c, f, i)** the corresponding normalized intracavity fields right before light is outcoupled at the fiber coupler. The experimental data (blue squares) is shown together with the fits with the cascaded interaction (CI) model (red solid line) and the predictions with the Tavis-Cummings (TC) model (green dashed lines). Additionally, the empty cavity responses in the frequency domain are also given together with the fits by the CI model (gray squares and solid lines). The cavity response in the few-mode cavity QED regime simultaneously exhibits features from the single-mode and of the multi-mode cavity QED regime. t_{rt}: resonator roundtrip time, τ_{at}: excited state lifetime of emitter, Δ: laser–atom detuning, ν_{FSR}: resonator free spectral range. The orange dots in **(g)** represent the setting for the detuned measurements in Section 5.4.

5.2.1 Single-Mode Cavity QED Regime

At first, we discuss the single-mode cavity QED regime, where the system response for a 5-cm-long cavity is presented in Figures 5.4(a) – 5.4(c). The fiber-ring cavity has a roundtrip time of $t_{rt} = 241.7\,ps \ll \tau_{at} = 30.4\,ns$ and is coupled to an atomic ensemble with OD = 1.42.

The spectrum in the frequency domain in Figure 5.4(a) shows a distinct vacuum Rabi splitting of $2g$ around zero detuning, $\Delta = 0$.

This splitting of the resonator mode stems from the coupling of the atomic ensemble to the resonator. Accordingly, the system's time domain response in Figure 5.4(b) displays conventional sinusoidal Rabi oscillations with a Rabi frequency of $2g$ that are damped due to dissipation. The time domain signal in transmission arises from the interference of the light field that remains in the coupling fiber and the fraction of the light field that is outcoupled from the cavity (see also the explanation in Section 5.1). Due to the π-phase shift of the outcoupled light, this interference is destructive. Consequently, the transmitted signal shows the inverted behavior of the intracavity field depicted in Figure 5.4(c), where we plot the intracavity field amplitude at the position right before the cavity field exits at the fiber coupler, $E_{\mathrm{cav}}(t)$. We normalize this field to the amplitude of the field that entered the cavity at $t = 0$, $E_{\mathrm{in}} = u_{\mathrm{in}}\, c_{\mathrm{cpl}}$, which only depends on the probe field amplitude, u_{in}, and the coupling coefficient of the coupler, c_{cpl}. Also, since the excitation field is resonant with both the cavity and the atomic resonance, the ratio $E_{\mathrm{cav}}(t)/E_{\mathrm{in}}$ is real-valued, so that plotting the field amplitude is sufficient to describe the field. Without atoms in the cavity, the intracavity field would grow monotonously until it saturates at its steady state value. However, in the presence of atoms in the cavity, the intracavity field oscillates as a result of the periodic and coherent exchange of energy between the light field in the cavity and the energy stored in the atoms, which lies at the origin of Rabi oscillations.

The predictions of the Tavis-Cummings and the cascaded interaction model are shown in Figures 5.4(a) and 5.4(b) and are in good agreement. This is expected, as the Tavis-Cummings model is specifically designed for the single-mode cavity case and, therefore, agrees with our more general cascaded interaction model. However, the Tavis-Cumming model does not account for the steps in transmission due to the progressive cavity build up discussed earlier because it does not include a position-dependent resonator field.

5.2.2 Multi-Mode Cavity QED Regime

We continue our discussion at the other extreme end of cavity QED by investigating light–matter interaction with a very long ring resonator operating in the multi-mode cavity QED regime. In this regime, the atomic ensemble interacts not with a single, but with multiple resonator modes at the same time. Figures 5.4(g) – 5.4(i) show experimental and theoretical results for a 45.4-m-long ring resonator coupled to an ensemble of cold atoms with OD = 14.4. For such a long resonator, the roundtrip time is much larger than the atomic

lifetime: $t_{rt} = 219.7\,\text{ns} \gg \tau_{at} = 30.4\,\text{ns}$. The system thus operates in the multi-mode strong coupling regime, where the ensemble–cavity coupling strength, g, is comparable to or exceeds the free spectral range, ω_{FSR}, of the resonator.

The frequency response of the system in Figure 5.4(g) highlights the multi-mode nature of the light-matter coupling in this regime. In addition to the splitting of the central resonance, the adjacent resonator modes also shift outwards compared to the empty resonator spectrum. As the frequency spectrum for such a long resonator is much denser ($\omega_{FSR} = 2\pi \times 4.55\,\text{MHz} < \Gamma_o = 2\pi \times 5.24\,\text{MHz}$), the atoms interact with multiple resonator modes causing an outwards shift of the resonances [46, 62]. This shift of the individual modes decreases for modes detuned from the central cavity mode as the interaction with the atoms is weaker for larger detuning [99]. For comparison, we plot predictions of both the cascaded interaction and the Tavis-Cummings models. The Tavis-Cummings model qualitatively reproduces the width of the splitting, but otherwise shows completely different features compared to our data. In contrast, the cascaded interaction model agrees closely with the observed features.

In the time domain measurements presented in Figure 5.4(h), the dynamics for our very long cavity differ significantly from the standard cavity QED predictions. Instead of Rabi oscillations that would be expected for a strongly coupled ensemble, the transmission signal displays sharp features separated by the roundtrip time. These observations closely match the predictions by the cascaded interaction model, while the predictions from the Tavis-Cummings model do not align at all with the experimental data.

To understand the origin of these sharp features, we will again examine the calculated intracavity field in Figure 5.4(i). At first, the intracavity field is zero as the light field first has to complete one roundtrip to arrive at the output coupler. At $t/t_{rt} = 1$, the sudden switch-on of the laser field results in a sudden increase of the resonator field, which then begins to decay immediately due to the presence of the atoms. The decay continues until light makes another full roundtrip. As the roundtrip time is much longer than the atomic lifetime, the cavity field actually reaches a steady state with $E_{cav}/E_{in} = e^{-OD/2}$ before light reaches the atoms again. No significant intracavity field builds up due to the high optical depth of the ensemble. The dynamics observed for the first roundtrip is consequently the same as in waveguide QED, i.e., when light makes a single-pass through the ensemble. For example, the initial decay of the intracavity field is governed by the collective light-matter coupling of the ensemble with a rate of approximately $(N\beta + (1+\beta))\Gamma_o/2 \approx (OD/4 + 1)/(2\tau_{at})$, see Equation (4.33) with $OD = 4\beta N$ and $\beta \ll 1$. The absorption dynamics

of the light field has the same shape as the emission dynamics that we discussed earlier in Chapter 4.

At $t/t_{\mathrm{rt}} = 2$, light completes its second roundtrip through the cavity and the sharp turn-on of the pulse can be observed again, which after the second interaction with the ensemble now exhibits a decay with a faster timescale than during the first roundtrip. This can be attributed to the fact that the light that reaches the atoms at the second roundtrip has already interacted with the same ensemble during the previous roundtrip. So instead of the step function that excited the ensemble in the first roundtrip, the ensemble is now driven by a pulse in the shape of the dynamics of the first roundtrip. Accordingly, from the perspective of waveguide QED, the observed behavior corresponds to that of a single pass through an ensemble with twice the optical depth. After m roundtrips, the intracavity dynamics are essentially equivalent to a single pass through an ensemble with a total optical depth $\mathrm{OD}_{\mathrm{tot}} = m \times \mathrm{OD}$, see als Section 3.4. This situation of providing delayed coherent feedback to the atoms is also referred to as atom interaction with a non-Markovian reservoir, and we refer to the repeated absorption dynamics as non-Markovian dynamics or features.

The temporal dynamics in the transmission signal in Figure 5.4(h) results from the interference between the outcoupled intracavity field and the light that remains in the coupling fiber. Due to the π-phase shift resulting from the cavity resonance condition, the signal shows thus an inverted behavior compared to the intracavity field.

5.2.3 Few-Mode Cavity QED Regime

Finally, we investigate the behavior of the ensemble–cavity system in the few-mode cavity QED regime shown in Figures 5.4(d) – 5.4(f). We reached this regime by using a resonator length of 5.8 m, where $t_{\mathrm{rt}} = 28.3\,\mathrm{ns} \approx \tau_{\mathrm{at}} = 30.4\,\mathrm{ns}$. For the measurements we chose an optical depth of OD = 6.6.

The frequency response of the system in Figure 5.4(d) is very similar to the predictions of the Tavis-Cummings model. This seems to suggest that the multi-mode nature of light-matter coupling is not relevant as for this situation the adjacent resonances are only modestly shifted outwards. The splitting of the central resonance is well described by the single-mode Tavis-Cummings model, although the steady-state transmission for resonant excitation is not accurately predicted as the additional cavity modes are not included in the model. The cascaded interaction model, on the other hand, again matches very well with the measured data.

The time domain response of the system in Figure 5.4(e) reveals further insights into the dynamics of the system and shows a remarkably intricate dynamics. We find that conventional Rabi oscillations are overlaid with the single-pass or non-Markovian dynamics, indicating that the system shows cavity QED and waveguide QED features at the same time in this regime. The envelope of the signal resembles Rabi oscillations with a frequency that matches the predictions by the Tavis-Cummings model, although the steady state value is slightly too large. Overall, the predictions of the cascaded interaction model align closely with the observed data, with minor deviations that may be attributed to inhomogenous broadening of the atomic ensemble, due to the proximity of the atoms to the nanofiber surface or non-homogeneous magnetic fields from the MOT coils.

To explain the complex behavior in the time domain, it is again best to examine the time evolution of the intracavity field in Figure 5.4(f). The initial dynamics resemble those of the multi-mode regime that we discussed before, where the rapid turn-on of the cavity field at $t/t_{\mathrm{rt}} = 1$ is succeeded by a collective decay due to atomic absorption. However, in the few-mode cavity QED regime, the roundtrip time is now much shorter than for the multi-mode case, preventing the ensemble from reaching a steady state before light completes its first roundtrip. Therefore, there is still atomic excitation left in the atoms when light from the second roundtrip reaches the ensemble. On resonance, the phase condition is such that this results in constructive interference, leading to Rabi oscillations similar to the single-mode case depicted in Figure 5.4(c). However, the cavity is still long enough that the atoms absorb a significant amount of light during one roundtrip. As a result, the cavity response is not instantaneous which causes the non-Markovian features to appear together with the Rabi oscillations.

5.3 INFLUENCE OF THE SYSTEM PARAMETERS

In order to choose a resonator length for our experiment that allows to clearly see the features of the few-mode cavity QED regime, we calculated the expected dynamics for a range of different settings. Interestingly, the dynamics of the system remain qualitatively consistent across a broad range of system parameters. Figure 5.5 illustrates the robustness of the previously observed features by showing theoretical predictions of the cascaded interaction models for a 10-times lower loss rate, a 2.3-times larger optical depth, and a 50% shorter resonator. For comparison, we also include the predictions of the Tavis-Cummings model.

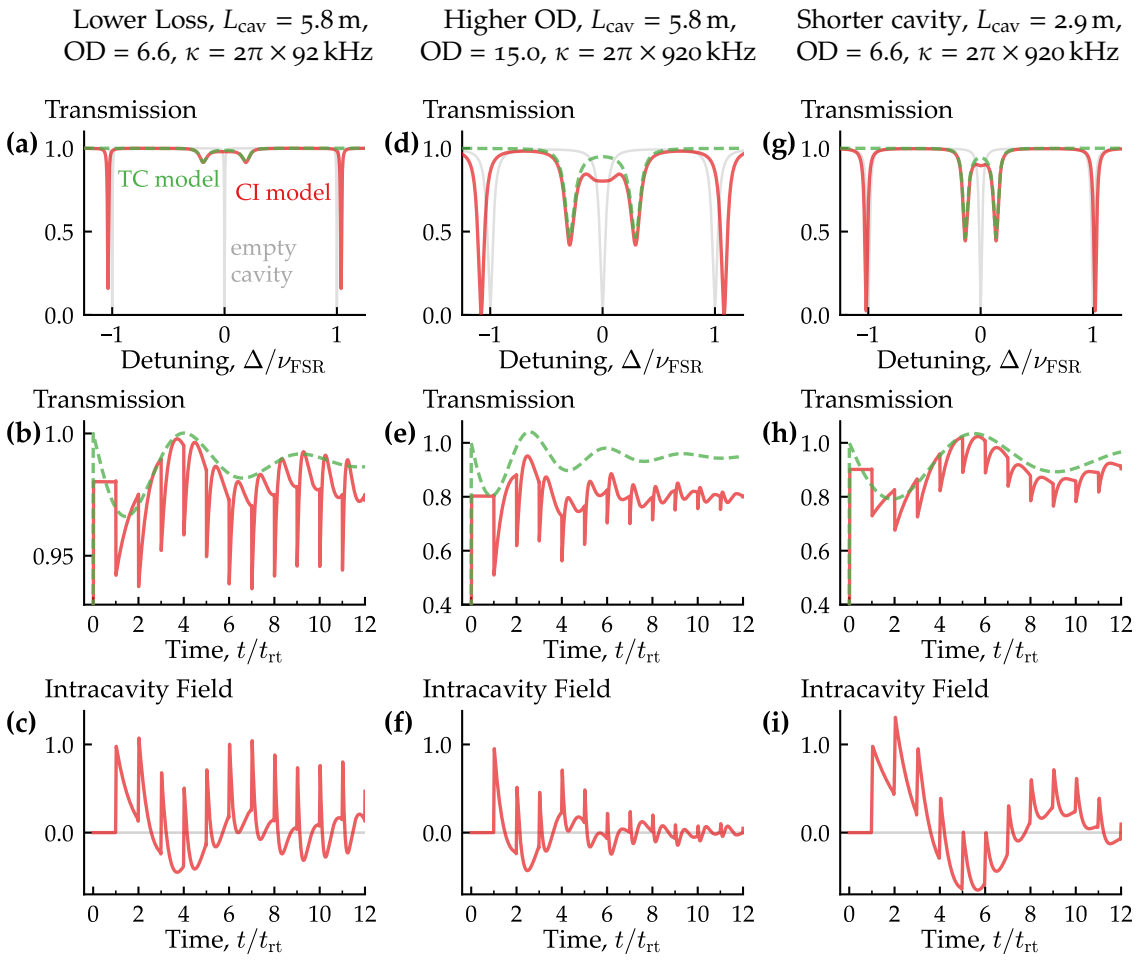

Figure 5.5: Calculated responses of an ensemble–cavity system in the few-mode cavity QED regime for three parameter sets with **(a, b, c)** a lower total cavity loss rate, κ, **(d, e, f)** a higher OD, and **(g, h, i)** a shorter cavity length, L_{cav}, compared to the experimental situation in Figures 5.4(d) – 5.4(f). The calculations with atoms are shown using the cascaded interaction (CI) model (red solid lines) and the Tavis-Cummings (TC) model (green dashed lines), alongside the empty cavity spectra calculated using the CI model (gray lines). No qualitative difference in the dynamics are observed when changing these parameters. t_{rt}: resonator roundtrip time, τ_{at}: natural lifetime of emitters, Δ: laser-cavity detuning, ν_{FSR}: resonator free spectral range.

Figures 5.5(a) – 5.5(c) show the results for a resonator with significantly lower loss, where κ is decreased by a factor of ten from our experimental value $\kappa = 2\pi \times 920$ kHz to $\kappa = 2\pi \times 92$ kHz while keeping the coupling conditions similar to the experimental situation in Figures 5.4(d) – 5.4(f). In the frequency domain, the linewidth of the resonances is thus much narrower in this configuration. In the time domain, essentially the same behavior is observed as in our experiment. The main difference is that the single-pass dynamics exhibits a slower decay and can be observed over many more roundtrips.

The second case that we study is the case of an ensemble with a higher optical depth of OD = 15, depicted in Figures 5.5(d) – 5.5(f). The higher optical depth results in a larger splitting of the central cavity resonance in the frequency spectrum in Figure 5.5(d). In the temporal dynamics in Figure 5.5(e) and the intracavity field in Figure 5.5(f), we observe that the frequency of the overlaying Rabi oscillations is higher compared to Figures 5.4(e) and 5.4(f). This is due to the increased ensemble–cavity coupling rate $g \propto \sqrt{\mathrm{OD}}$, while the loss rates κ and Γ_0 remain the same. As expected, the initial decay rate of the non-Markovian features also becomes faster with increasing OD. Nevertheless, the main property that characterizes the few-mode cavity QED regime, i.e., the co-existence of Rabi oscillations and non-Markovian dynamics, remains again qualitatively unchanged. The parameters in this case are actually reachable in our system, but the non-Markovian features become so fast that they exceed the time resolution of our photon counting system of $\approx 1\,\mathrm{ns}$, especially at higher roundtrip counts where the dynamics are even faster. Thus, we did not investigate this regime experimentally.

Finally, the effects of halving the resonator length to 2.9 m are shown in Figures 5.5(g) – 5.5(i). This modification primarily influences the relative amplitudes of the vacuum Rabi oscillations and the non-Markovian features. For instance, examining the temporal dynamics in Figure 5.5(h) and the intracavity field in Figure 5.5(i), we observe that the shorter roundtrip time interrupts the absorption process earlier, which causes a greater overlap of the non-Markovian features. This also allows for a larger intracavity field to build up, leading to more pronounced Rabi oscillations. Nonetheless, the overall system behavior remains qualitatively similar to our experiment. Further shortening of the cavity would increase the overlap of non-Markovian features progressively until the dynamics resemble those typical of a standard single-mode cavity QED scenario, where the cavity response is instantaneous and is characterized solely by Rabi oscillations.

5.4 MEASUREMENTS WITH DETUNED LIGHT

Another aspect that we investigated is the behavior of the system when it is probed not in the central cavity resonance, but in adjacent ones, which shows complex dynamics that are well predicted with our theoretical model. For this measurement, we set our system to the multi-mode cavity QED regime using a cavity length $L_{\mathrm{cav}} = 45.4\,\mathrm{m}$. We probe the system such that the probe laser field is tuned to the outwards-shifted resonances in the presence of atoms, as illustrated

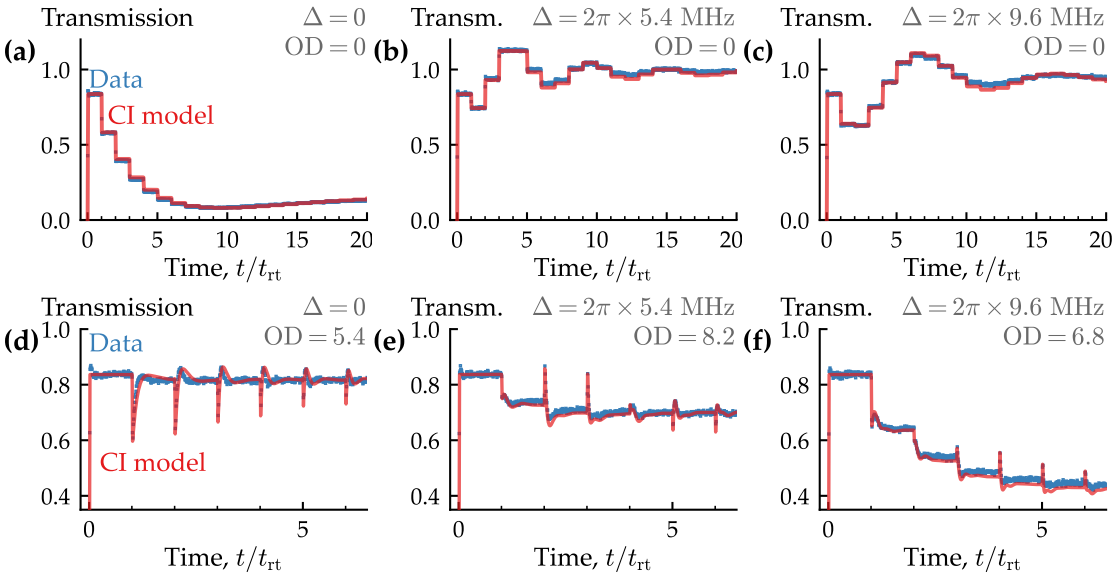

Figure 5.6: Temporal dynamics of the cavity response in the multi-mode cavity QED system with $L_{cav} = 45.4\,\mathrm{m}$ when the probe laser field is detuned from the atomic transition and tuned to the shifted cavity resonances at a detuning of $\Delta = 0,\ 2\pi \times 5.4\,\mathrm{MHz},\ 2\pi \times 9.6\,\mathrm{MHz}$, as depicted by orange dots in Figure 5.4(g). Experimental data (blue squares) is shown alongside predictions using the cascaded interaction (CI) model. **(a, b, c)** show the empty cavity response for comparison, which displays stepwise reductions in transmission and an oscillatory behavior as light is detuned from the empty cavity resonances. **(d, e, f)** depicts the ensemble–cavity dynamics, which become more complex for detuned light due to an additional phase introduced by the atomic dispersion. The optical depth of the fitted model varies for these measurements, possibly due to fluctuations of dispensed cesium over the measurement time of inhomogeneous broadening.

by orange dots in Figure 5.4(g), but here for an ensemble with OD = 5.4. For this optical depth, this corresponds to detunings of $\Delta = 2\pi \times 5.4\,\mathrm{MHz}$ and $\Delta = 2\pi \times 9.4\,\mathrm{MHz}$.

Figure 5.6(a) shows the measured response for the empty cavity and the corresponding fit with the cascaded interaction model for a detuning of $\Delta = 0$. This is essentially the same measurement as previously presented and discussed in Figure 5.3(c), but with a slightly different setting of the tunable fiber coupler. Figures 5.6(b) and 5.6(c) then depict the transmitted power in the detuned cases for the empty cavity. Interestingly, the transmitted power shows an oscillatory behavior, which occurs because the probe light is detuned from the cavity resonances and light accumulates an additional phase during a roundtrip [105]. The detunings in these measurements were chosen such that they are tuned to the shifted cavity resonances in the presence of atoms. Since no atoms are present in this measurement, the light is detuned from the empty cavity resonances. In the measurement shown in Figure 5.6(b), the detuning of the light from the closest cavity mode is $\delta = \Delta - 1 \times \omega_{FSR} = 2\pi \times (5.4\,\mathrm{MHz} - 4.55\,\mathrm{MHz}) = 2\pi \times 0.85\,\mathrm{MHz}$.

This corresponds to an oscillation period of $2\pi/\delta = 1.17\,\mu s = 5.35 \times t_{rt}$ which is consistent with the behavior observed in the plot. For Figure 5.6(c), the relative detuning to the nearest cavity resonance is smaller and the oscillation period here is $9.1 \times t_{rt}$, which also aligns with the observed behavior.

Next, we examine the system's behavior with these detunings, but in the presence of atoms. Figure 5.6(d) is again qualitatively the same measurement as in Figure 5.4(h), which shows repeated non-Markovian features. In the detuned measurements in Figures 5.6(e) and 5.6(f) comparable repeating dynamics appear as before. However, as the ensemble–cavity system is now probed at the combined resonance, we observe a reduction in the overall transmitted power with time due to a build up of a cavity field.

The cascaded interaction model reproduces the observed behavior very well and even subtle features match the predictions.

5.5 SUMMARY AND CONCLUSIONS

In conclusion, this chapter presented a detailed study of the change of the dynamics in cavity QED as atoms are coupled to cavities with increasing length. We showed calculations and measurements in three regimes of cavity QED, the conventional single-mode cavity QED regime ($t_{rt} \ll \tau_{at}$), the few-mode cavity QED regime ($t_{rt} \approx \tau_{at}$), and the multi-mode cavity QED regime ($t_{rt} \gg \tau_{at}$).

As the cavity length increases, we observed that the Rabi oscillations typical for cavity QED disappear and are progressively replaced by non-Markovian features. The cavity length, or more precisely the cavity roundtrip time, determines how much time the dynamics of the atomic ensemble has to develop before the light that already interacted with the atoms returns to the ensemble. In the single-mode cavity QED regime ($t_{rt} \ll \tau_{at}$), the atomic absorption happens on a timescale much longer than this cavity response time. Therefore, a cavity field builds up, which exchanges energy with the atomic ensemble and leads to Rabi oscillations. In contrast, in the multi-mode cavity QED regime ($t_{rt} \gg \tau_{at}$), atoms have sufficient time to reach a steady state before light completes a roundtrip through the cavity. When light returns to the atoms after a roundtrip, these dynamics repeat, but now happen on a faster time scale. As discussed in Section 3.4, the dynamics during a single roundtrip is the same as single-pass waveguide QED dynamics where the optical depth increases each roundtrip. In this configuration, the cavity acts as a non-Markovian reservoir. In the few-mode cavity QED regime ($t_{rt} \approx \tau_{at}$), the ensemble has enough

time to show the onset of a single-pass dynamics, but not enough to reach its steady state before light finishes a roundtrip. Therefore, a cavity field builds up over time. In the few-mode cavity QED regime, we thus observed non-Markovian dynamics superimposed with Rabi oscillations.

The three regimes examined in this chapter provide a comprehensive picture of potential scenarios in cavity QED for cavities with no higher order transverse modes. The observed dynamics were shown to be consistent across a large range of experimental parameters. To observe the described dynamics in our cold atom system, we used unusually long cavities. For quantum emitters with larger intrinsic linewidths, these effects can become significant with much shorter resonators. As an example, quantum dots exhibit radiative lifetimes ranging from 100 ps to 1 ns [33]. Consequently, in such systems, multi-mode features can already be observed for resonators that are only a few millimeters long.

6 TRAPPING ATOMS

Building a nanofiber-based interface between light and neutral atoms trapped close to a nanofiber was an important milestone in the history of our group [41]. The traps are realized in the evanescent field around a nanofiber using a standing wave generated by two counter-propagating laser fields that are red-detuned from the atomic resonance and a blue-detuned running wave. Together, these form a lattice of optical dipole traps along the nanofiber waist. These two-color optical dipole traps are based on the concept of atomic traps in the evanescent field of a dielectric medium introduced by Ovchinnikov et al. in 1991 [106] which has been adapted for nanofibers by Le Kien et al. in 2004 [107] and first realized experimentally by our group in 2010 [41]. Since then, trapping of neutral atoms around a nanofiber has been successfully achieved in multiple experiments within our group and also in other groups around the world [103, 108–111].

In the previous experiments in this thesis, atoms were not trapped. Instead, a cold atom cloud was overlapped with the nanofiber and atoms were interfaced as they freely passed through the evanescent field of the nanofiber. Trapping the atoms, however, can enhance the coupling between atoms and probe light, and increase our experimental toolkit, for example, by enabling coherent manipulation of atomic states (see Section 6.3.3).

In our experimental setup, trapping had not been implemented earlier because the presence of the resonator that was part of the setup rendered the implementation of the required configuration of trapping fields challenging. The most pressing issue is the need for specific polarization states in the nanofiber section for three light fields with different wavelengths. Our fiber-ring resonator is highly birefringent with strongly wavelength-dependent eigenpolarizations. Consequently, there are too many degrees of freedom to reliably ensure that these fields can be prepared with the correct polarization in the nanofiber section. In addition, because high laser powers are required for trapping, frequency fluctuations in the laser field cause fluctuations in the intracavity power, leading to instability of the resonator. The goal is therefore to build a resonator that is only resonant for the probe laser field and where trap light only passes through the system once. We plan to build such a resonator using so-called nullcouplers, a type of fiber coupler with wavelength and polarization-dependent

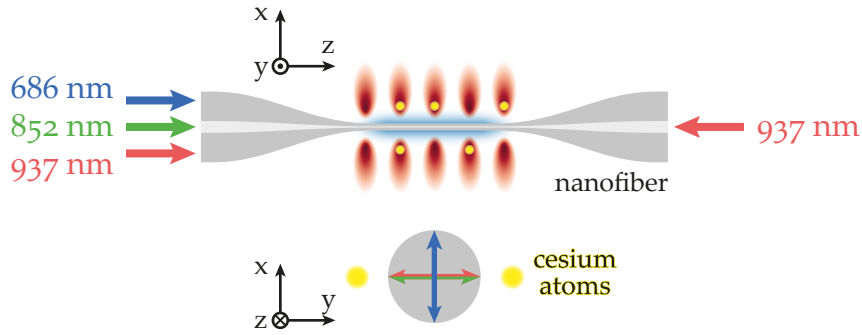

Figure 6.1: A sketch of the light fields that are involved in trapping and probing atoms around a nanofiber. The polarizations of the probe and the red- and blue-detuned laser fields are shown in the cut through the nanofiber waist and cesium atoms are depicted in yellow.

coupling ratio that can be controlled electronically [112]. As a first step towards this system, here we implement traditional trapping without a resonator.

This chapter introduces optical fiber traps and describes the steps needed to update our setup in order to trap atoms. It then covers the optimization and characterization of atom traps, before focusing on the study of the influence of torsional motion of the nanofiber on trapped atoms.

6.1 NANOFIBER-BASED TWO-COLOR OPTICAL DIPOLE TRAP

The standard method to realize optical dipole traps for neutral atoms along a nanofiber is the so-called two-color trapping scheme [41]. This scheme involves creating attractive potentials using a standing wave formed by two counter-propagating, red-detuned laser fields, and a repulsive potential formed by a blue-detuned laser field in a running wave configuration. Figure 6.1 illustrates the light fields and their polarizations that we used to implement such a two-color optical dipole trap. The atoms are probed with a laser field resonant with the D_2-line of cesium at $\lambda_{\text{probe}} = 852\,\text{nm}$. The trapping laser fields are red- and blue-detuned with respect to the D_2 transition of cesium and are near the so-called *magic wavelengths*, for which the scalar light shift is identical for the ground and excited state, which reduces the inhomogeneous broadening due to the trapping fields [108, 113]. The wavelengths we used in our experiment are $\lambda_{\text{red}} = 937\,\text{nm}$ and $\lambda_{\text{blue}} = 686\,\text{nm}$. The polarizations of all light fields are quasi-linear at the nanofiber waist [107] and the red- and the blue-detuned trapping

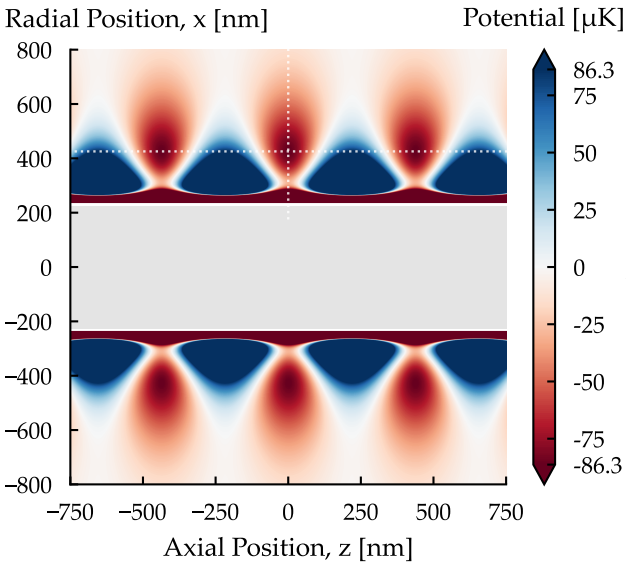

(a) Potential in x-z plane

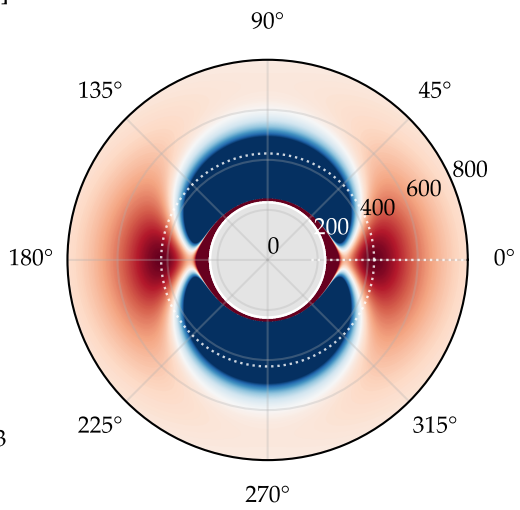

(b) Potential in x-y plane

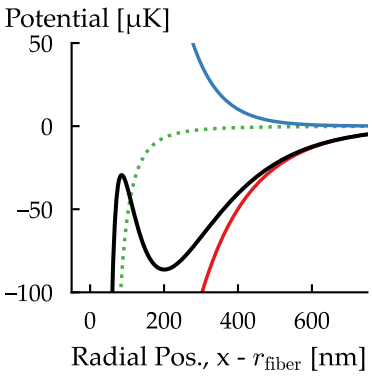

(c) Radial Potential

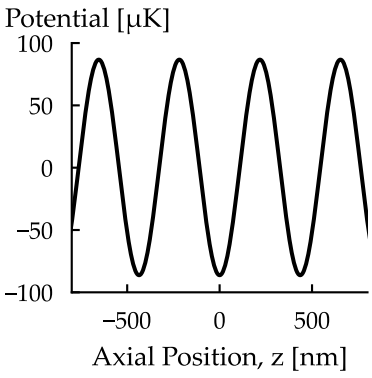

(d) Axial Potential

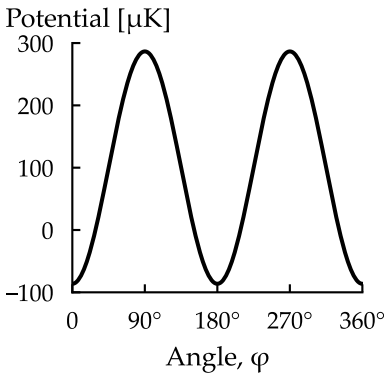

(e) Azimuthal Potential

Figure 6.2: Calculated potentials of the optical dipole traps around a nanofiber for our experimental parameters. The potentials are shown for both **(a)** axial and **(b)** transversal cross-sections through the fiber at $z = 0$ (intensity maximum of the red standing wave). The potential profiles through the trap minimum in **(c)** radial, **(d)** axial and **(e)** azimuthal directions are depicted by dotted lines in the two-dimensional cross-sections.

fields are chosen such that their polarizations are orthogonal to each other. For this configuration, the trap minima where atoms are trapped are along the polarization axis of the red-detuned laser fields. The probe laser polarization is also on this axis to ensure optimal coupling between the probe laser field and the trapped atoms. The trap laser powers were $P_{\text{red}} = 148\,\mu\text{W}$ for each of the two counter-propagting red-detuned laser fields and $P_{\text{blue}} = 13\,\text{mW}$ for the blue-detuned laser field.

Figure 6.2 depicts the resulting potentials for our trap parameters for which we found the longest trap lifetime. Using the radial poten-

tial in Figure 6.2(c), we explain the working principle of the two-color trapping scheme. Far off-resonant, red-detuned laser light leads to an attractive potential for neutral atoms, where the potential depth is proportional to the light's intensity. The atoms therefore experience a force towards the surface of the fiber, where the intensity of red-detuned light is highest. Another attractive potential is the surface potential due to Van-der-Waals interaction of the atoms with the nanofiber surface which scales with the radial position r as $1/(r-a)^3$ with a as the fiber radius. A far-off resonant, blue-detuned light field acts as a repulsive potential that counteracts the two attractive potentials which pull the atoms towards the fiber surface. The evanescent field surrounding a nanofiber decays with decay lengths that are larger for longer wavelengths [107]. By tuning the powers of the red- and blue-detuned laser fields appropriately, a total potential can be formed that is repulsive in the vicinity of the fiber surface and attractive at a larger distance, forming a potential minimum. For our trap parameters, the trap minimum is located about 200 nm from the fiber surface, with a trap depth of $-57\,\mu K$. As atoms enter the trap, they are continuously cooled by the cooling laser fields. If the final temperature is lower than the trap depth, trapping becomes feasible and atoms can be confined within the traps.

In axial direction, the trap potential is shown in Figure 6.2(d) through the trap minimum as depicted by a dotted line in Figure 6.2(a). The confinement of the atoms in this direction is due to the intensity distribution of red-detuned light that is created by the standing wave. The potential has its minimum where the intensity of the red-detuned laser field is highest. The distance between the traps is given by half the wavelength of the red-detuned laser field in the fiber $(\lambda_{red}/n_{eff})/2 = 436\,nm$, with an effective refractive index of the nanofiber waist of $n_{eff} = 1.075$ for $\lambda_{red} = 937\,nm$. The potential in azimuthal direction through the trap minimum is shown in Figure 6.2(e) as indicated by a dotted circle in Figure 6.2(b). Due to the quasi-linear polarization of the laser fields, the intensity of the red-detuned laser fields is highest along the x-direction and the attractive potential is therefore also highest in this direction. The potential is therefore also minimum at angles 0° and 180° in Figure 6.2(e). The blue-detuned laser field is polarized perpendicularly and thus has a repulsive potential that is highest on the y-axis, confining atoms in the azimuthal direction. The atoms oscillate in the formed trapping potentials and we calculate the trap frequencies in radial, azimuthal and axial direction for our trap parameters as $(\omega_r, \omega_\varphi, \omega_z) = 2\pi \times (105.7\,kHz, 80.8\,kHz, 168.8\,kHz)$.

The use of magic wavelengths in our setup mitigates inhomogeneous broadening effects due to light shifts. The energy states of an

atom depend on the intensity of light that it experiences. As atoms move within the trap, they encounter varying light intensities depending on their position in the trap, since the trapping laser fields decay exponentially with distance from the nanofiber surface. Therefore, for finite temperatures of the atoms, this variation results in inhomogeneous broadening of the transition if ground and excited state exhibit different light shifts. The selected wavelengths are then insofar magic as the differential scalar light shift between ground and excited state vanishes for the D_2 transition of cesium ($6S_{1/2}$, $F = 4 \rightarrow 6P_{3/2}$, $F' = 5$), since the scalar polarizabilities of the two states coincide for these wavelengths. While the vector and tensor light shifts are not compensated, their shifts are smaller than the excited state linewidth of cesium for our trap parameters and can thus be neglected [108, 113–115].

6.2 UPDATES TO EXPERIMENTAL SETUP

This section outlines the updates to our experimental setup, including the exchange of our nanofiber and an updated optical setup that combines all nanofiber-guided fields necessary for implementing trapping.

6.2.1 Nanofiber Exchange

To create nanofiber-based optical dipole traps, laser powers on the order of tens of mW need to be launched into the fiber. In our configuration, we launch around 13.3 mW. Due to the nanofiber's small diameter, these powers result in very high peak intensities in the waist ($65\,\mathrm{GW/m^2} = 65\,\mathrm{mW/\mu m^2}$ for our parameters). This calls for very clean fiber surfaces, as even absorbers with very small absorptions can locally heat the nanofiber beyond its melting point, potentially causing fatal damage of the nanofiber.

Unfortunately, the fiber used in the previous chapters could not withstand such high intensities and broke before reaching the required trapping powers. Therefore, we had to exchange the nanofiber, a process which proved to be unusually challenging, requiring six months and thirteen attempts until we could launch high enough powers through the installed fiber. A key factor for the successful exchange was to maintain rigorous cleanliness during the exchange and also of the airflow in the work area.

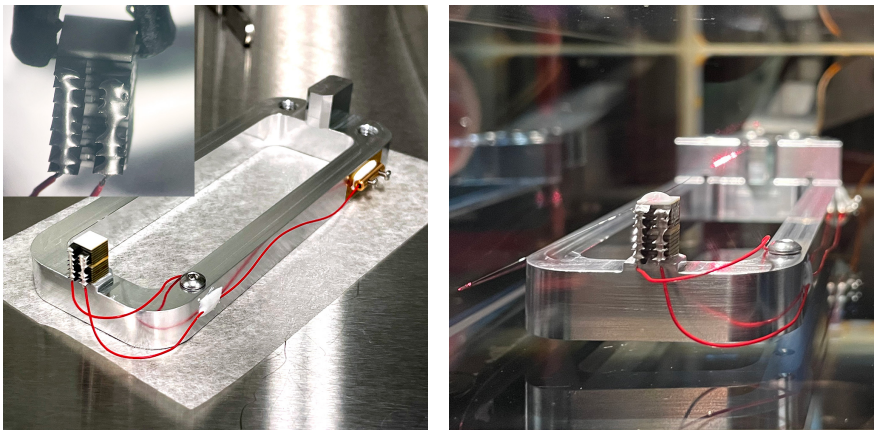

(a) Redesigned fiber holder with piezo

(b) Fiber holder in the setup

Figure 6.3: Photos of the redesigned fiber holder with the attached shear piezo actuator. (a) The fiber holder after fabrication illustrating the connections of the two terminals of the piezo. The inset shows a magnified view of the shear piezo. (b) The fiber holder in its final position within the experimental chamber. The fiber is glued on one side to the shear piezo and on the other side to the holder. The nanofiber can be seen in this picture due to scattering of laser light that is launched through the fiber.

Redesigned Fiber Holder

During the exchange process, we took the opportunity to enhance the experimental capabilities of our setup and added the ability to drive the mechanical motion of the nanofiber. This was achieved by designing a new fiber holder where one end of the tapered optical fiber is attached to a piezo actuator, as depicted in Figure 6.3.

The actuator consists of two shear piezos (Physik Instrumente PI121.03T) that are glued on top of each other using Torr Seal, a low-outgassing vacuum sealant. These piezo actuators are intended for high-vacuum and low temperature environments. Because of the last point, the electrodes are made of tantalum, which has a very low thermal expansion coefficient, but is very hard to solder. Therefore, an electrically conductive epoxy adhesive with a low outgassing rate (Epoxy Technologies H20E) was used to contact the piezo with wires. The inset in Figure 6.3(a) shows the piezo with the wires glued on. To contact the electrodes of the piezo stack, wires were threaded through holes in the electrodes and epoxy glue was added to the wire along each electrode column. However, this method rigidly connected the whole stack, potentially hindering the shear movement of the piezo. If this holder is to be remade in the future, it would be advantageous to connect the wires individually to each electrode rather than along the entire stack, allowing for unhindered horizontal movement. The influ-

ence of the glue on the piezo's movement has not been evaluated, but the piezo movement remained sufficiently functional for our purposes. The wires (Vishay STC-32T-1R) used to contact the piezo are Teflon-coated, ensuring vacuum compatibility. The negative terminal of the piezo is connected to the aluminum holder itself, thereby grounding it to both the chamber and to a pin of an electrical feedthrough. The positive terminal connects to a small wire terminal attached to the side of the holder where it is connected to another pin of the electrical feedthrough.

Nanofiber Diameter

In our updated setup, we have chosen to pull a nanofiber with a nominal waist diameter of 450 nm, slightly larger than the previously used 400 nm. This adjustment aims to improve trapping lifetime by reducing the heating rate due to mechanical motion, which has been predicted to scale inversely with the fiber radius as $R^{-5/2}$ [116]. This approach is supported by a comparison of the two other experiments within our group that trap atoms using a 500-nm-diameter and a 400-nm-diameter fiber, respectively. The initial choice for a smaller fiber diameter was to take advantage of the resulting more intense evanescent fields at the trap position, which could potentially enhance the coupling between probe light and the atoms, i.e., the β factor. However, comparing the experimental results for the two other experiments in our group, we did not observe a significant difference in β between the 400-nm and 500-nm fibers. However, the trapping lifetimes for the 500-nm fiber are higher than for the smaller diameter. To explore the effect of the fiber diameter on the trap performance, we therefore, decided on a fiber diameter of 450 nm, which lies in between the existing parameters.

Process of Exchanging a Nanofiber

After pulling a nanofiber, the transport of the nanofiber from the pulling rig and its installation in the experiment chamber is often associated with additional transmission loss due to pollutants accumulating on the nanofiber. In the worst case, the local heating due to the large intensities in the evanescent field surrounding the fiber that we discussed earlier, can cause the fiber to break. Therefore, it is of utmost importance to maintain a clean environment during a nanofiber exchange.

The setup for our nanofiber exchange with a laminar flowbox above the work area is shown in Figure 6.4(a). To ensure the airflow inside the flowbox was laminar and to prevent dust from being stirred up, we visualized the airflow using a tissue dipped in liquid nitrogen. The

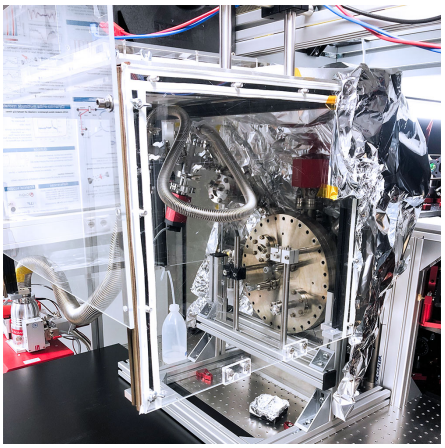

(a) Chamber with scaffold and flowbox

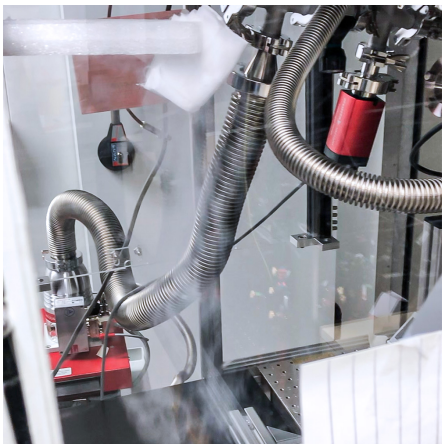

(b) Laminar flow

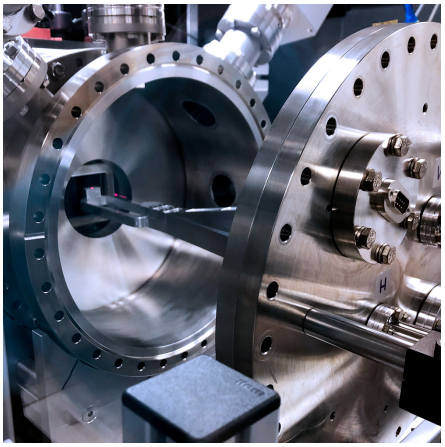

(c) Open chamber with nanofiber

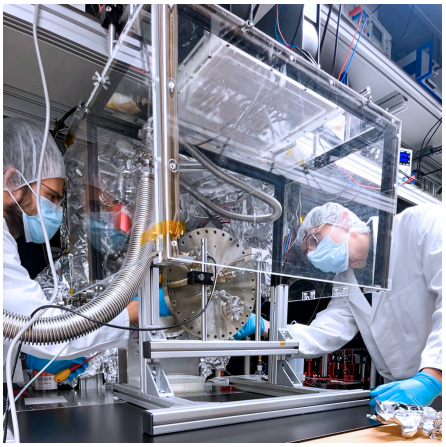

(d) Exchanging the nanofiber

Figure 6.4: Pictures of the setup for exchanging a nanofiber. **(a)** The working area for exchanging the nanofiber with an attached flow box. The large vacuum chamber flange is attached to a scaffold to open it. **(b)** Visualization of flowing air using liquid nitrogen to ensure laminar flow in the flow box. **(c)** The open chamber with an attached nanofiber. **(d)** Another view of the setup during a nanofiber exchange.

cold nitrogen that evaporates from the tissue caused the moisture in the air to condense, making the airflow visible, as shown in Figure 6.4(b). This technique allowed us to determine optimal settings for the strength of the flowbox fans. Additionally, we discovered unfiltered air entering the work area from the sides of the flowbox, which we then sealed with aluminum foil to maintain a clean environment.

After thirteen failed exchange attempts, we found that the culprit was likely an overaged high-efficiency particulate air (HEPA) filter in the flow box. After replacing this filter, the next fiber exchange was successful and the fiber withstood high laser power. We therefore

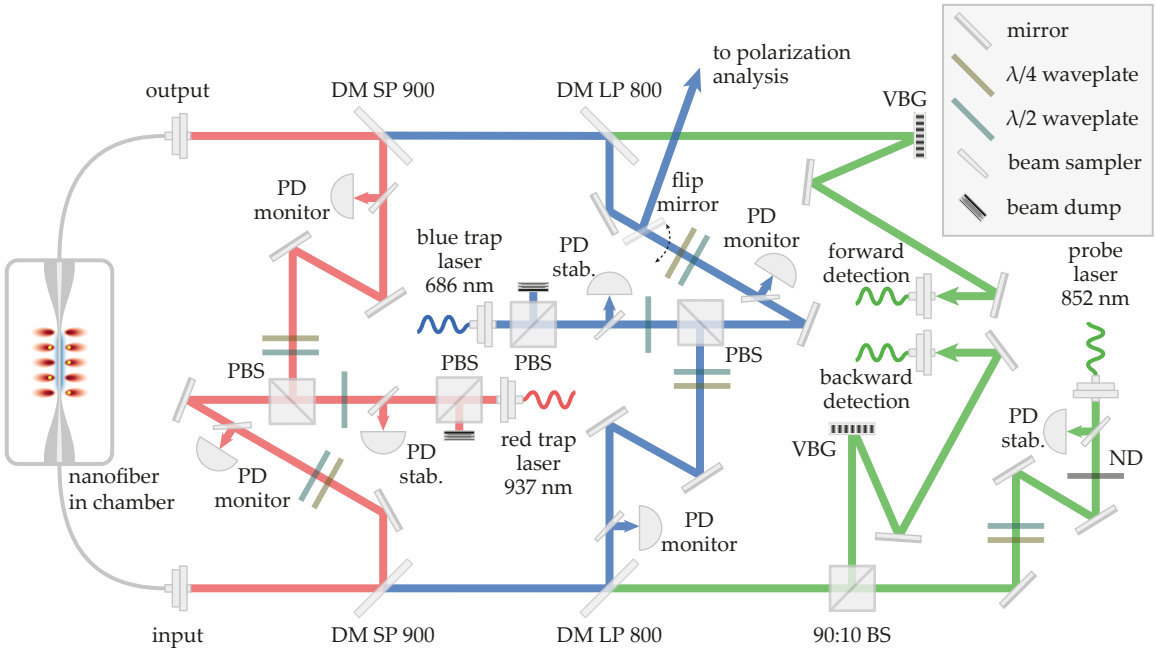

Figure 6.5: The setup combining all fiber-guided light fields for trapping atoms and for detecting transmitted and reflected probe light. PD: photodiode, (P)BS: (polarizing) beam splitter, DM: dichroic mirror, SP 900: short pass filter with 900 nm cut-off wavelength, LP 800: long pass filter with 800 nm cut-off wavelength, VBG: volume Bragg grating, ND: neutral density filter.

conclude that the most important parameter for a successful exchange is clean airflow.

Figure 6.4(c) shows a view inside the open chamber. The large front flange, attached to a scaffold structure, has been pulled out. The photo displays the nanofiber holder, which is attached to a movable arm, and the nanofiber itself, visible due to scattering of the blue-detuned trap laser field. Additionally, Figure 6.4(d) captures a moment during the nanofiber exchange, where Riccardo Pennetta (right) and I can be seen focusing on the delicate task of exchanging a nanofiber.

6.2.2 Updated Setup for Nanofiber-Coupled Light Fields

The setup for in- and outcoupling of fiber-guided light fields that are needed for our experiments with trapped atoms is sketched in Figure 6.5. The setup is designed in a modular fashion, building on our group's experience with atom trapping. Experiments with different trapping configurations can be done without the necessity for realignment, such as changing from a red to a blue standing wave trap, which has a smaller axial distance between the traps but azimuthally shallower traps [117]. Ports for additional fiber-guided laser beams are easy to add via beam splitters.

The design also ensures equal optical path lengths for both arms of the standing waves. When the optical path lengths of the counter-propagating laser fields are equal, any fluctuations in the laser frequency, which affect the spacing of the traps, are centered around the middle of the nanofiber waist. In this case, one half of the traps shift to the left and the other half shift to the right as they move outwards. The further a trap is from the center of the interference pattern, the larger the overall shift. However, if the path lengths are not equal, the point of equal path length is outside the nanofiber waist and eventually far away from it. Therefore, fluctuations in frequency would translate to large shifts in trap position.

The light fields that are launched through the nanofiber are the red- and blue-detuned trap fields and the probe laser field, with wavelengths $\lambda_{\text{red}} = 937\,\text{nm}$, $\lambda_{\text{blue}} = 686\,\text{nm}$, and $\lambda_{\text{red}} = 852\,\text{nm}$, respectively. The probe laser and the red-detuned trapping laser fields are generated from Toptica DL Pro external cavity diode lasers, while the blue-detuned trapping laser utilizes a tapered amplifier Toptica TA Pro laser system. The light fields are coupled into optical fibers on the laser table and routed to the experiment table in polarizatiton maintaining fibers, where they are intensity stabilized before entering the nanofiber using the signal from a photodiode (PD) that samples a portion of the light, with the PID control being implemented on a Red Pitaya microcontroller.

The polarization of the trap laser fields is first cleaned with a polarizing beam splitter (PBS) before the laser light is split into two arms. The polarization state in each arm can then be adjusted with a $\lambda/2$ and a $\lambda/4$ waveplate, which are manually controlled for the probe and the blue-detuned trap laser fields and computer controlled with motorized rotation mounts (Thorlabs Elliptec ELL14K) for the red-detuned light fields. The polarization state of the light in the nanofiber section is tuned by maximizing or minimizing the power of the light scattered to the side of the nanofiber, which we observe with a camera that is equipped with a linearly polarized filter, achieving visibilities of up to 85% for the red trapping laser fields, up to 75% for the blue trapping laser field and up to 80% for the probe laser field, see [115] for additional details on this method.

The laser fields are combined using dichroic mirrors before they are coupled into the coupling fiber. In our configuration, the probe field and the blue trapping field were launched only from one direction into the fiber.

Probe light transmitted through the nanofiber is detected similarly to the earlier setup using two SPCMs in Hanbury Brown-Twiss configuration. In backward direction, a single SPCM is used. Before light is detected it is spectrally filtered using narrow bandwidth volume

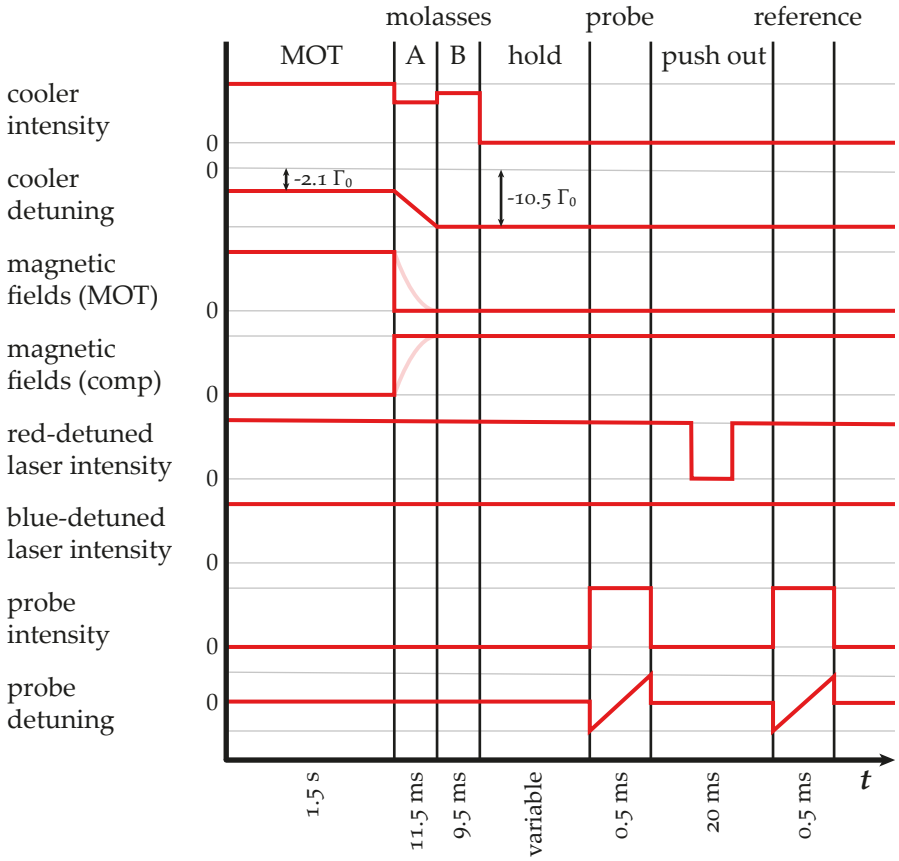

Figure 6.6: Experimental sequence used to trap atoms in our experiment and to measure the optical depth of the trapped ensemble after a variable hold time. A reference measurement is taken after atoms are expelled from the trap by deactivating the red-detuned trap laser fields. Red lines depict the values of the controlled channels and 0 signifies that the channel is turned off. Light red lines highlight the non-negligible time required for magnetic fields to completely switch off.

bragg gratings (VBG) and bandpass filters in order to remove photons from the trapping fields and from Raman scattering of the trapping laser fields. This filtering is now even more important as the powers of the laser fields are much higher than in the configuration before.

6.3 TRAPPING ATOMS

6.3.1 Sequence

The experimental sequence to load and detect atoms in an optical dipole trap is sketched in Figure 6.6. The sequence starts with a MOT phase of 1.5 s, during which atoms are loaded into the MOT. Subsequently, the MOT's magnetic fields are turned off and the system

enters the molasses phase which is divided into molasses phase A and B. In the initial molasses phase A, the magnetic fields are turning off, a process that takes about 10 ms owing to self-induction of the coils, which we indicate in the figure in light red. During this time, we ramp the detuning of the cooler laser fields from the $2.1\Gamma_0$ in the MOT phase to $10.5\Gamma_0$. When the magnetic fields are completely turned off, the system enters the second molasses phase B, during which we just slightly change the cooler intensity and wait for the atoms to be cooled into the dipole trap potential. At the end of molasses B, the cooler is switched off completely. The trap laser fields are kept on the whole time. In order to measure the optical depth after a variable hold time, we sweep the frequency of the probe laser field within 0.5 ms across the atomic resonance and record the transmission through the nanofiber using SPCMs. To normalize this probe scan, a reference measurement without atoms is taken after the atoms are released from the traps by turning off the red-detuned trap laser fields.

6.3.2 Optimization and Characterization of Nanofiber Traps

Creating a nanofiber-based optical dipole trap involves optimization of a large number of experimental parameters such as laser powers, laser detunings, magnetic field strengths, and all the involved timings. In doing so, we arrived at the experimental sequence outlined in the previous section. Simulations and experience from the other experiments in our groups that successfully trap atoms, gave us preliminary settings for selecting the appropriate trapping parameters. However, for the majority of the other parameters, we performed systematic scans of one or more variables and optimized for the optical depth of the ensemble. Once we were trapping the atoms successfully, we fine-tuned the parameters with further scans in order to maximize the trapping lifetime to achieve a stable and long-lived trap.

Molasses

An essential step in trapping atoms around a nanofiber involves creating a cloud of cold atoms that acts as a reservoir for loading atoms into the dipole traps. In our experiment, atoms are first cooled and trapped in a MOT. Then the magnetic fields are switched off, creating an optical molasses with parameters optimized to achieve a lower atomic temperature than during the MOT phase [118]. This enables us to load atoms more reliably into the dipole traps.

To create a molasses, it is necessary to compensate the Earth's magnetic field and other stray magnetic fields. In our setup, compensation coils are employed to compensate these magnetic fields. We used an

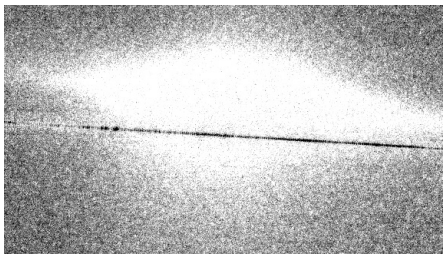

(a) Molasses after 5 ms

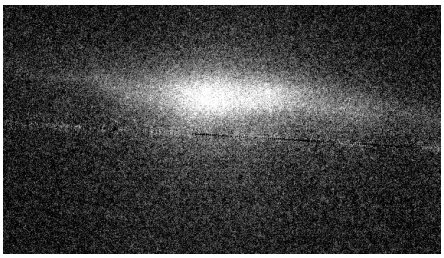

(b) Molasses after 10 ms.

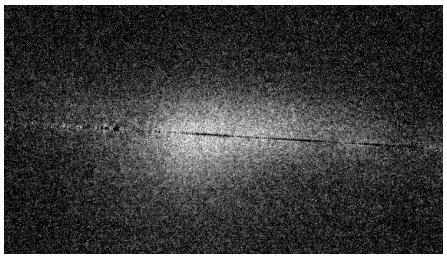

(c) Molasses after 20 ms. Atoms are transferred into the trap around this time.

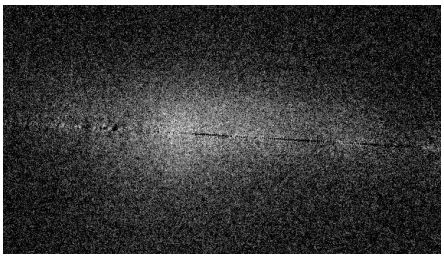

(d) Molasses after 100 ms.

Figure 6.7: Fluorescence images of the cloud of cold atoms during the molasses stage at different times after the magnetic fields of the MOT are turned off. The molasses moves from the MOT position down to overlap with the fiber and remains in this position for more than 100 ms. The power and detuning of the cooling laser fields corresponds to the ones from the experimental sequence.

iterative process to determine the optimal settings for the compensation coils. We turned off the MOT coils and used a camera to monitor the direction in which the cold atom cloud was moving. The currents in the compensation coils were then adjusted until the cloud remained stationary after switching off the MOT.

Figure 6.7 shows images of the cold atom cloud for different times after turning off the MOT coils. The images were captured by a camera that observes the fiber from the side. A background image without the atom cloud was subtracted to remove the scattering of light from the nanofiber waist. Initially, after the MOT coils are turned off, the cold atom cloud is above the nanofiber within 10 ms (see Figures 6.7(a) and 6.7(b)), which is the time it takes for the MOT coils to switch off. The cloud then moves to its final position where it overlaps with the nanofiber (see Figures 6.7(c) and 6.7(d)). The atoms are loaded into the nanofiber traps during the molasses B phase which ends at about 20 ms as shown in Figure 6.7(c). An additional image of the molasses after 100 ms shown in Figure 6.7(d) demonstrates the molasses remaining stationary for long times. The position change of the atom cloud between the MOT and the molasses phase is not fully

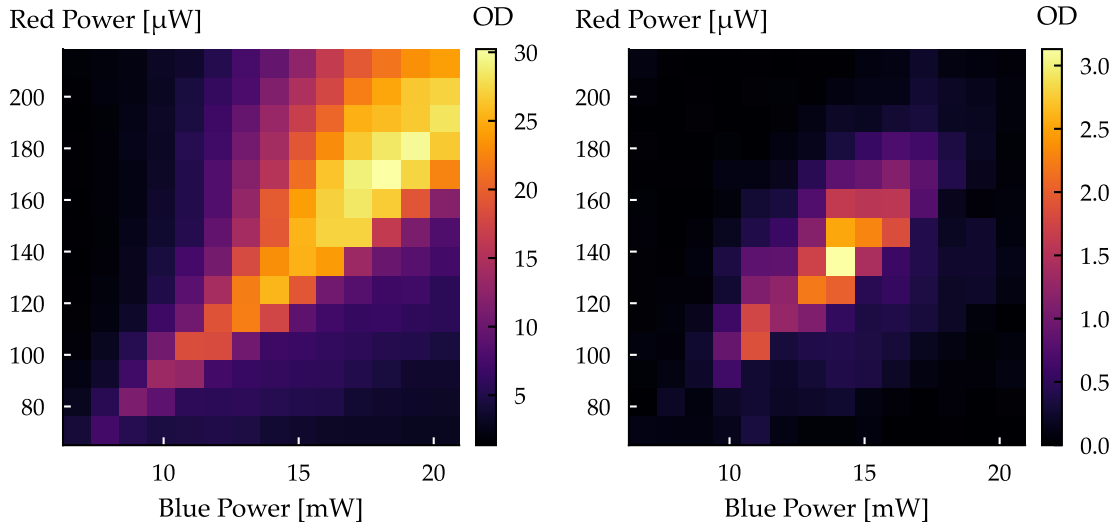

(a) OD after 0 ms

(b) OD after 50 ms

Figure 6.8: A two-dimensional scan of the trapping powers measured after **(a)** 0 ms and **(b)** 50 ms after the cooler laser fields are turned off shows that the parameters suitable for enabling long trap lifetime might be different from those for enabling high initial optical depths.

understood. However, this configuration yielded the highest number of nanofiber-coupled atoms in our experiments. We speculate that it is advantageous to load the MOT away from the nanofiber as we have observed a MOT's brightness to reduce when overlapping it with the nanofiber, likely due to atoms colliding with the fiber surface.

Trapping Powers

To maximize the number of trapped atoms, we optimized multiple parameters, including the laser powers of the trapping fields. As we are targeting long lifetimes, we optimize the parameters for achieving a high optical depth after a long hold time. Figure 6.8 shows a typical two-dimensional scan, where we measured the optical depth of the atomic ensemble for different powers of the red- and blue-detuned laser fields immediately after switching off the cooler laser fields (Figure 6.8(a)) and after a hold time of 50 ms (Figure 6.8(b)). While in Figure 6.8(a), the maximum optical depth is reached for relatively high laser powers, the maximum after 50 ms is actually reached for lower powers, showing that the configuration with the highest initial optical depth is not necessarily the one that yields the longest lifetimes. After further optimization, the trapping powers that gave the best lifetime and which were used in the experiments were $P_{\mathrm{red}} = 148\,\mu\mathrm{W}$ in each arm and $P_{\mathrm{blue}} = 13\,\mathrm{mW}$.

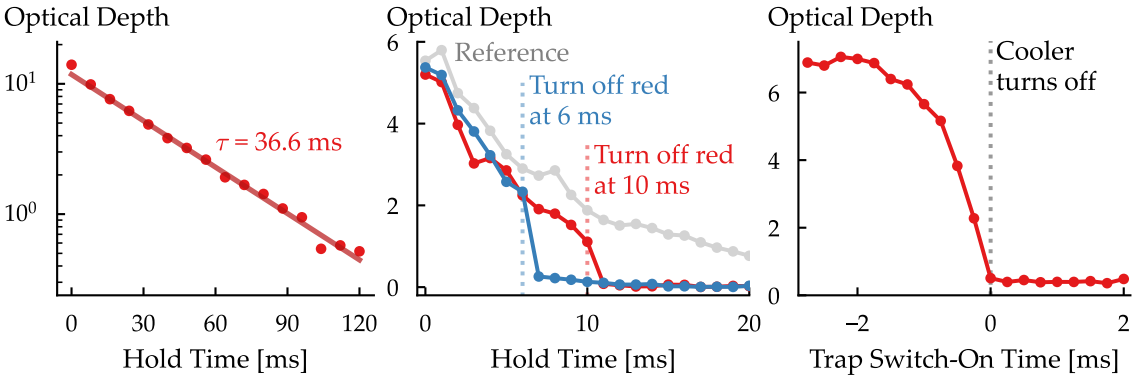

(a) Trap lifetime **(b)** Loss of atoms **(c)** Loading time traps

Figure 6.9: (a) Measurement of the optical depth for increasing hold time. From an exponential fit of the data, we extract a lifetime of $\tau = 36.6$ ms. **(b)** The same measurement, but the red-detuned trapping laser field is temporarily turned off for 100 µs. The loss of atoms from the trap is evidence for successful trapping of atoms. **(c)** The optical depth for varying switch-on times of the red-detuned trap laser field. From this, we can estimate a minimum loading time of our nanofiber traps of approximately 2 ms

Trap Lifetime

Figure 6.9(a) shows a measurement of the number of atoms in the traps as a function of hold time for the optimal trap parameters from the previous section. Fitting an exponential decay to the measured data, we obtain a $1/e$ trap lifetime of $\tau = 36.6$ ms. The first two experimental points at 0 and 8 ms are excluded in the fitting because at these times there are still untrapped atoms from the molasses around the nanofiber, introducing an offset to the data.

To verify that the measured absorption signal originates from trapped atoms rather than atoms from the background cloud of cold atoms, we present a measurement of the optical depth for increasing hold times in Figure 6.9(b). In this experiment, we briefly switch off the red-detuned trap laser fields for 100 µs after 6 ms and 10 ms. In both cases, the measured OD drops sharply, confirming that the atoms were indeed trapped in the dipole traps.

Loading Time into Traps

Another important parameter for our experiment is the timescale required to load atoms from the molasses into the dipole traps. To measure this, we switch on the red-detuned trapping laser fields at variable time delays before the end of the molasses phase, i.e., before the cooler laser field turns off. The blue trap laser field remains on continuously. The optical depth of the trapped ensemble is then measured after a hold time of 15 ms. Figure 6.9(c) shows the resulting optical depth as a function of the switch-on time of the red trap laser.

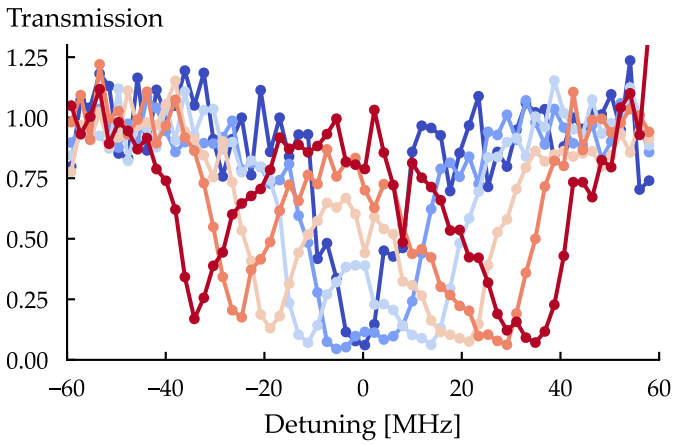

Figure 6.10: Transmission spectra for an ensemble prepared by applying a linearly increasing magnetic field and pumping the ensemble with a probe field. Due to the circular polarizations in the evanescent field of the nanofiber, the ensembles on either side of the nanofiber are pumped into the outer $m_F = \pm 4$ states. As the magnetic field increases, the larger Zeeman shift causes the absorption dips to split apart. From these spectra, we extract magnetic field strengths ranging from 0 G to 24 G.

Activating the dipole traps more than 2 ms prior to the deactivation of the cooler laser fields does not have an impact on the final optical depth. However, the optical depth decreases noticeably when the red laser fields are turned on closer to the end of the molasses B phase. Turning on the trap laser fields after the cooler has already been deactivated results in zero optical depth. Based on these observations, we deduce a loading time of the dipole traps of about 2 ms.

6.3.3 State Preparation

Atoms trapped in nanofiber-based optical dipole traps interestingly experience different probe field polarizations on the two sides of the fiber. Due to the strong field gradients, the evanescent field surrounding the nanofiber exhibits a significant longitudinal field component. As this component is $\pi/2$-phase-shifted with respect to the transverse polarization component, the local polarization in the evanescent field can have nearly perfectly circular polarization. Consequently, the light fields in the evanescent field are σ^+-polarized on one side and σ^--polarized on the other side. Here σ^+ and σ^- are defined with respect to a quantization axis that is oriented perpendicularly to the nanofiber axis and to the transverse polarization component of the probe light [119]. An external magnetic field parallel to this quantization axis induces a Zeeman shift in the m_F levels of the atoms. Atoms that are excited by the fiber-guided, circularly polarized $\sigma^\pm$ light fields

are pumped into the outermost m_F states due to selection rules. On one side they are prepared into the $m_F = 4$ state, while those on the opposite side are prepared into the $m_F = -4$ state [120].

To pump atoms into these states, we apply a bias field with our compensation coils to shift the m_F states. We then prepare the ensemble by sweeping the probe laser field across the atomic resonance. This way, the ensembles on both sides of the fiber are pumped into different states. We then probe the ensemble by scanning the probe laser field across resonance.

Figure 6.10 shows the resulting transmission spectra of the ensemble for increasing applied magnetic fields. The cycling transitions for $m_F = -4$ to $m_F = -5$, and $m_F = 4$ to $m_F = 5$ have different transition frequencies due to different Zeeman shifts. As a result, we observe two absorption dips in this measurement that belong to the two subensembles on the two sides of the fiber. The dips split apart linearly with the increasing magnetic field strength as the Zeeman shift becomes larger. From this measurement and based on the knowledge of the Zeeman shift of the individual levels, the magnetic field strengths can be extracted, which range from 0 G to 24 G [87].

These measurements show our capability to replicate the results of [120] and manipulate the internal state of the atoms which we can prepare in specific states, which opens up new possibilities in our experimental toolbox.

6.4 INFLUENCE OF TORSIONAL MOTION OF THE NANOFIBER ON TRAPPED ATOMS

Heating induced by the mechanical motion of a nanofiber has been hypothesized to significantly affect the lifetime of atoms trapped in evanescent two-color standing wave traps. The new design of our nanofiber holder allows us for the first time to directly study the influence of the mechanical modes on the trapped atoms via controlled excitation of individual modes. This section focuses on the influence of the torsional mode of the nanofiber on the trapping performance. Since the torsional oscillation couples to the polarization of the trapping light fields via the strain-optical effect, it has been hypothesized to influence the lifetime of trapped atoms due to the proximity of the torsional mode frequency to the trap frequencies of atoms in the trap [116, 121].

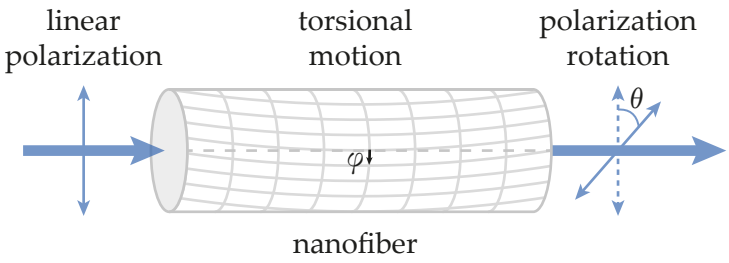

Figure 6.11: The displacement φ of the nanofiber waist around its axis due to torsional motion causes a rotation θ of the (linear) polarization of transmitted light due to linear birefringence of the nanofiber caused by its slightly elliptical cross section.

6.4.1 Mechanical Modes of a Nanofiber

The nanofiber section of the tapered optical fiber supports several mechanical eigenmodes, for example, the longitudinal, flexural and torsional modes [116, 121, 122]. Longitudinal motion involves periodic compression along the fiber's length, potentially accompanied by a breathing motion that alters the fiber radius due to the Poisson effect. Flexural modes, also sometimes called string modes, are transverse oscillations of the fiber. Finally, torsional modes are rotations of the nanofiber about its axis.

The taper geometry of an optical nanofiber can act as a reflector for certain mechanical modes giving rise to standing waves that are localized in the taper region, while other modes may propagate through the taper, delocalizing them along the entire fiber [121]. The mechanical motion of nanofibers can be damped in different ways, including losses attributed to the clamping of the fiber [123], friction with a background gas [121, 124], losses within the material [125] and losses on its surface [126].

Of particular interest are torsional modes in nanofibers which can have very high quality (Q) factors of up to 10^7 [124]. The fundamental torsional mode and the second order torsional mode are localized predominantly along the nanofiber waist, while higher order modes above a certain geometry-dependent cutoff frequency penetrate deeper into the taper region, resulting in modes that extend into the taper as well [121].

Figure 6.11 depicts the displacement due to the fundamental torsional motion of a nanofiber waist, represented here as a cylinder. In this mode, the nanofiber undergoes periodic rotation around its axis, accompanied by a displacement denoted by the angle φ in its center where we assume that the nanofiber is clamped on both sides.

The nanofibers we use exhibit birefringence, which we believe results from a slight ellipticity of their cross sections due to the pulling process. As a consequence, different quasi-linear polarization components of light transmitted through the fiber experience different phase shifts. When the fiber oscillates around its axis, the displacement φ of the fiber leads to a change of the orientation of the fast and slow axes, which causes a corresponding change in the polarization direction θ of the output light. This makes it possible to measure the fiber displacement by analyzing the change of the output polarization. For more details, refer to [124, 127] where these mechanisms were first described in another experiment conducted by our group.

The dynamics of the torsional motion can be modeled as a driven, damped harmonic oscillator described by its equation of motion [124]

$$\ddot{\varphi} + \gamma\dot{\varphi} + \omega_0^2\varphi = \frac{M_{\mathrm{th}}(t) + M_{\mathrm{ext}}(t)}{I_{\mathrm{eff}}}. \tag{6.43}$$

Here, γ represents the energy damping rate of the oscillation, $\omega_0 = 2\pi f_0$ denotes the resonance frequency of the fundamental torsional mode and I_{eff} is the effective moment of inertia of the nanofiber mode. The driving terms include the thermal torque M_{th} arising from white noise, modeling thermal excitation of the motion due to the fiber's temperature, and an external torque M_{ext} which, in our experiments, is provided by a piezo actuator attached to one end of the nanofiber. However, the exact mechanism by which the motion of the piezo actuator couples to the torsional motion remains unclear.

6.4.2 Experimental Setup

The experimental setup we use to observe, drive and feedback-cool the nanofiber motion is shown in Figure 6.12. It consists of several parts: the nanofiber inside the vacuum chamber with an attached piezo actuator to directly excite the nanofiber motion, two detection setups to measure the polarization fluctuations of the transmitted field, and a Red Pitaya microcontroller to control and drive the piezo.

We use the blue-detuned trapping laser field at 685 nm to probe the nanofiber motion because it is always on and also provides the strongest light field in our experimental setup, thus giving the best signal-to-noise ratio. After passing through the nanofiber, the light is outcoupled and split into two arms with a 50:50 non-polarizing beam splitter (BS) to proceed to the in-loop and out-of-loop polarization detection setups. Since the torsional motion induces changes in the polarization state of light, these fluctuations can be analyzed using a polarization analysis setup consisting of a polarizing beam splitter

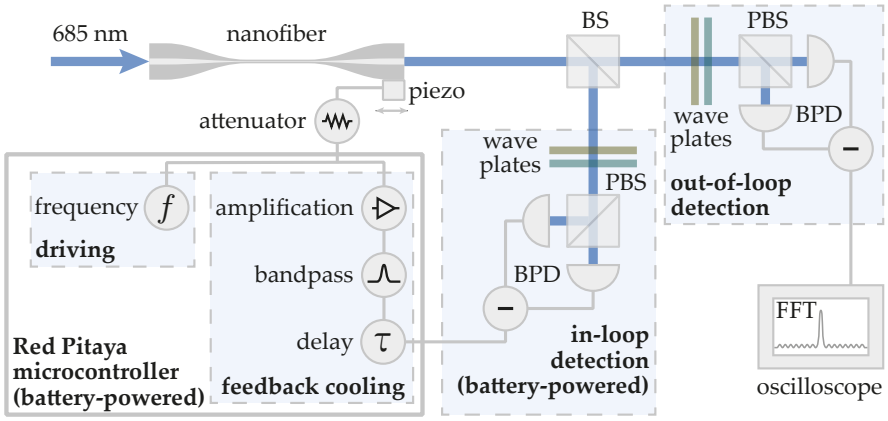

Figure 6.12: The experimental setup used to detect, drive and cool the torsional mode of the nanofiber. An in-loop and an out-of-loop detection setup is employed, consisting of a polarizing beam splitter (PBS) and a balanced photodiode (BPD) to measure the polarization fluctuations of the light transmitted through the nanofiber, which give us a measure of its torsional displacement. The signal acquired with the out-of-loop detection is analyzed on an oscilloscope by a fast Fourier transform (FFT). A Red Pitaya microcontroller is used either to drive the torsional motion directly or to feedback the signal from the in-loop detection to the piezo in order to cool the torsional motion of the nanofiber.

(PBS) and two photodiodes whose signals are subtracted to form a balanced photodiode. Two waveplates ($\lambda/2$ and $\lambda/4$) are used in each detection setup to set the polarization state of light to balance the signals between the two photodiodes, which is the set point with the highest sensitivity to polarization fluctuations. The PBS divides the incident light into its horizontal and vertical polarization components. Fluctuations in the polarization state then lead to a difference signal between the photodiodes, which serves as a measure of the polarization fluctuations and, consequently, of the displacement of the nanofiber due to torsional motion. While a single photodiode would be sufficient to measure these fluctuations, the use of a balanced photodiode couple makes the setup less susceptible to changes in signal due to changes in overall laser power. In this configuration, the difference signal is recorded on an oscilloscope. When the time-domain signal is Fourier-transformed, the resulting power spectral density reveals the spectrum of the fluctuations. A commercial balanced photodiode (Thorlabs PDB450A) is used in the out-of-loop detection setup. For in-loop detection, two battery-powered photodiodes (Thorlabs DET36A2) are used along with a homemade, battery-powered summing amplifier to subtract the signals. A Red Pitaya microcontroller controls the piezo actuator, either to drive it at a specific frequency or to implement feedback cooling of the torsional motion. The microcontroller is also

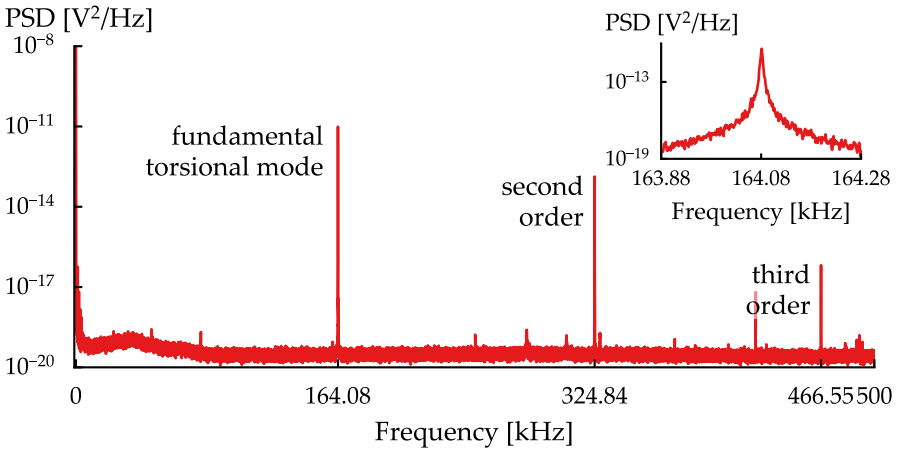

Figure 6.13: Power spectral density (PSD) of the out-of-loop difference signal of the light transmitted through the nanofiber as a function of the mechanical frequency. The prominent peaks correspond to the first three torsional modes of the fiber. The inset shows a magnified view of the fundamental torsional mode.

battery-powered. The reason for using battery-powered devices is an unresolved grounding issue in our lab, which introduces significant noise into the piezo when it is connected to anything in the lab that is grounded. This noise causes the nanofiber to shake uncontrollably, making trapping or other experiments impossible.

The motion of the nanofiber is highly sensitive to the motion of the piezo, meaning that even small voltage changes significantly affect the motion of the nanofiber. Consequently, the inherent output noise of the microcontroller affects the nanofiber motion of the nanofiber. To mitigate this influence, we attenuate the output of the microcontroller by 60 dB before connecting it to the shear piezo. This reduces both the output noise and the signal. By then driving the signal at a high amplitude, we found that a better signal-to-noise ratio can be achieved in comparison to not attenuating the output.

6.4.3 Characterization of the Torsional Mode

Mechanical Spectrum

Figure 6.13 shows the power spectral density (PSD) of the light transmitted through the nanofiber as a function of the mechanical frequency measured with the balanced photodiode setup described in the previous section. A magnified view of the fundamental torsional mode is provided in the inset. The PSD was inferred from the time-domain data using a Fourier transform that follows Welch's method [128]. This method is preferred for calculating PSDs as it more accurately

maintains the signal's power and reduces noise compared to a regular Fourier transform. The optical power launched into the nanofiber was 13 mW for the blue-detuned trapping laser field and 300 µW combined power for the red-detuned trapping laser fields. For these settings, the absorbed optical power is expected to heat the waist to temperatures on the order of 500 K [129]. The time domain signal was recorded for a total of 10 s with a total of 10 million samples, allowing us to resolve frequencies up to 500 kHz. The spectrum exhibits three distinct frequencies that have been identified as the torsional modes of the nanofiber [121]. The frequency of the fundamental torsional mode of this fiber is at 164.08 kHz, with the second and third order torsional mode observed at 324.84 kHz and 466.55 kHz, which agrees well with finite element simulations of the torsional modes of the nanofiber. The spacing between the harmonics is not exactly an integer multiple of the fundamental mode frequency because the nanofiber structure is connected to two taper sections. Higher harmonics above a certain cutoff frequency extend further into the taper geometry, resulting in resonance frequencies that differ from the simple harmonic spectrum of a clamped cylinder [121]. In addition, we found that the resonance frequencies also change as a function of the laser power injected into the fiber. The resulting temperature change in the pre-strained fiber waist causes a change in strain, and thus a change of the resonance frequency of the torsional mode. We observed the fundamental torsional mode frequency to vary by up to 10 kHz for the powers used.

In the subsequent sections, we primarily study the influence of the fundamental torsional mode as its frequency ($\approx$ 164 kHz) is closest to the axial trap frequency of atoms in the trap ($\approx$ 169 kHz) and is therefore most likely to influence the lifetime of the atoms.

Driving the Torsional Mode

Driving the nanofiber's oscillations is achieved by modulating the piezo voltage via a Red Pitaya microcontroller as illustrated in Figure 6.12. An example of the effect of driving of the motion of the nanofiber is shown in Figure 6.14(a). Here the piezo is driven with a sinusoidally varying signal that is slightly off-resonance to the fundamental torsional mode. The exact coupling mechanism between the axial, linear oscillation exerted by the piezo actuator and the torsional oscillation of the nanofiber is not completely understood. It is possible that the nanofiber is attached to the holder at a slight angle or with a minor twist. As a result, the linear force applied by the piezo actuator may be converted into a rotational torque. Additionally, material anisotropy resulting from the drawing process might also contribute to the coupling. Initially, we assumed that the torsional mode would have to be

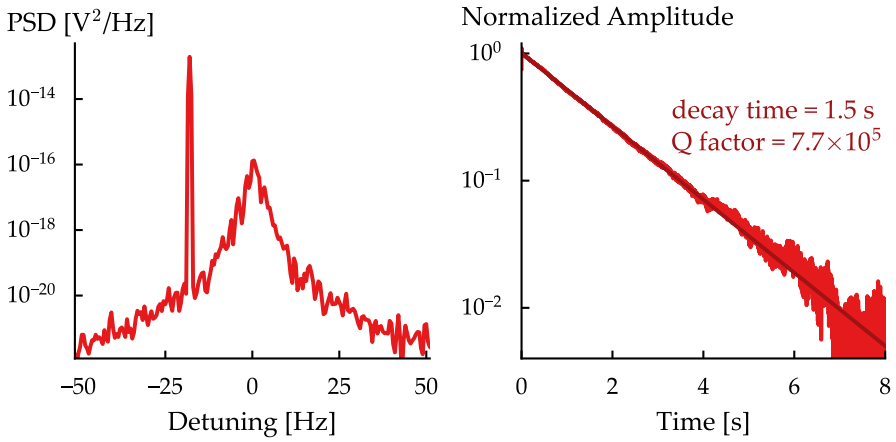

(a) Driving the torsional mode **(b)** Ringdown measurement

Figure 6.14: (a) Measured PSD of the transmitted light when driving the fundamental torsional mode of the nanofiber externally with a sinusoidal signal that is slightly detuned from resonance. **(b)** Ringdown measurement of the fundamental torsional mode excited on resonance. The data (light red curve) shows the time evolution of the oscillation amplitude of the torsional motion. The amplitude of the band-pass filtered signal is fit with an exponential decay (dark red line), which results in a decay time of 1.5 s and a resulting Q factor of 7.7×10^5.

driven parametrically at double the resonance frequency. But in our system, we only clearly observed resonant driving of the mode.

Q Factor

The Q factor, which characterizes a resonator's energy loss, is typically inferred from the width of the Lorentzian lineshape in the spectrum. In our experiment, the torsional mode resonance, which exhibits a linewidth of ≈ 1 Hz, drifts by several Hz on a second scale making the estimation of the Q factor from its spectrum impossible. Another way to extract the Q factor is to perform a ring-down measurement, where the torsional mode is driven on resonance, the drive is abruptly stopped and the decay of the oscillation amplitude is recorded on an oscilloscope.

Figure 6.14(b) shows the result of such a ring-down measurement of the fundamental torsional mode. The data is band-pass filtered around the resonance frequency with a bandwidth of 1 kHz. The envelope of the resulting oscillation is fitted with an exponential, from which we extract the decay time of the amplitude of $\tau_{\text{ampl}} = 1.5$ s. Consequently, the resonance linewidth or damping rate can be derived as $\gamma = 2/\tau_{\text{ampl}} = 2\pi \times 0.2\,\text{Hz}$ and the Q-Factor as $Q = (\omega_0 \tau_{\text{ampl}})/2 = 7.7 \times 10^5$ at a resonance frequency $\omega_0 = 2\pi \times 162.3\,\text{kHz}$. These values are comparable to what has been reported in our group

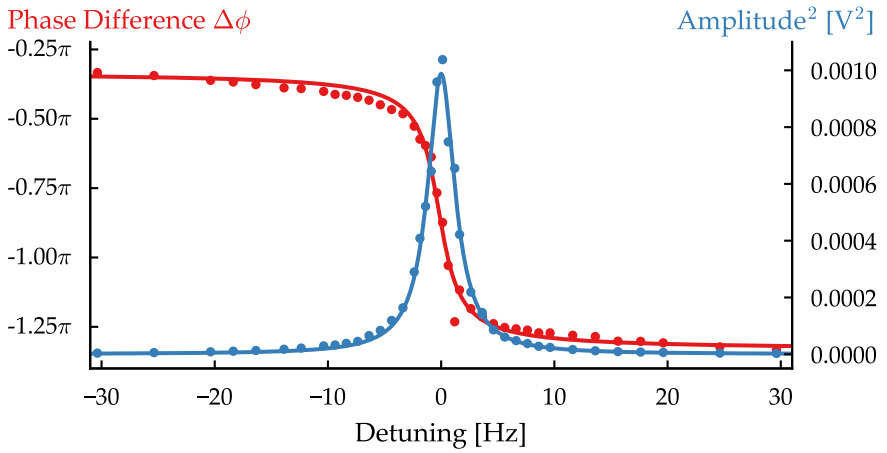

Figure 6.15: Bode plot illustrating the amplitude (blue) and phase response (red) of the torsional mode, with experimental data represented as dots and fits to the data with a harmonic oscillator model as solid lines. The phase difference between the drive and the signal changes by $-\pi$ above resonance while the amplitude follows a Lorentzian profile. This confirms that the system is linear in actuation as well as in detection and its behavior is consistent with a harmonic oscillator.

for measurements of the torsional motion for fibers with a similar profile and waist length [121, 124].

Amplitude and Phase Response

Figure 6.15 shows the Bode plot, i.e., the amplitude and phase response of the fundamental torsional mode when driven externally. The amplitude response shows a Lorentzian lineshape that is peaked at the resonance frequency. We plot the square of the amplitude as it is proportional to the energy in the resonator. The phase difference between signal and drive changes across resonance by $-\pi$ and is then out of phase with the drive. Both, the Lorentzian amplitude response and the phase response follow the behavior of a harmonic oscillator.

Furthermore, due to good fit between the data with the model, we can say that the system behaves linear in detection and in actuation, i.e., the nanofiber displacement $\varphi(t)$ is linearly proportional to the signal from the balanced photodiode $V(t)$ as well as the applied torque $M_{\text{ext}}(t)$ is linearly proportional to the applied voltage $V_{\text{drive}}(t)$ on the piezo.

To obtain this data, we drove the piezo actuator with a sinusoidal voltage with variable frequency ω and collected the polarization fluctuations using the out-of-loop balanced photodiode as sketched in Figure 6.12. At the same time, we also record the driving voltage on the oscilloscope. In order to compute the phase difference $\Delta\phi$ between the external driving voltage and the polarization fluctuation,

we first band-pass filter the measured signal from the balanced photodiode around the driving frequency. Then we compute the phase difference $\Delta\phi$ by comparing the mean angle of the complex power spectral density of the drive signal to that of the measured signal from the balanced photodiode. To compute the amplitude response of that signal, we take the mean of the absolute value of the filtered time-domain data from the polarization analysis setup and square it.

For monochromatic driving and in the steady state, the signal from the balanced photodiode can be described by the relation $V(t) = V(\omega)\cos\big(\omega t + \Delta\phi(\omega)\big)$ when assuming that $V^2(t)$ is proportional to the energy of the oscillator. The amplitude response $V(\omega)$ and the phase response $\Delta\phi(\omega)$ can be modeled by a simple damped harmonic oscillator model where [124, 127, 130]

$$V(\omega)^2 = \frac{V_0^2}{4\omega_0\left((\omega-\omega_0)^2+\gamma^2/4\right)} \tag{6.44}$$

$$\Delta\phi(\omega) = \phi_0 + \operatorname{atan2}\left(-\gamma\omega, 2\omega_0(\omega_0-\omega)\right). \tag{6.45}$$

Here ω is the drive frequency of the piezo, ω_0 is the resonance frequency of the torsional mode, V_0 is an amplitude factor, γ is the energy damping rate, ϕ_0 is a constant phase lag given by the specific experimental setup and atan2 is the extension of the arctangent function which is valid across all quadrants.

From the fit, we can extract the damping rate γ which we find for the amplitude response to be $\gamma_{\text{ampl}} = 2\pi \times 2.93$ Hz and for the phase response $\gamma_{\text{phase}} = 2\pi \times 2.71$ Hz. This corresponds to Q factors of 5.60×10^4 and 6.05×10^4. This is an order of magnitude lower than the Q factor that we have measured from the ring-down measurement in Figure 6.14(b). This might be because the Bode plot has been measured with a different nanofiber which had not been subjected to high laser powers before the measurement, which was found to increase the Q factor of the torsional motion [124, 127]. We did not perform a ring-down measurement with this nanofiber as it broke when we subjected it to the high laser powers required for trapping. The Q factors that we found from these fits, however, agree very well with values that were found in fibers that had not been subjected to high powers [127].

The phase response fit of the torsional motion in Figure 6.15 also exhibits a constant phase offset $\phi_0 = 0.33\pi$. This phase lag between driving and detection is most likely due to signal delays in our experimental setup and can stem from, for example, the delayed piezo response or from delays introduced by the balanced photodiode.

6.4.4 Feedback Cooling and Driving the Nanofiber Motion

Cooling the Torsional Mode

In order to cool the torsional motion of the nanofiber, we use a cold damping scheme in which the in-loop detection signal is fed back to the nanofiber via the piezo actuator with a phase shift of $\pi/2$, as has previously been demonstrated in our group [124, 127]. Due to the high Q factor of the torsional mode, the oscillatory motion stays phase-coherent for a long time and feedback cooling should be very effective. When the feedback signal exhibits a phase shift of $\pi/2$ with respect to the displacement $\varphi(t)$ of the nanofiber, the external feedback torque $M_{\text{ext}}(t)$ is in phase with the angular velocity of the torsional motion $\dot{\varphi}(t)$ and therefore acts as an additional frictional force. As we have found from the analysis of the Bode plot in the previous section, the nanofiber's rotational displacement $\varphi(t)$ is linearly proportional to the polarization fluctuation $\theta(t)$ and thus to the voltage signal from the polarization analysis $V(t)$. Furthermore, the applied torque $M_{\text{ext}}(t)$ is linear to the applied voltage $V_{\text{drive}}(t)$ on the piezo. We can therefore directly feedback the phase-shifted voltage signal to the piezo to cool the torsional motion.

Figure 6.12 shows an overview of the setup used for feedback cooling. To control the feedback, we use the Red Pitaya microcontroller running custom FPGA software originally developed by Felix Tebbenjohanns for feedback cooling of an optically trapped silica nanoparticle [131]. This program allows us to vary the time delay and thus the phase of the signal from the in-loop balanced photodiode. It also implements a bandpass filter around the torsional mode frequency and allows amplification of the output signal that is fed back to the piezo actuator. To find the correct delay that corresponds to a phase shift of $\pi/2$ and cools the motion, we first find the time delay that amplifies the torsional motion, i.e. that corresponds to a phase shift of zero. Then we delay the signal by a time delay corresponding to a phase shift of $\pi/2$ and fine-tune the delay and gain around this value until the out-of-loop signal shows minimal excitation of the torsional mode and thus cooling of the torsional motion.

Figure 6.16(a) depicts the power spectral density of the out-of-loop signal around the resonance frequency of the nanofiber's torsional motion with and without feedback cooling. The frequency resolution of this measurement is 0.25 Hz. The red curve shows the torsional motion without cooling when the fiber is in equilibrium with its environment, i.e. when it is only thermally driven and the blue curve shows the spectrum when we successfully feedback-cool the mode.

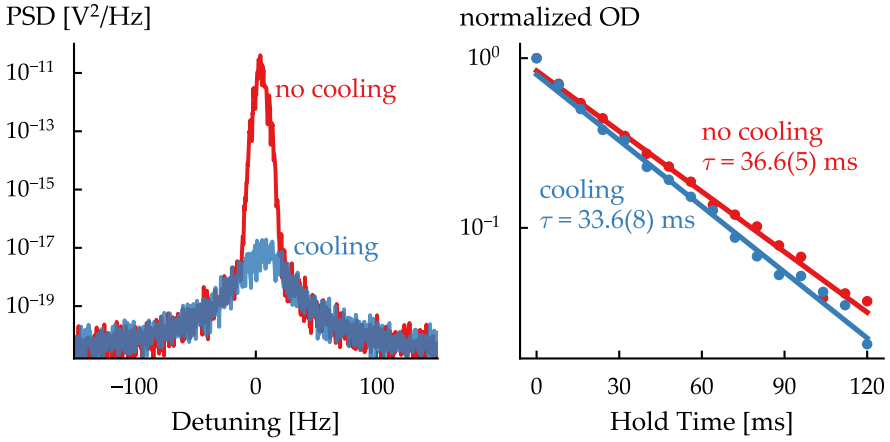

(a) Cooling of the torsional mode **(b)** Trap lifetime during cooling

Figure 6.16: (a) PSD of the out-of-loop signal of light transmitted through the nanofiber when the torsional motion is not cooled (red) and when the motion is feedback-cooled (blue). **(b)** A lifetime measurement of the trapped atoms when the torsional motion is not cooled (red) and when it is cooled (blue). Dots are experimental data and solid lines represent an exponential fit where τ is the lifetime and the number in parenthesis represents the error. Counter-intuitively, feedback cooling of the torsional motion worsens the lifetime of atoms trapped in the nanofiber. A likely explanation is that additional noise is introduced into the system when it is connected to the drive electronics.

Since the data was recorded over a period of 20 seconds, the mode profile is significantly broadened due to drifts of the resonance frequency on the Hz scale. We attribute these drifts to slight fluctuations in laser power, which we found to change the resonance frequency. We can derive a cooling ratio between the equilibrium and the cooled mode by integrating the power spectral density over a range of ±500 Hz around resonance, which yields a cooling ratio of about 200 for the torsional mode. While we have not measured the initial temperature of our nanofiber, previous measurements for a similar nanofiber geometry and similar launched powers have estimated the temperature to be on the order of 500 K [129]. Therefore, the effective temperature of the cooled torsional motion would be about 2.5 K.

Lifetime of Trapped Atoms when Cooling the Torsional Mode

In order to assess the influence of the torsional motion on the trapping of atoms, we will now compare the lifetimes of the atoms in the nanofiber traps for the cooled and non-cooled torsional mode. Figure 6.16(b) shows a measurement of the normalized optical depth for increasing hold times for the cases of cooling and not cooling the torsional motion. From an exponential fit to the data, we extract the

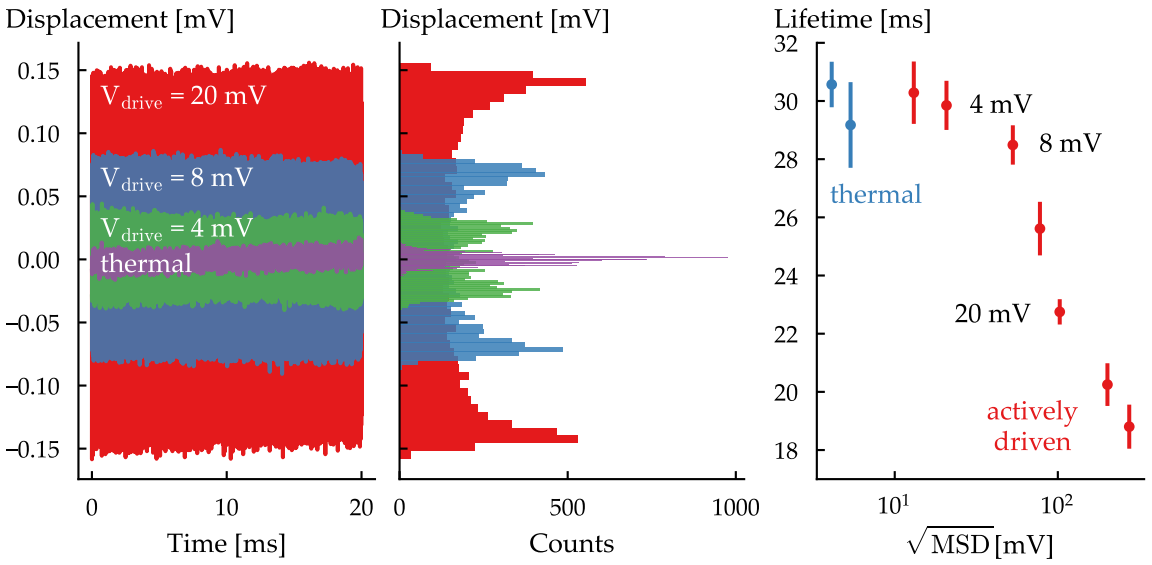

(a) Displacement from oscilloscope

(b) Histogram of displacements

(c) Lifetime while driving

Figure 6.17: Analysis of the influence of driving the torsional mode of the nanofiber. **(a)** The amplitude of the detected signal and thus the displacement increases with increasing drive amplitude compared to when the system is at thermal equilibrium. **(b)** A histogram of the displacements in (a) shows the characteristic distribution of a driven harmonic oscillator that is driven with increasing amplitudes. **(c)** The lifetime of trapped atoms starts to drop only for large nanofiber displacements given in terms of the square root of the mean-square displacement (MSD). This measure more accurately represents the extent of the displacement in comparison to the drive voltage. The square root ensures consistent units with the displacement measurement.

trap lifetime τ. We do not fit the first two experimental points at 0 and 8 ms because at these times there are still atoms from the molasses around the nanofiber that are not trapped and thus the OD for these points is higher. The data for the non-cooled atoms is the same as in Figure 6.9(a).

We observe that cooling the torsional mode does not result in an increase of the trap lifetime. On the contrary, in this experiment, the trap lifetime decreased from $\tau = 36.6(5)\,\text{ms}$ to $\tau = 33.6(8)\,\text{ms}$, a reduction of about 8% when we feedback-cool the motion. This suggests, that the feedback signal we apply on the piezo may act as noise that affects other mechanical modes, possibly amplifying their amplitude. If these modes couple to the atomic motion in the trap, this could explain the slight reduction in lifetime.

Actively Driving the Torsional Mode

To further study the influence of the torsional mode on the lifetime of trapped atoms, we also studied the opposite scenario where we

actively drive the torsional motion. As we will see, also driving the motion has no large detrimental effect on the trap lifetime.

In order to excite the torsional mode, we constantly drive it by applying a sinusoidal modulation on the piezo. We drive the mode slightly below resonance with varying output voltages. As before, we record the polarization fluctuations and thus measure the fiber displacement on an oscilloscope with the out-of-loop detection setup.

As shown in Figure 6.17, the amplitude of the torsional motion and therefore also the displacement signal increases with increasing drive voltage V_{drive}. This plot shows the measured polarization fluctuations when the system is in thermal equilibrium and for drives of 4 mV, 8 mV and 20 mV amplitude over a period of 20 ms. In Figure 6.17(b) we present the probability distribution of the displacements in Figure 6.17(a) in the form of a histogram with 50 bins for each measurement. The shape of the histogram is typical for the probability distribution of the position of a sinusoidally driven harmonic oscillator where the oscillator spends most time in the turning points of its oscillation.

In order to quantify the displacement of the fiber from its rest position, we use the mean square displacement (MSD) which is defined as $\langle |V(t) - \overline{V}|^2 \rangle$ with $V(t)$ as the fluctuating signal that we record on the oscilloscope as shown in Figure 6.17(a) and $\overline{V}$ as the mean value of the displacement, which was set to $\overline{V} = 0$ in this measurement. We then take the square root of the MSD to end up with the same units as the displacement signal.

To examine the effect of driving the oscillation, we measured the associated trap lifetime and Figure 6.17(c) presents the trap lifetimes for different drive voltages and therefore different MSDs. We also show two measurements when the system is only driven thermally in blue. The first point with the smallest $\sqrt{\text{MSD}}$ is the measurement that is also shown in the two plots on the left. The errorbar corresponds to the error of the exponential fit of the lifetime.

From the graph, it is apparent that when the torsional mode is not driven strongly, the lifetime does not decrease even though the mean displacement of the fiber is increased by more than an order of magnitude compared to thermal equilibrium. Only for large drive voltages, the lifetime starts to decrease.

These findings indicate that increasing the torsional motion of the fiber only has a small effect on the lifetime of trapped atoms. Combined with the results, that cooling the torsional mode has no effect on the lifetime, we can conclude that heating by torsional motion does not limit the lifetime of trapped atoms. These results experimentally validate the theoretical predictions of Hümmer et al. [116].

6.5 SUMMARY AND CONCLUSIONS

In this chapter, we described the implementation, optimization and characterization of nanofiber-based optical dipole traps in our experimental setup, and investigated the influence of the torsional motion of the nanofiber on the lifetime of trapped atoms.

First, we explained the working principle of the two-color trapping scheme that is used to generate an array of dipole traps and then described the necessary modifications to our setup to implement it. Since this scheme requires relatively high powers in the nanofiber-guided fields ($\approx$ 13 mW after optimization), we had to replace our previous nanofiber, which broke due to heating from surface impurities under these conditions. After numerous failed attempts, we identified an overaged HEPA filter as the source of the problem, which further enforced the need to maintain clean airflow during a nanofiber exchange.

We successfully fine-tuned the trapping parameters, achieving a maximum lifetime of atoms in the trap of 36.6 ms. The loading time for atoms to enter the traps was found to be $\approx$ 2 ms. By exploiting the local circular polarization in the evanescent field of the nanofiber and by applying a magnetic field, we were able to prepare the sub-ensembles on either side of the fiber in the $m_f = \pm 4$ states, respectively. Previously in our experiment, atoms were interfaced in random positions around the nanofiber, which did not allow for this level of control over the atomic states.

However, the lifetime of atoms in nanofiber-based traps is limited by larger heating rates compared to free-space traps. It has been hypothesized that the mechanical motion of the nanofiber contributes to this heating [116, 121, 132]. The torsional motion of the nanofiber couples to the polarization of the nanofiber-guided fields, which allowed us to measure this motion by analyzing the polarization fluctuations. This way, we observed the fundamental torsional mode, which has a Q factor of 7.7×10^5 in our structure. The mode has a frequency that is close to the trapping frequencies of our traps and could therefore influence the lifetime of the trapped atoms.

During the fiber exchange, we incorporated a piezo actuator into the nanofiber holder. This allowed us to feedback-cool the torsional motion of the nanofiber and reduce its effective temperature to 2.5 K. However, no significant effect on the trapping lifetime was observed. In further experiments, we also actively drove the torsional mode with the piezo actuator, but even though the angular displacement was orders of magnitude larger than that caused by thermal motion, we still found no major reduction in lifetime. The experimental results

support a previous theoretical study, which predicted that the torsional mode has a small contribution to the heating rate of trapped atoms.

7 CONCLUSIONS AND OUTLOOK

In this thesis, we have studied the transition from cavity to waveguide QED in a unique system that integrates a nanofiber-based optical interface coupled to neutral cesium atoms into a fiber-ring resonator with an adjustable cavity length.

First, we studied the system in a waveguide QED setting. By exciting the ensemble with short optical pulses, we observed collective phenomena such as superradiance, where the emission into the waveguide is enhanced, followed by the ensemble transitioning through several subradiant states, where the emission into the waveguide is suppressed. To understand these features, we derived analytical solutions for the system dynamics for ensembles prepared in the timed Dicke state based on a cascaded interaction model. Furthermore, we observed collective Rabi oscillations, which provided insight into the gradual build up of collective dynamics along the ensemble. These collective effects are enabled by interactions between multiple atoms mediated by the guided mode of the nanofiber.

We then explored the transition from cavity to waveguide QED experimentally by changing the length of the fiber-ring resonator and studying how the collective atomic response is modified. In the case of a 45-m-long cavity, the emitters were coupled to multiple longitudinal cavity modes, resulting in temporal dynamics that exhibited repeated features reminiscent of the collective single-pass dynamics of waveguide QED. When the resonator length was reduced to 6 m, the atomic ensemble coupled to fewer cavity modes and the temporal dynamics were characterized by single-pass features that partially overlapped. This then caused the dynamics to feature Rabi oscillations, typical of single-mode cavity QED. Our investigations in this new regime of cavity QED allow for a deeper understanding of light–matter interaction and reveal the intrinsic link between the collective single-pass dynamics and the associated ensemble–cavity dynamics.

While our unique resonator system presents many opportunities, it also faces a number of limitations such as a low single-atom coupling strength and high resonator losses.

During this thesis, we already took the first step towards increasing the light–atom coupling strength β by trapping atoms along the nanofiber using a two-color optical dipole trap. However, as in all nanofiber trapping schemes, the lifetime of trapped atoms in our

system is still limited to a few tens of millisecond, which could be a drawback for certain applications. To investigate the source of heating we studied the mechanical oscillations of the nanofiber structure. As we have found, the fundamental torsional mode does not significantly influence the lifetime of atoms even though its oscillation frequency ($\approx 164\,\mathrm{kHz}$) is close to the axial trap frequency ($\approx 168\,\mathrm{kHz}$). However, the flexural modes have been identified as a dominant heating source of trapped atoms in theoretical calculations [116]. In preliminary measurements, we found signatures of these modes distributed along the whole mechanical spectrum of the nanofiber, spaced at intervals of $\approx 1\,\mathrm{kHz}$ to $2\,\mathrm{kHz}$. Driving them caused significant heating of the atoms. To study their influence, the immediate next step is to update our experiment with a nanofiber that has a shorter waist, for which the frequency spacing between these modes is larger, leading to fewer flexural modes in the vicinity of the trapping frequencies. We will also add a stick-slip piezo actuator to the fiber holder to strain the fiber. By adjusting this strain, we aim to modify the flexural mode spectrum, and evaluate the impact on the heating of atoms in the traps.

The main goal for our experiment remains to implement a fiber-ring resonator that includes trapped atoms. To achieve trapping around a nanofiber, the polarizations of three light fields must be precisely adjusted. When such a trap is integrated into a fiber-ring resonator, these polarizations must also be matched with the intrinsic eigenpolarizations of the resonator. The many degrees of freedom make this task very challenging in a conventional fiber-ring resonator. To solve this problem, we intend to build a resonator which is resonant for the probe light, while allowing only a single pass for the trapping laser fields. To achieve this, we have fabricated a special type of four-port fiber beam splitter based on a so-called null coupler [112, 133]. This coupler is made by fusing two tapered fiber with different diameters, which prevents mode coupling under normal conditions. However, when an acoustic wave is applied to the coupler using a piezo actuator, the modes in the fused fibers can be phase-matched, allowing them to couple. This realizes an acoustically controllable, low-loss coupler that in addition is highly wavelength- and polarization-dependent. By using two of these null couplers in series, placed before and after the trapped atoms, we can then construct a resonator that is only resonant for the probe light and includes trapped atoms.

The higher cavity Finesse achievable with such a coupler and the higher light–atom coupling strength enabled by trapping atoms, should allow us to reach a single-atom cooperativity between five and ten, which would place our system in the single-atom strong coupling regime. Together with the non-Markovian, i.e., time-delayed, feedback present in our long resonator, our system should enable the

observation of new quantum features. For example, we could study the system's interaction with its time-delayed emission following the preparation of the ensemble in a highly excited state [134], potentially leading to interesting photon correlations.

Other potential applications for our platform include research in emerging quantum technologies. Our system's ability to interface many atoms could enable complex operations, for example, by using the atoms as qubits that are strongly coupled to a common cavity mode for information transfer between the qubits. As our resonator system is completely fiber-based, it is easily interfaced with quantum communications networks. An example that shows the interest in such a platform is that another group recently raised funding for a startup company (NanoQT), to set up and connect multiple nanofiber-based cavity systems [103, 135] to realize a quantum communications network. Furthermore, coupling many emitters to the cavity mode in our setup could be advantageous for research on photon-transport dynamics [136–138], which scale favorably with the number of involved emitters. In conjunction with our multi-mode resonator, this scheme could be extended to generate highly non-classical quantum states of light that are relevant for quantum information science.

BIBLIOGRAPHY

[1] Serge Haroche and Daniel Kleppner. Cavity Quantum Electrodynamics. *Physics Today*, 42(1), 1989.

[2] J M Raimond, M Brune, and S Haroche. Colloquium: Manipulating quantum entanglement with atoms and photons in a cavity. *Rev. Mod. Phys.*, 73(3), 2001.

[3] S. Haroche and J.-M. Raimond. *Exploring the Quantum: Atoms, Cavities and Photons*. Oxford University Press, 2006.

[4] Edward Mills Purcell. Spontaneous Emission Probabilities at Radio Frequencies. *Physical Review A*, 69(681), 1946.

[5] Karl H. Drexhage. Influence of a dielectric interface on fluorescence decay time. *Journal of Luminescence*, 1–2, 1970.

[6] Karl H. Drexhage. IV Interaction of Light with Monomolecular Dye Layers. In *Progress in Optics*. Volume 12. Elsevier, 1974.

[7] P. Goy, J. M. Raimond, M. Gross, and S. Haroche. Observation of Cavity-Enhanced Single-Atom Spontaneous Emission. *Physical Review Letters*, 50(24), 1983.

[8] D. J. Heinzen, J. J. Childs, J. E. Thomas, and M. S. Feld. Enhanced and inhibited visible spontaneous emission by atoms in a confocal resonator. *Physical Review Letters*, 58(13), 1987.

[9] F. De Martini, G. Innocenti, G. R. Jacobovitz, and P. Mataloni. Anomalous Spontaneous Emission Time in a Microscopic Optical Cavity. *Physical Review Letters*, 59(26), 1987.

[10] W. Jhe, A. Anderson, E. A. Hinds, D. Meschede, L. Moi, and S. Haroche. Suppression of spontaneous decay at optical frequencies: Test of vacuum-field anisotropy in confined space. *Physical Review Letters*, 58(7), 1987.

[11] Randall G. Hulet, Eric S. Hilfer, and Daniel Kleppner. Inhibited Spontaneous Emission by a Rydberg Atom. *Physical Review Letters*, 55(20), 1985.

[12] Gerald Gabrielse and Hans Dehmelt. Observation of inhibited spontaneous emission. *Physical Review Letters*, 55(1), 1985.

[13] E.T. Jaynes and F.W. Cummings. Comparison of quantum and semiclassical radiation theories with application to the beam maser. *Proceedings of the IEEE*, 51(1), 1963.

[14] Y. Kaluzny, P. Goy, M. Gross, J. M. Raimond, and S. Haroche. Observation of Self-Induced Rabi Oscillations in Two-Level Atoms Excited Inside a Resonant Cavity: The Ringing Regime of Superradiance. *Physical Review Letters*, 51(13), 1983.

[15] Gerhard Rempe, Herbert Walther, and Norbert Klein. Observation of quantum collapse and revival in a one-atom maser. *Physical Review Letters*, 58(4), 1987.

[16] R. J. Brecha, L. A. Orozco, M. G. Raizen, Min Xiao, and H. J. Kimble. Observation of oscillatory energy exchange in a coupled-atom–cavity system. *Journal of the Optical Society of America B*, 12(12), 1995.

[17] M. Brune, F. Schmidt-Kaler, A. Maali, J. Dreyer, E. Hagley, J. M. Raimond, and S. Haroche. Quantum Rabi Oscillation: A Direct Test of Field Quantization in a Cavity. *Physical Review Letters*, 76(11), 1996.

[18] S. L. Mielke, G. T. Foster, J. Gripp, and L. A. Orozco. Time response of a coupled atoms–cavity system. *Optics Letters*, 22(5), 1997.

[19] R. J. Thompson, G. Rempe, and H. J. Kimble. Observation of normal-mode splitting for an atom in an optical cavity. *Physical Review Letters*, 68(8), 1992.

[20] F Bernardot, P Nussenzveig, M Brune, J. M Raimond, and S Haroche. Vacuum Rabi Splitting Observed on a Microscopic Atomic Sample in a Microwave Cavity. *Europhysics Letters*, 17(1), 1992.

[21] A. Boca, R. Miller, K. M. Birnbaum, A. D. Boozer, J. McKeever, and H. J. Kimble. Observation of the Vacuum Rabi Spectrum for One Trapped Atom. *Physical Review Letters*, 93(23), 2004.

[22] P. Maunz, T. Puppe, I. Schuster, N. Syassen, P. W. H. Pinkse, and G. Rempe. Normal-Mode Spectroscopy of a Single-Bound-Atom–Cavity System. *Physical Review Letters*, 94(3), 2005.

[23] Serge Haroche. Nobel Lecture: Controlling photons in a box and exploring the quantum to classical boundary. *Reviews of Modern Physics*, 85(3), 2013.

[24] David J. Wineland. Nobel Lecture: Superposition, entanglement, and raising Schrödinger's cat. *Reviews of Modern Physics*, 85(3), 2013.

[25] A. Rauschenbeutel, G. Nogues, S. Osnaghi, P. Bertet, M. Brune, J. M. Raimond, and S. Haroche. Coherent Operation of a Tunable Quantum Phase Gate in Cavity QED. *Physical Review Letters*, 83(24), 1999.

[26] T. Pellizzari, S. A. Gardiner, J. I. Cirac, and P. Zoller. Decoherence, Continuous Observation, and Quantum Computing: A Cavity QED Model. *Physical Review Letters*, 75(21), 1995.

[27] J. I. Cirac, P. Zoller, H. J. Kimble, and H. Mabuchi. Quantum State Transfer and Entanglement Distribution among Distant Nodes in a Quantum Network. *Physical Review Letters*, 78(16), 1997.

[28] Axel Kuhn, Markus Hennrich, and Gerhard Rempe. Deterministic Single-Photon Source for Distributed Quantum Networking. *Physical Review Letters*, 89(6), 2002.

[29] L.-M. Duan and H. J. Kimble. Scalable Photonic Quantum Computation through Cavity-Assisted Interactions. *Physical Review Letters*, 92(12), 2004.

[30] A. D. Boozer, A. Boca, R. Miller, T. E. Northup, and H. J. Kimble. Reversible State Transfer between Light and a Single Trapped Atom. *Physical Review Letters*, 98(19), 2007.

[31] Stephan Ritter, Christian Nölleke, Carolin Hahn, Andreas Reiserer, Andreas Neuzner, Manuel Uphoff, Martin Mücke, Eden Figueroa, Joerg Bochmann, and Gerhard Rempe. An elementary quantum network of single atoms in optical cavities. *Nature*, 484(7393), 2012.

[32] Andreas Reiserer and Gerhard Rempe. Cavity-based quantum networks with single atoms and optical photons. *Reviews of Modern Physics*, 87(4), 2015.

[33] Peter Lodahl, Sahand Mahmoodian, and Søren Stobbe. Interfacing single photons and single quantum dots with photonic nanostructures. *Reviews of Modern Physics*, 87(2), 2015.

[34] A. P. Foster, D. Hallett, I. V. Iorsh, S. J. Sheldon, M. R. Godsland, B. Royall, E. Clarke, I. A. Shelykh, A. M. Fox, M. S. Skolnick, et al. Tunable Photon Statistics Exploiting the Fano Effect in a Waveguide. *Physical Review Letters*, 122(17), 2019.

[35] A. Sipahigil, R. E. Evans, D. D. Sukachev, M. J. Burek, J. Borregaard, M. K. Bhaskar, C. T. Nguyen, J. L. Pacheco, H. A. Atikian, C. Meuwly, et al. An integrated diamond nanophotonics platform for quantum-optical networks. *Science*, 354(6314), 2016.

[36] A. Goban, C.-L. Hung, J. D. Hood, S.-P. Yu, J. A. Muniz, O. Painter, and H. J. Kimble. Superradiance for Atoms Trapped along a Photonic Crystal Waveguide. *Physical Review Letters*, 115(6), 2015.

[37] Arjan F. Van Loo, Arkady Fedorov, Kevin Lalumière, Barry C. Sanders, Alexandre Blais, and Andreas Wallraff. Photon-Mediated Interactions Between Distant Artificial Atoms. *Science*, 342(6165), 2013.

[38] Caleb A. Christensen, Sebastian Will, Michele Saba, Gyu-Boong Jo, Yong-Il Shin, Wolfgang Ketterle, and David Pritchard. Trapping of ultracold atoms in a hollow-core photonic crystal fiber. *Physical Review A*, 78(3), 2008.

[39] M. Bajcsy, S. Hofferberth, V. Balic, T. Peyronel, M. Hafezi, A. S. Zibrov, V. Vuletic, and M. D. Lukin. Efficient All-Optical Switching Using Slow Light within a Hollow Fiber. *Physical Review Letters*, 102(20), 2009.

[40] Shoichi Okaba, Deshui Yu, Luca Vincetti, Fetah Benabid, and Hidetoshi Katori. Superradiance from lattice-confined atoms inside hollow core fibre. *Communications Physics*, 2(1), 2019.

[41] E. Vetsch, D. Reitz, G. Sagué, R. Schmidt, S. T. Dawkins, and A. Rauschenbeutel. Optical Interface Created by Laser-Cooled Atoms Trapped in the Evanescent Field Surrounding an Optical Nanofiber. *Physical Review Letters*, 104(20), 2010.

[42] Marlan O. Scully, Edward S. Fry, C. H. Raymond Ooi, and Krzysztof Wódkiewicz. Directed Spontaneous Emission from an Extended Ensemble of N Atoms: Timing Is Everything. *Physical Review Letters*, 96(1), 2006.

[43] Marlan O. Scully and Anatoly A. Svidzinsky. The Super of Superradiance. *Science*, 325(5947), 2009.

[44] Pablo Solano, Jeffrey A. Grover, Jonathan E. Hoffman, Sylvain Ravets, Fredrik K. Fatemi, Luis A. Orozco, and Steven L. Rolston. Optical Nanofibers. In *Advances In Atomic, Molecular, and Optical Physics*. Volume 66. Elsevier, 2017.

[45] Martin Ligare and Ryan Oliveri. The calculated photon: Visualization of a quantum field. *American Journal of Physics*, 70(1), 2002.

[46] D. Meiser and P. Meystre. Superstrong coupling regime of cavity quantum electrodynamics. *Physical Review A*, 74(6), 2006.

[47] Dmitry O. Krimer, Matthias Liertzer, Stefan Rotter, and Hakan E. Türeci. Route from spontaneous decay to complex multimode dynamics in cavity QED. *Physical Review A*, 89(3), 2014.

[48] Martin Blaha, Aisling Johnson, Arno Rauschenbeutel, and Jürgen Volz. Beyond the Tavis-Cummings model: Revisiting cavity QED with ensembles of quantum emitters. *Physical Review A*, 105(1), 2022.

[49] Dario Cilluffo, Luca Ferialdi, G. Massimo Palma, Giuseppe Calajò, and Francesco Ciccarello. Multimode-cavity picture of non-Markovian waveguide QED. arXiv: 2403.07110, 2024.

[50] Yves Colombe, Tilo Steinmetz, Guilhem Dubois, Felix Linke, David Hunger, and Jakob Reichel. Strong atom–field coupling for Bose–Einstein condensates in an optical cavity on a chip. *Nature*, 450(7167), 2007.

[51] Helmut Ritsch, Peter Domokos, Ferdinand Brennecke, and Tilman Esslinger. Cold atoms in cavity-generated dynamical optical potentials. *Reviews of Modern Physics*, 85(2), 2013.

[52] Kerry J. Vahala. Optical microcavities. *Nature*, 424(6950), 2003.

[53] M. Pöllinger, D. O'Shea, F. Warken, and A. Rauschenbeutel. Ultrahigh- Q Tunable Whispering-Gallery-Mode Microresonator. *Physical Review Letters*, 103(5), 2009.

[54] Christian Junge, Danny O'Shea, Jürgen Volz, and Arno Rauschenbeutel. Strong Coupling between Single Atoms and Nontransversal Photons. *Physical Review Letters*, 110(21), 2013.

[55] Martin Blaha. *Multimode Strong Coupling of Cold Atoms to a Fiber Ring Resonator Including a Nanofiber-Based Optical Interface*, Technische Universität Wien, 2021.

[56] Florian Warken. *Ultradünne Glasfasern als Werkzeug zur Kopplung von Licht und Materie*, Universität Bonn, 2007.

[57] R. Garcia-Fernandez, W. Alt, F. Bruse, C. Dan, K. Karapetyan, O. Rehband, A. Stiebeiner, U. Wiedemann, D. Meschede, and A. Rauschenbeutel. Optical nanofibers and spectroscopy. *Applied Physics B*, 105(1), 2011.

[58] Eugen Vetsch. *Optical Interface Based on a Nanofiber Atom-Trap*, Johannes Gutenberg-Universität Mainz, 2010.

[59] Guillem Sagué Cassany. *Cold atom physics using ultra-thin optical fibres*, Universität Bonn, 2008.

[60] T.W. Hansch and B. Couillaud. Laser frequency stabilization by polarization spectroscopy of a reflecting reference cavity. *Optics Communications*, 35(3), 1980.

[61] Adam Libson, Nicolas Brown, Aaron Buikema, Camilo Cela López, Tamara Dordevic, Matthew Heising, and Matthew Evans. Simple method for locking birefringent resonators. *Optics Express*, 23(3), 2015.

[62] Aisling Johnson, Martin Blaha, Alexander E. Ulanov, Arno Rauschenbeutel, Philipp Schneeweiss, and Jürgen Volz. Observation of Collective Superstrong Coupling of Cold Atoms to a 30-m Long Optical Resonator. *Physical Review Letters*, 123(24), 2019.

[63] Jung-Tsung Shen and Shanhui Fan. Theory of single-photon transport in a single-mode waveguide. I. Coupling to a cavity containing a two-level atom. *Physical Review A*, 79(2), 2009.

[64] Riccardo Pennetta, Martin Blaha, Aisling Johnson, Daniel Lechner, Philipp Schneeweiss, Jürgen Volz, and Arno Rauschenbeutel. Collective Radiative Dynamics of an Ensemble of Cold Atoms Coupled to an Optical Waveguide. *Physical Review Letters*, 128(7), 2022.

[65] Peter Lodahl, Sahand Mahmoodian, Søren Stobbe, Arno Rauschenbeutel, Philipp Schneeweiss, Jürgen Volz, Hannes Pichler, and Peter Zoller. Chiral quantum optics. *Nature*, 541(7638), 2017.

[66] D. Reitz, C. Sayrin, B. Albrecht, I. Mazets, R. Mitsch, P. Schneeweiss, and A. Rauschenbeutel. Backscattering properties of a waveguide-coupled array of atoms in the strongly nonparaxial regime. *Physical Review A*, 89(3), 2014.

[67] Michael Tavis and Frederick W. Cummings. Exact Solution for an N-Molecule-Radiation-Field Hamiltonian. *Physical Review*, 170(2), 1968.

[68] Michael Tavis and Frederick W. Cummings. Approximate Solutions for an N-Molecule-Radiation-Field Hamiltonian. *Physical Review*, 188(2), 1969.

[69] C. C. Gerry and Peter Knight. *Introductory Quantum Optics*. Cambridge University Press, Cambridge, UK ; New York, 2005.

[70] Ferdinand Brennecke, Tobias Donner, Stephan Ritter, Thomas Bourdel, Michael Köhl, and Tilman Esslinger. Cavity QED with a Bose–Einstein condensate. *Nature*, 450(7167), 2007.

[71] André Pscherer, Manuel Meierhofer, Daqing Wang, Hrishikesh Kelkar, Diego Martín-Cano, Tobias Utikal, Stephan Götzinger, and Vahid Sandoghdar. Single-Molecule Vacuum Rabi Splitting: Four-Wave Mixing and Optical Switching at the Single-Photon Level. *Physical Review Letters*, 127(13), 2021.

[72] J. M. Fink, M. Göppl, M. Baur, R. Bianchetti, P. J. Leek, A. Blais, and A. Wallraff. Climbing the Jaynes–Cummings ladder and observing its nonlinearity in a cavity QED system. *Nature*, 454(7202), 2008.

[73] R. H. Dicke. Coherence in Spontaneous Radiation Processes. *Physical Review*, 93(1), 1954.

[74] Michelle O. Araújo, Ivor Krešić, Robin Kaiser, and William Guerin. Superradiance in a Large and Dilute Cloud of Cold Atoms in the Linear-Optics Regime. *Physical Review Letters*, 117(7), 2016.

[75] S. J. Roof, K. J. Kemp, M. D. Havey, and I. M. Sokolov. Observation of Single-Photon Superradiance and the Cooperative Lamb Shift in an Extended Sample of Cold Atoms. *Physical Review Letters*, 117(7), 2016.

[76] William Guerin, Michelle O. Araújo, and Robin Kaiser. Subradiance in a Large Cloud of Cold Atoms. *Physical Review Letters*, 116(8), 2016.

[77] Robert J. Bettles, Teodora Ilieva, Hannes Busche, Paul Huillery, Simon W. Ball, Nicholas L. R. Spong, and Charles S. Adams. Collective Mode Interferences in Light-Matter Interactions. arXiv: 1808.08415, 2020.

[78] G. Ferioli, A. Glicenstein, F. Robicheaux, R. T. Sutherland, A. Browaeys, and I. Ferrier-Barbut. Laser-Driven Superradiant Ensembles of Two-Level Atoms near Dicke Regime. *Physical Review Letters*, 127(24), 2021.

[79] Asaf Paris-Mandoki, Christoph Braun, Jan Kumlin, Christoph Tresp, Ivan Mirgorodskiy, Florian Christaller, Hans Peter Büchler, and Sebastian Hofferberth. Free-Space Quantum Electrodynamics with a Single Rydberg Superatom. *Physical Review X*, 7(4), 2017.

[80] Nina Stiesdal, Hannes Busche, Jan Kumlin, Kevin Kleinbeck, Hans Peter Büchler, and Sebastian Hofferberth. Observation of collective decay dynamics of a single Rydberg superatom. *Physical Review Research*, 2(4), 2020.

[81] Ralf Röhlsberger, Kai Schlage, Balaram Sahoo, Sebastien Couet, and Rudolf Rüffer. Collective Lamb Shift in Single-Photon Superradiance. *Science*, 328(5983), 2010.

[82] Tom Bienaimé, Nicola Piovella, and Robin Kaiser. Controlled Dicke Subradiance from a Large Cloud of Two-Level Systems. *Physical Review Letters*, 108(12), 2012.

[83] Anatoly A. Svidzinsky, Jun-Tao Chang, and Marlan O. Scully. Dynamical Evolution of Correlated Spontaneous Emission of a Single Photon from a Uniformly Excited Cloud of N Atoms. *Physical Review Letters*, 100(16), 2008.

[84] W. Guerin, T. S. Do Espirito Santo, P. Weiss, A. Cipris, J. Schachenmayer, R. Kaiser, and R. Bachelard. Collective Multimode Vacuum Rabi Splitting. *Physical Review Letters*, 123(24), 2019.

[85] Fam Le Kien and K. Hakuta. Spontaneous radiative decay of translational levels of an atom near a dielectric surface. *Physical Review A*, 75(1), 2007.

[86] Kanupriya Sinha, Pierre Meystre, Elizabeth A. Goldschmidt, Fredrik K. Fatemi, S. L. Rolston, and Pablo Solano. Non-Markovian Collective Emission from Macroscopically Separated Emitters. *Physical Review Letters*, 124(4), 2020.

[87] Daniel A. Steck. Cesium D Line Data. 2019.

[88] C. C. Kwong, T. Yang, M. S. Pramod, K. Pandey, D. Delande, R. Pierrat, and D. Wilkowski. Cooperative Emission of a Coherent Superflash of Light. *Physical Review Letters*, 113(22), 2014.

[89] Riccardo Pennetta, Daniel Lechner, Martin Blaha, Arno Rauschenbeutel, Philipp Schneeweiss, and Jürgen Volz. Observation of Coherent Coupling between Super- and Subradiant States of an Ensemble of Cold Atoms Collectively Coupled to a Single Propagating Optical Mode. *Physical Review Letters*, 128(20), 2022.

[90] Jan Kumlin, Kevin Kleinbeck, Nina Stiesdal, Hannes Busche, Sebastian Hofferberth, and Hans Peter Büchler. Nonexponential decay of a collective excitation in an atomic ensemble coupled to a one-dimensional waveguide. *Physical Review A*, 102(6), 2020.

[91] H. H. Jen, M.-S. Chang, G.-D. Lin, and Y.-C. Chen. Subradiance dynamics in a singly excited chirally coupled atomic chain. *Physical Review A*, 101(2), 2020.

[92] P. R. Berman. Theory of two atoms in a chiral waveguide. *Physical Review A*, 101(1), 2020.

[93] V. A. Pivovarov, L. V. Gerasimov, J. Berroir, T. Ray, J. Laurat, A. Urvoy, and D. V. Kupriyanov. Single collective excitation of an atomic array trapped along a waveguide: A study of cooperative emission for different atomic chain configurations. *Physical Review A*, 103(4), 2021.

[94] Fam Le Kien and A. Rauschenbeutel. Nanofiber-mediated chiral radiative coupling between two atoms. *Physical Review A*, 95(2), 2017.

[95] U. Van Bürck. Coherent pulse propagation through resonant media. *Hyperfine Interactions*, 123, 1999.

[96] Johann Haber, Xiangjin Kong, Cornelius Strohm, Svenja Willing, Jakob Gollwitzer, Lars Bocklage, Rudolf Rüffer, Adriana Pálffy, and Ralf Röhlsberger. Rabi oscillations of X-ray radiation between two nuclear ensembles. *Nature Photonics*, 11(11), 2017.

[97] Leon M. Lohse, Petar Andrejić, Sven Velten, Malte Vassholz, Charlotte Neuhaus, Ankita Negi, Anjali Panchwanee, Ilya Sergeev, Adriana Pálffy, Tim Salditt, et al. Collective nuclear excitation dynamics in mono-modal x-ray waveguides. arXiv: 2403.06508, 2024.

[98] Fam Le Kien, S. Dutta Gupta, V. I. Balykin, and K. Hakuta. Spontaneous emission of a cesium atom near a nanofiber: Efficient coupling of light to guided modes. *Physical Review A*, 72(3), 2005.

[99] S. T. Dawkins, R. Mitsch, D. Reitz, E. Vetsch, and A. Rauschenbeutel. Dispersive Optical Interface Based on Nanofiber-Trapped Atoms. *Physical Review Letters*, 107(24), 2011.

[100] Daniel Lechner, Riccardo Pennetta, Martin Blaha, Philipp Schneeweiss, Arno Rauschenbeutel, and Jürgen Volz. Light-Matter Interaction at the Transition between Cavity and Waveguide QED. *Physical Review Letters*, 131(10), 2023.

[101] Neereja M. Sundaresan, Yanbing Liu, Darius Sadri, László J. Szőcs, Devin L. Underwood, Moein Malekakhlagh, Hakan E. Türeci, and Andrew A. Houck. Beyond Strong Coupling in a Multimode Cavity. *Physical Review X*, 5(2), 2015.

[102] J. Bochmann, M. Mücke, G. Langfahl-Klabes, C. Erbel, B. Weber, H. P. Specht, D. L. Moehring, and G. Rempe. Fast Excitation and Photon Emission of a Single-Atom-Cavity System. *Physical Review Letters*, 101(22), 2008.

[103] Shinya Kato and Takao Aoki. Strong Coupling between a Trapped Single Atom and an All-Fiber Cavity. *Physical Review Letters*, 115(9), 2015.

[104] Chaohan Cui, Liang Zhang, Bo-Han Wu, Shuai Liu, Pao-Kang Chen, and Linran Fan. Distinguishing under- and over-coupled resonances without prior knowledge. *Optica*, 11(2), 2024.

[105] Serge Rosenblum, Yulia Lovsky, Lior Arazi, Frank Vollmer, and Barak Dayan. Cavity ring-up spectroscopy for ultrafast sensing with optical microresonators. *Nature Communications*, 6(1), 2015.

[106] Y B Ovchinnikov, S V Shul'ga, and V I Balykin. An atomic trap based on evanescent light waves. *Journal of Physics B: Atomic, Molecular and Optical Physics*, 24(14), 1991.

[107] Fam Le Kien, V. I. Balykin, and K. Hakuta. Atom trap and waveguide using a two-color evanescent light field around a subwavelength-diameter optical fiber. *Physical Review A*, 70(6), 2004.

[108] A. Goban, K. S. Choi, D. J. Alton, D. Ding, C. Lacroûte, M. Pototschnig, T. Thiele, N. P. Stern, and H. J. Kimble. Demonstration of a State-Insensitive, Compensated Nanofiber Trap. *Physical Review Letters*, 109(3), 2012.

[109] Neil V. Corzo, Jérémy Raskop, Aveek Chandra, Alexandra S. Sheremet, Baptiste Gouraud, and Julien Laurat. Waveguide-coupled single collective excitation of atomic arrays. *Nature*, 566(7744), 2019.

[110] J.-B. Béguin, J. Laurat, X. Luan, A. P. Burgers, Z. Qin, and H. J. Kimble. Reduced volume and reflection for bright optical tweezers with radial Laguerre–Gauss beams. *Proceedings of the National Academy of Sciences*, 117(42), 2020.

[111] J Lee, J A Grover, J E Hoffman, L A Orozco, and S L Rolston. Inhomogeneous broadening of optical transitions of ^{87} Rb atoms in an optical nanofiber trap. *Journal of Physics B: Atomic, Molecular and Optical Physics*, 48(16), 2015.

[112] Martin Blaha, Arno Rauschenbeutel, and Riccardo Pennetta. A low-loss and broadband all-fiber acousto-optic circulator. arXiv: 2405.12903, 2024.

[113] Fam Le Kien, Victor I. Balykin, and Kohzo Hakuta. State-Insensitive Trapping and Guiding of Cesium Atoms Using a Two-Color Evanescent Field around a Subwavelength-Diameter Fiber. *Journal of the Physical Society of Japan*, 74(3), 2005.

[114] C Lacroûte, K S Choi, A Goban, D J Alton, D Ding, N P Stern, and H J Kimble. A state-insensitive, compensated nanofiber trap. *New Journal of Physics*, 14(2), 2012.

[115] Adarsh Shankar Prasad. *Generating Correlations between Photons via Interaction with Nanofiber-Trapped Atoms*, Technische Universität Wien, Wien, 2020.

[116] Daniel Hümmer, Philipp Schneeweiss, Arno Rauschenbeutel, and Oriol Romero-Isart. Heating in Nanophotonic Traps for Cold Atoms. *Physical Review X*, 9(4), 2019.

[117] Lucas Pache, Martin Cordier, Max Schemmer, Philipp Schneeweiss, Jürgen Volz, and Arno Rauschenbeutel. Realization of a magic-wavelength nanofiber-based two-color dipole trap with sub-lambda/2 spacing. arXiv: 2407.02278, 2024.

[118] C. J. Foot. *Atomic Physics*. Oxford Master Series in Physics. Oxford University Press, 2005. 331 pages.

[119] R. Mitsch, C. Sayrin, B. Albrecht, P. Schneeweiss, and A. Rauschenbeutel. Quantum state-controlled directional spontaneous emission of photons into a nanophotonic waveguide. *Nature Communications*, 5(1), 2014.

[120] R. Mitsch, C. Sayrin, B. Albrecht, P. Schneeweiss, and A. Rauschenbeutel. Exploiting the local polarization of strongly confined light for sub-micrometer-resolution internal state preparation and manipulation of cold atoms. *Physical Review A*, 89(6), 2014.

[121] C. Wuttke, G. D. Cole, and A. Rauschenbeutel. Optically active mechanical modes of tapered optical fibers. *Physical Review A*, 88(6), 2013.

[122] Lijun Song, Chenxi Wang, Yudong Hu, Jing Zhou, Qiang Zhang, Chang-Ling Zou, Gang Li, Pengfei Zhang, and Tiancai Zhang. Measurement of Nanofiber Mechanical Flexural Modes Based on Near-Field Scattering. *Physical Review Letters*, 132(3), 2024.

[123] Riccardo Pennetta, Shangran Xie, and Philip St.J. Russell. Tapered Glass-Fiber Microspike: High- Q Flexural Wave Resonator and Optically Driven Knudsen Pump. *Physical Review Letters*, 117(27), 2016.

[124] Felix Tebbenjohanns, Jihao Jia, Michael Antesberger, Adarsh Shankar Prasad, Sebastian Pucher, Arno Rauschenbeutel, Jürgen Volz, and Philipp Schneeweiss. Feedback cooling the fundamental torsional mechanical mode of a tapered optical fiber to 30 mK. *Physical Review A*, 108(3), 2023.

[125] Johannes Wiedersich, Sergei V. Adichtchev, and Ernst Rössler. Spectral Shape of Relaxations in Silica Glass. *Physical Review Letters*, 84(12), 2000.

[126] Steven D. Penn, Alexander Ageev, Dan Busby, Gregory M. Harry, Andri M. Gretarsson, Kenji Numata, and Phil Willems. Frequency and surface dependence of the mechanical loss in fused silica. *Physics Letters A*, 352(1-2), 2006.

[127] Jihao Jia. *Torsional Optomechanics with the High-Q Fundamental Mode of a Tapered Optical Fiber*. Master's thesis, Humboldt-Universität zu Berlin, 2023.

[128] P. Welch. The use of fast Fourier transform for the estimation of power spectra: A method based on time averaging over short, modified periodograms. *IEEE Transactions on Audio and Electroacoustics*, 15(2), 1967.

[129] C. Wuttke and A. Rauschenbeutel. Thermalization via Heat Radiation of an Individual Object Thinner than the Thermal Wavelength. *Physical Review Letters*, 111(2), 2013.

[130] Richard P. Feynman, Robert B. Leighton, and Matthew L. Sands. *The Feynman Lectures on Physics*. Basic Books, 2011.

[131] Felix Tebbenjohanns. *Linear Feedback Cooling of a Levitated Nanoparticle in Free Space*, ETH Zürich, 2020.

[132] Christian Wuttke. *Thermal Excitations of Optical Nanofibers Measured with a Fiber-Integrated Fabry-Pérot Cavity*, Johannes Gutenberg-Universität Mainz, 2014.

[133] T.A. Birks, P.S.J. Russell, and D.O. Culverhouse. The acousto-optic effect in single-mode fiber tapers and couplers. *Journal of Lightwave Technology*, 14(11), 1996.

[134] Christian Liedl, Sebastian Pucher, Felix Tebbenjohanns, Philipp Schneeweiss, and Arno Rauschenbeutel. Collective Radiation of a Cascaded Quantum System: From Timed Dicke States to Inverted Ensembles. *Physical Review Letters*, 130(16), 2023.

[135] Shinya Kato, Nikolett Német, Kohei Senga, Shota Mizukami, Xinhe Huang, Scott Parkins, and Takao Aoki. Observation of dressed states of distant atoms with delocalized photons in coupled-cavities quantum electrodynamics. *Nature Communications*, 10(1), 2019.

[136] Sahand Mahmoodian, Mantas Čepulkovskis, Sumanta Das, Peter Lodahl, Klemens Hammerer, and Anders S. Sørensen. Strongly Correlated Photon Transport in Waveguide Quantum Electrodynamics with Weakly Coupled Emitters. *Physical Review Letters*, 121(14), 2018.

[137] Sahand Mahmoodian, Giuseppe Calajó, Darrick E. Chang, Klemens Hammerer, and Anders S. Sørensen. Dynamics of Many-Body Photon Bound States in Chiral Waveguide QED. *Physical Review X*, 10(3), 2020.

[138] Natasha Tomm, Sahand Mahmoodian, Nadia O. Antoniadis, Rüdiger Schott, Sascha R. Valentin, Andreas D. Wieck, Arne Ludwig, Alisa Javadi, and Richard J. Warburton. Photon bound state dynamics from a single artificial atom. *Nature Physics*, 19(6), 2023.

SELBSTSTÄNDIGKEITSERKLÄRUNG

Ich erkläre, dass ich die Dissertation selbständig und nur unter Verwendung der von mir gemäß § 7 Abs. 3 der Promotionsordnung der Mathematisch-Naturwissenschaftlichen Fakultät, veröffentlicht im Amtlichen Mitteilungsblatt der Humboldt-Universität zu Berlin Nr. 42/2018 am 11.07.2018 angegebenen Hilfsmittel angefertigt habe.

Berlin, 18.06.2024

Daniel Lechner